Minimal nuclear energy density functional

Aurel Bulgac,[1,*] Michael McNeil Forbes,[1,2,†] Shi Jin,[1,‡] Rodrigo Navarro Perez,[3,§] and Nicolas Schunck[3,‖]
[1]*Department of Physics, University of Washington, Seattle, Washington 98195-1560, USA*
[2]*Department of Physics and Astronomy, Washington State University, Pullman, Washington 99164-2814, USA*
[3]*Nuclear and Chemical Science Division, Lawrence Livermore National Laboratory, Livermore, California 94551, USA*

(Received 27 August 2017; revised manuscript received 8 January 2018; published 17 April 2018)

We present a minimal nuclear energy density functional (NEDF) called "SeaLL1" that has the smallest number of possible phenomenological parameters to date. SeaLL1 is defined by seven significant phenomenological parameters, each related to a specific nuclear property. It describes the nuclear masses of even-even nuclei with a mean energy error of 0.97 MeV and a standard deviation of 1.46 MeV, two-neutron and two-proton separation energies with rms errors of 0.69 MeV and 0.59 MeV respectively, and the charge radii of 345 even-even nuclei with a mean error $\epsilon_r = 0.022$ fm and a standard deviation $\sigma_r = 0.025$ fm. SeaLL1 incorporates constraints on the equation of state (EoS) of pure neutron matter from quantum Monte Carlo calculations with chiral effective field theory two-body (*NN*) interactions at the next-to-next-to-next-to leading order (N3LO) level and three-body (*NNN*) interactions at the next-to-next-to leading order (N2LO) level. Two of the seven parameters are related to the saturation density and the energy per particle of the homogeneous symmetric nuclear matter, one is related to the nuclear surface tension, two are related to the symmetry energy and its density dependence, one is related to the strength of the spin-orbit interaction, and one is the coupling constant of the pairing interaction. We identify additional phenomenological parameters that have little effect on ground-state properties but can be used to fine-tune features such as the Thomas-Reiche-Kuhn sum rule, the excitation energy of the giant dipole and Gamow-Teller resonances, the static dipole electric polarizability, and the neutron skin thickness.

DOI: 10.1103/PhysRevC.97.044313

I. INTRODUCTION

The accurate and precise calculation of ground-state nuclear properties and nuclear dynamics represent a formidable challenge for quantum many-body theory. While there exist a variety of techniques for directly solving the many-body Schrödinger equation, most of them are often limited to static properties and do not scale well with the number of particles in the system. In contrast, density functional theory (DFT) provides a unified framework for computing both static and dynamic properties. Although in principle exact, at least for atomic systems [1,2], the theory does not provide the form of the energy functional. A successful implementation of DFT thus requires a physically motivated functional form, together with carefully fitted phenomenological parameters, or alternatively, a first-principle derivation. Most nuclear energy density functionals (NEDF) in the literature are typically constructed by building the functional from the expectation value of effective nuclear forces on Slater determinants, such as the Skyrme and Gogny parameters, or by considering the average values of effective Lagrangians as in the relativistic mean-field theory [3]. Despite a significant research investment [4–9], improvements to these functionals have been incremental.

In this paper, we present a different approach, revisiting the motivation behind the form of current DFTs. We systematically construct a truly minimal NEDF, which we call SeaLL1, that cleanly separates the phenomenological parameters into hierarchies. Unlike typical NEDFs, which are built directly from the approach of Kohn and Sham [10], we start with a minimal orbital-free formulation functional of neutron and proton densities in the spirit of Hohenberg and Kohn [1], along the lines delineated by Weizsäcker [11]. Built on a core of four dominant parameters, this orbital-free NEDF obtains a global mass fit better than the four-parameter Bethe-Weizsäcker mass formula [12], but in addition provides quite accurate charge radii. The orbital based SeaLL1 functional then minimally extends this four-parameter NEDF by adding three parameters to describe shell effects, pairing correlations, and the density dependence of the symmetry energy, the latter which governs the neutron skin thickness of ^{208}Pb and ^{48}Ca. In this form, the seven parameter SeaLL1 functional displays extremely reasonably single-particle spectra, globally fitting masses, charge radii, and two-nucleon separation energies. As the nucleon effective mass in SeaLL1 is the bare nucleon mass, we expect the total energy level densities to be in much better agreement with experiment than for typical Skyrme-like NEDFs.

Since we advocate a new paradigm for constructing and improving a NEDF, we begin in Sec. II with a somewhat lengthy historical background to motivate our approach in

*bulgac@uw.edu
†mforbes@alum.mit.edu
‡js1421@uw.edu
§navarrop@ohio.edu
‖schunck1@llnl.gov

Sec. III. The form of the SeaLL1 functional is presented in detail in Sec. III along with its orbital-free formulation. Section IV discusses a number of nuclear properties that have been used to validate the predictive power of our NEDF. Section V identifies how the NEDF could be systematically improved for applications either to static or dynamical properties. Finally, we summarize our results in Section VI. The hurried reader can just read Secs. III and IV, which contain all the results.

For the interested reader, we provide additional material in Appendix A, where we discuss in more detail the orbital-free formulation and illustrate the dominance or subdominance of various parameters. Numerical values for the functional parameters, as well as tables of quantities used in our fits, are provided as Supplementary Material [13].

II. HISTORICAL BACKGROUND AND MOTIVATIONS

Almost a century ago, Aston [14] realized that a nucleus is not quite the sum of its parts. This led Eddington [15] to correctly conjecture a link between nuclear masses, the conversion of hydrogen into heavier elements, and the energy radiated by the stars. An accurate theoretical model of nuclear masses, particularly close to the neutron drip line and with an uncertainty of better than 100 keV (an accuracy which has not been achieved yet even for known stable nuclei), will have a great impact on predicting the origin and the abundances of elements in the Universe [16,17].

When quantum mechanics was first applied to many-body systems, Weizsäcker [11] proposed that an energy density approach could be an effective tool for calculating nuclear binding energies. This was the first instance of an energy density functional being applied in nuclear physics, several decades before the foundation of DFT [1,2,10] was formulated. Bethe and Bacher [12] further developed Weizsäcker's ideas and introduced the nuclear mass formula (the Bethe-Weizsäcker formula) for the ground-state energies of nuclei with $A = N + Z$ nucleons (N neutrons and Z protons):

$$E(N,Z) = a_v A + a_s A^{2/3} + a_C \frac{Z^2}{A^{1/3}} + a_I \frac{(N-Z)^2}{A}. \quad (1)$$

Unlike electrons in atoms, nuclei are saturating systems with a nearly constant interior density. This yields the terms in Eq. (1) referred to as volume energy, surface tension, nonextensive Coulomb energy, and symmetry energy that favors similar numbers of protons and neutrons. (Because of the presence of the long-range Coulomb interaction, the terms "volume" and "surface" do not have a strict thermodynamic meaning.) As shown in the first row of Table I, these four terms alone fit the AME2012 evaluated nuclear masses [18,19] with a rms error of $\chi_E = 3.30$ MeV per nucleus. This is a remarkable result: the nuclear binding energy of heavy nuclei can reach 2000 MeV; hence the errors are at the subpercent level.

A slightly better fit is obtained using a mass formula with surface corrections terms to the symmetry and Coulomb energies, as well as odd-even staggering correction due to pairing:

$$E(N,Z) = a_v A + a_s A^{2/3} + a_C \frac{Z^2}{A^{1/3}} + a'_C \frac{Z^2}{A^{2/3}} + a_I \frac{(N-Z)^2}{A} + a'_I \frac{(N-Z)^2}{A^{4/3}} + \Delta. \quad (2a)$$

$$\Delta = \begin{cases} -\delta A^{-1/2} & \text{even-even nuclei,} \\ 0 & \text{odd nuclei,} \\ \delta A^{-1/2} & \text{odd-odd nuclei.} \end{cases} \quad (2b)$$

TABLE I. Parameters and the energy rms of the mass formulas Eqs. (1) or (2), with or without the even-odd staggering correction, Eq. (2b). Here $\chi_E^2 = \sum |E_{N,Z} - E(N,Z)|^2 / N_E$ and we fit the $N_E = 2375$ measured (not extrapolated) nuclear masses of nuclei with $A \geqslant 16$ from Audi *et al.* [18], Wang *et al.* [19] and an evaluated uncertainty less than 1 MeV with the electronic correction. (All quantities expressed in MeV.) The last two rows show how the mass formulas, Eqs. (1) or (2), fit the theoretical nuclear masses computed using the SeaLL1 functional.

a_v	a_s	a_I	a'_I	a_C	a'_C	δ	χ_E
−15.47	16.73	22.87	0	0.699	0	0	3.30
−15.49	16.78	22.91	0	0.700	0	12.29	3.18
−15.32	17.76	24.96	−22.60	0.767	−0.675	0	2.64
−15.34	17.80	25.01	−22.43	0.767	−0.661	11.46	2.50
−15.77	17.50	23.65	0	0.723	0	0	1.87
−15.46	18.29	25.72	−26.00	0.792	−0.773	0	1.53

This pairing contribution is significantly smaller than the others, with an amplitude $\approx 12\,\text{MeV}/A^{1/2}$. It is also smaller than contributions arising from shell-correction energies (discussed below), changing the rms error χ_E by about at most 150 keV. This fit is shown in Table I and the residuals are displayed in Fig. 1. The magnitudes of the various terms are compared in Fig. 2, which shows that the volume, surface, and Coulomb contributions are dominant, while the symmetry energy contribution is roughly at the level of 10%.

There are several possible ways to determine the volume, surface, symmetry, etc. coefficients of Eqs. (1) or (2). For example, one may turn off the Coulomb interaction and extract volume, surface, and symmetry energy from the asymptotic behavior of the energy of nuclei with very large numbers of protons and neutrons [20]. This corresponds to considering the thermodynamic limit, which is not realized in real nuclei due to the presence of the long-range Coulomb interaction among the protons. We prefer instead a unified approach, determining the parameters by directly fitting almost all nuclear binding energies, whether experimental or computed. (See last two rows of Table I.)

In a parallel development, properties of many-fermion systems were understood in mathematical physics by tying together the roles of the geometry and of the periodic trajectories in cavities. As early as 1911, Weyl [21–27] and others related the wave eigenstate density in boxes of various shapes and boundary conditions to the geometrical shape of the box [28–31]. In a manner similar to the nuclear mass formula

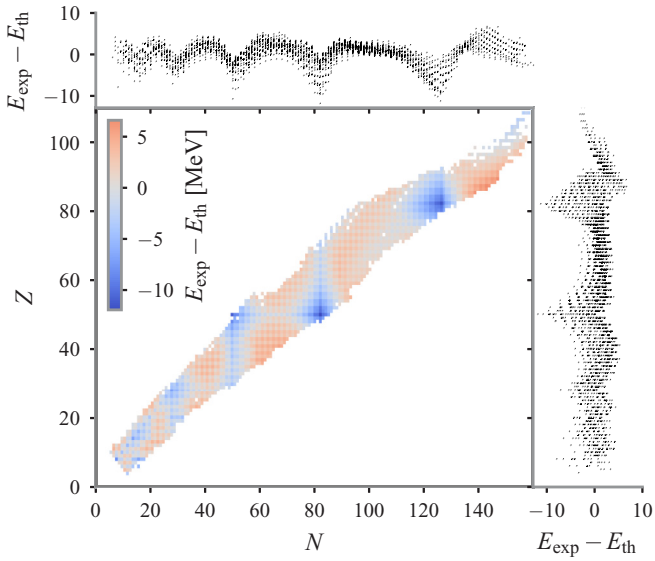

FIG. 1. The differences $E_{\rm exp} - E_{\rm th}$ in MeVs between the evaluated ground state energies $E_{\rm exp}(N,Z)$ [18,19] of 2375 nuclei with $A \geqslant 16$ and fitted with the six-parameter mass formula $E_{\rm th} = E(N,Z)$ [Eq. (2)] with $\Delta \equiv 0$. One can easily identify the location of closed shells (the blue regions) for protons and neutrons.

Eq. (1), this approach can be applied to saturating systems, relating the ground-state energy to the volume (V), surface area (A), and mean curvature radius R of the many-particle system [20]:

$$E = a_V V + a_S S + a_R R + \cdots . \tag{3}$$

The similarity between Eq. (3) and the nuclear mass formula Eq. (1) becomes apparent after relating the volume to the particle number $n = A/V \approx$ const. The ground-state energy can thus be rewritten in terms of particle number A (here for only one kind of particles):

$$E = b_V A + b_S A^{2/3} + b_R A^{1/3} + \cdots . \tag{4}$$

The coefficient b_V is the energy per particle in infinite matter and a_S represents the surface tension. These types of expansion

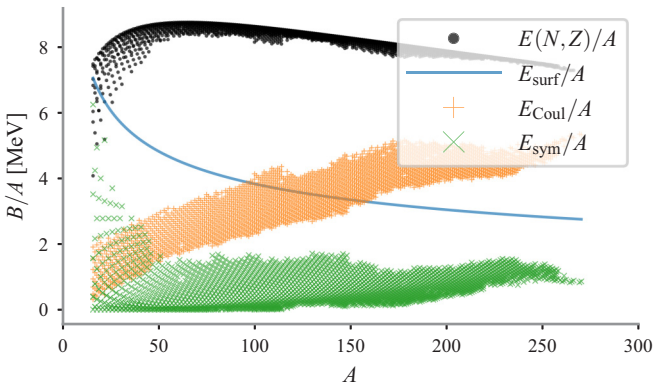

FIG. 2. The binding energy per nucleon $B/A = |E(N,Z)|/A$ and the Coulomb, surface and symmetry energy per nucleon in Eq. (2) for the measured 2375 nuclei with $A \geqslant 16$ [18,19].

are classical in character: Planck's constant plays no explicit role. Their accuracy for many-fermion systems is thus limited by the lack of quantum effects (often referred to as shell effects). It appears that for nuclei, the mass formula Eq. (2) is about as good as one can achieve without introducing the quantum effects.

There is a long debate in literature, fueled mainly by studies of quantum chaos, about whether an expansion in powers of A can be extended beyond the terms present in Eq. (4). Naïvely, one might expect the next terms to be proportional to A^0, $A^{-1/3}$, and so forth, but a a more careful analysis shows that that is not correct. (See, for example, Brack and Bhaduri [31].) The next term is instead proportional to $A^{1/6}$ [32–35], arising from the contribution of periodic orbits. Subsequent terms appear to be stochastic, due to the inherent chaotic character of the interacting many-body systems [36]. It is well established by now that ideas originating from quantum chaos and random matrices provide extremely useful tools to study properties of neutron resonances, for example, in the region of nuclear spectra where the level density is quite high. Subsequent works have shown [37] that even the properties of ground states in many-fermion systems are amenable to study using similar ideas. Thus it should not be surprising that small contributions to the nuclear binding energies might be interpreted using similar ideas.

Gutzwiller [38], Balian and Bloch [32–34], and Berry and Tabor [39,40] observed that quantum states in a finite system can be quite accurately reproduced by quantizing the periodic classical trajectories. (See also Brack and Bhaduri [31].) Combining the idea of geometric quantization with the Thomas-Fermi model, the Pauli principle, and copious empirical evidence that strongly interacting fermionic systems share many similarities with noninteracting systems [41–47], one can quite accurately construct the single-particle density of states and binding energies as a function of the particle number, eventually correcting this by the shape of the system.

The single-particle density of states $n(\varepsilon)$ in a given potential has a smooth and an oscillating components:

$$n(\varepsilon) = n_{\rm TF}(\varepsilon) + n_{\rm osc}(\varepsilon), \tag{5a}$$

$$n_{\rm osc}(\varepsilon) = \sum_{\rm PO} a_{\rm PO}(\varepsilon) \sin\left(\frac{S_{\rm PO}(\varepsilon)}{\hbar} + \phi_{\rm PO}\frac{\pi}{2}\right) + \cdots , \tag{5b}$$

where the sum is performed over classical periodic orbits (PO) (diameter, triangles, squares, etc.). Here, $a_{\rm PO}(\varepsilon)$ is the stability amplitude, $S_{\rm PO}(\varepsilon)$ is the action, and $\phi_{\rm PO}$ is the Maslov index of each orbit at the energy ε [31–34,48]. The single-particle density of states in the Thomas-Fermi approximation $n_{\rm TF}$ [21–31] has a clear dependence on the size and shape of the system, and leads to Eqs. (3) and (4) for a square-well potential. At the same time, the nature of the periodic orbits also depends on the size and shape of the single-particle potential. Knowing $n(\varepsilon)$, one can calculate the particle number A and shell corrections (SC) $E_{\rm SC} = E - E_{\rm TF}$ for a many-fermion system by integrating up to the chemical potential μ:

$$A = \int_{-\infty}^{\mu} n(\varepsilon)d\varepsilon, \; E_{\rm SC} = \int_{-\infty}^{\mu} \varepsilon n_{\rm osc}(\varepsilon)d\varepsilon. \tag{6}$$

The theory of periodic orbits and structure of these shell corrections has been studied extensively. For example, in a three-dimensional spherical cavity, quantum effects can be reproduced by including only triangular and square orbits [31–34,48]. The emergence of magic numbers, and the role of the shapes of many-fermion systems have been tested in theory and validated against experimental results in fermion systems with up to 3000 electrons [49–51]. In particular, in atomic clusters, the emergence of supershells has been predicted theoretically [48,50,52] and confirmed experimentally [49,51]. (Nuclei are too small to exhibit supershells.)

In nuclear physics, a similar line of inquiry is encapsulated in the method of shell corrections, developed by Strutinsky [53–55] and many others [35,56–68]. This method shows that $n(\varepsilon)$ has a well-defined dependence on the particle number. The smooth part of the density of states is quite well described by the Thomas-Fermi approximation (and by the smoothing procedure introduced by Strutinsky). The leading terms are the volume ($\sim A$), surface ($\sim A^{2/3}$), Coulomb ($\sim Z^2/A^{1/3}$), and symmetry energy [$\sim (N-Z)^2/A$] contributions encoded in the Bethe-Weizsäcker mass formula (1). The oscillating part is dominated by the nuclear shape and the shell effects from the periodic orbits, where the amplitude depends on the particle number as $A^{1/6}$ [35].

The separation of $n(\varepsilon)$ into the smooth and oscillating parts (5a) is a general characteristic of the many-fermion systems. Both the macroscopic-microscopic method [35,53–68] and self-consistent approaches [3,69–75] lead to the same conclusions about the various contributions described above and agree with experimental data [76]. In all previous considerations of mass tables, either in self-consistent approaches or in microscopic-macroscopic models, the single-particle spectroscopic factors are modified only by pairing correlations. It is well known, however, that the coupling between collective degrees of freedom and single-particle degrees of freedom lead to a significant fragmentation of the single-particle occupation probabilities, which are measured in pickup and knockout reactions [64,77]. This fragmentation of the single-particle occupation probabilities is not taken into account in the single-particle density of states Eqs. (5) or in the definition of the single-particle densities Eqs. (10), and is likely to affect the exact magnitude of the shell effects. The order of magnitude of these effects is perhaps a (small) fraction of the rms error $\chi_E = 3.3$ MeV of the Bethe-Weizsäcker mass formula (1). All of this begs the question: To what order can one expand the density of states in powers of the particle numbers and periodic orbits?

There is a reasonable consensus that, beyond the leading contributions from the periodic orbits and shell corrections, any such expansion fails due to the effects of quantum chaos—i.e., contributions from classically chaotic trajectories through the many-body phase space [36]. Stable periodic orbits provide the strongest shell effects in quantum systems, evidenced by the appearance of magic numbers (see, e.g., Fig. 1). Unstable periodic orbits also produce shell effects but with smaller weights. In contrast, chaotic orbits appear to produce irregular oscillations in the single-particle density of states with a rather small amplitude. Various estimates suggest that chaotic fluctuations appear at the level of 0.5 MeV per nucleus [78–86], noticeably smaller than shell effects contributions due to periodic orbits and deformations, which are of the order of several MeVs.

The effect of periodic orbits is not limited to finite systems: The Casimir energy in quantum field theory [87,88], critical phenomena [89,90], and strongly interacting infinite inhomogeneous systems, e.g., nuclear pasta phase in neutron stars [91–97], can also be explained and calculated to high precision by evaluating the contributions from periodic orbits. This method has become the standard approach for evaluating the Casimir energy in a variety of fields [98–102].

It is somewhat surprising that shell effects from periodic orbits appear at the same level as deformation effects in the energy of nuclear systems. Naïvely one might expect the deformation energy to be controlled by the surface area of a saturating system and thus to contribute as a correction to the surface term in nuclear mass formulas like Eqs. (1) and (2). However, the deformation energy in nuclei has a quantum nature and is determined by a delicate interplay between the change in surface area and the shell effects. A similar behavior has been observed in the case of atomic clusters with up to 3000 electrons [52]. This leads to a leveling of the peaks, which one would otherwise expect in the absence of deformation, leaving in place only the large negative shell corrections for the magic spherical systems, as seen in Fig. 1 for the case of nuclei.

The shape stability of a many-fermion system is controlled by the single-particle level density at the Fermi level. In an open-shell system, this level density is high; the system can thus deform quite easily and single-particle levels can rearrange until the level density is low enough to render the system stable. The stabilization process of the nuclear deformation in the ground state is analogous to the Jahn-Teller effect in polyatomic molecules [103], where the high degeneracy of the ground state is lifted by the deformation of the system. This mechanism leads to new "magic numbers" in deformed systems as Strutinsky discussed in his seminal papers [53–55]. The increase in surface area and the energy penalty incurred (deformation energy) is canceled to a large extent by the shell corrections (due to periodic orbits in the deformed potential), unless the system is "magic" or "semimagic." The cancellation between deformation energy and shell effects suggests that open-shell systems should be easier to deform than magic systems. This is consistent with the character of the residuals remaining after fitting the nuclear binding energies with Bethe-Weizsäcker formulas like Eqs. (1) and (2) (as shown in Fig. 1). The largest residuals appear as large (negative) spikes at the shell closures for spherical nuclei with magic numbers of either protons and/or neutrons, while the expected (positive) peaks in between magic numbers are flattened. From the nature of the residuals $E_{\rm exp} - E_{\rm th}$ in Fig. 1— sharp negative spikes at the magic numbers, but roughly constant fluctuations in between—one can conclude that mass formulas of the type in Eq. (2) do encode the role of the nuclear deformation. For open shell nuclei, it thus appears that the deformation energy is roughly compensated by the shell-correction energy and shell effects only survive near magic and semimagic nuclei.

A number of corrective terms might be considered to improve the accuracy of the nuclear mass formulas, Eqs. (1)

and (2). For example, in the Coulomb term, one might replace Z^2 with $Z(Z-1)$ to correctly count the number of proton pairs, and one might add an additional term proportional to Z to account for the Coulomb exchange interaction and screening [104]. Motivated by Eq. (4), one might also consider including terms proportional to $A^{1/3}$ and A^0. The symmetry energy terms might also be "corrected" by replacing $(N-Z)^2/4$ with $T(T+1)$ where $T=|N-Z|/2$. Finally, one might introduce an additional correction to account for the Wigner energy $\propto |N-Z|$, which appears as a cusp in the nuclear binding energies as a function of $N-Z$ (basically only for nuclei with small values of $|N-Z|$) [105]. However, including these corrections lead to very small improvements in the energy rms χ_E below the value 2.64 MeV obtained with the main terms of Eq. (2). All these corrections are eclipsed by the shell effects as seen in Fig. 1.

There are a variety of many-body approaches based on the Schrödinger equation: The quantum Monte Carlo (QMC) method [106,107], the self-consistent Green's function method [108], the coupled-cluster method [109], and the in-medium renormalization method [110]. In all these approaches, one has to specify the two-body (*NN*), three-body (*NNN*), etc., interactions between nucleons, the form of which is ambiguous and depends on how the theory is regularized. Chiral effective field theory (EFT) [111,112] provides a framework for organizing these interactions using the symmetries of the underlying theory quantum chromodynamics (QCD) of quarks and gluons with the hope that physical results are independent of the energy cutoff. In general, there is still no guarantee, however, that this many-body expansion converges quickly enough using a naïve sum of diagrams [113,114].

The DFT approach differs from approaches based on the Schrödinger equation. For many-electron systems, it has been established that there is a mathematical one-to-one correspondence between the number density and the wave function of a many-body system [1,2], and this one-to-one correspondence leads to the existence of an exact energy density functional. In practice, however, this functional is extremely complicated and establishing a useful form is more of an art than a science. One particularly successful example is the unitary Fermi gas (UFG), which shares many properties with dilute neutron matter, and is also a superfluid with a large pairing gap [115]. In this case, the form of a local energy density functional follows using only dimensional arguments, renormalizability of the theory, Galilean invariance, and symmetries. The functional and the corresponding framework needed to treat fermionic superfluids is called the superfluid local density approximation (SLDA) (extending the local density approximation (LDA) acronym of Kohn and Sham [10]), and has been verified and validated against both QMC calculations and experiments at the few percent level for a wide range of systems [116,117]. Our approach here is motivated by similar considerations, leading to a simple and compact functional in which time-dependent phenomena can be treated easily as well. Thus, unlike approaches based on the Schrödinger equation, which are primarily limited to static properties, the DFT can be applied to reactions, fission, time-dependent nonequilibrium phenomena, and very heavy systems with remarkable accuracy.

III. FORM OF THE FUNCTIONAL

The lesson from our brief historical review is that, since nuclei are saturating systems with a rather well-defined saturation density, the bulk of the nuclear binding energy should be fixed by the geometry of the nuclei (volume, surface area, curvature radius) to subpercent accuracy. As demonstrated in Table I, the accuracy of the mass formulas Eqs. (1) and (2)—which both lack shell effects, deformation, spin-orbit effects, pairing, etc.—suggests that such a nuclear energy density functional (NEDF) should be capable of describing at a similar level of accuracy both the nuclear binding energies and the proton and neutron matter density distribution. Therefore, we might reasonably expect that a NEDF will also describe the nuclear charge radii, for which there is a large amount of accumulated data [118]. Shell effects, pairing correlations, and beyond-mean-field corrections, enter at the level of a few MeVs per nucleus, reducing the rms energy error χ_E from around 3 to about 0.5 MeV [66–68] and are most pronounced for magic or semimagic nuclei; see Fig. 1.

We will describe a NEDF that depends on the smallest number of phenomenological parameters needed to account for all the contributions in the nuclear mass formulas, Eqs. (1) and (2). First, we relate these parameters to various physical quantities relevant for nuclear physics. For a large nucleus, the Coulomb energy can be used to estimate the saturation density n_0 by approximating the nucleus as a uniformly charged sphere with $E_C = 3Z^2e^2/5R = a_C Z^2/A^{1/3}$, where $R = r_0 A^{1/3}$ and $r_0 \approx 1.2$ fm is a nuclear length scale:

$$n_0 = \frac{3}{4\pi r_0^3}, \quad \text{where} \quad r_0 = \frac{3e^2}{5a_C}. \tag{7a}$$

One can further estimate the ground-state energy of infinite nuclear matter per nucleon ε_0, the nuclear surface tension σ, and their dependence on the isospin $(N-Z)/2$:

$$\varepsilon_0 = \frac{E(N,Z)}{A} = a_v + a_I \frac{(N-Z)^2}{A^2}, \tag{7b}$$

$$\sigma = a_s + a_I' \frac{(N-Z)^2}{A^2}. \tag{7c}$$

Finally, one can relate the value of the coefficient a_C' (or of the alternative coefficient of the contribution $a_C'' Z^2/A$ to the mass formula [59]) with the nuclear surface diffuseness. For a NEDF to be as accurate as the mass formula, one expects no more than five or six significant parameters. As we shall see, such a functional does exist, requiring as few as four parameters, and demonstrating better accuracy than the original Bethe-Weizsäcker mass formula, with the additional property of predicting charge radii. That a functional depending on such a small number of phenomenological parameters can go beyond the capabilities of the empirical mass formula and also describe density distributions is truly remarkable.

We postulate a NEDF with three main contributions, which significantly improves on the Weizsäcker's original idea [11]:

$$\mathcal{E}[n_n, n_p] = \overbrace{\mathcal{E}_{\text{kin}}}^{\text{kinetic}} + \underbrace{\mathcal{E}_C}_{\text{Coulomb}} + \overbrace{\mathcal{E}_{\text{int}}}^{\text{interactions}}. \tag{8}$$

The first two terms—the kinetic energy and Coulomb energy—are well motivated and have no free parameters. All phenomenological parameters of the model appear in the interaction term $\mathcal{E}_{\rm int}$:

$$\mathcal{E}_{\rm int} = \overbrace{\mathcal{E}_{\rm homo}}^{\text{homogeneous}} + \underbrace{\mathcal{E}_{\nabla n}}_{\text{gradients}} + \overbrace{\mathcal{E}_{\rm SO}}^{\text{spin-orbit}} + \underbrace{\mathcal{E}_{\Delta}}_{\text{pairing}} + \overbrace{\mathcal{E}_{\rm entrain}}^{\text{entrainment}}, \quad (9)$$

The Kohn-Sham formulation of the functional is specified in terms of the single-particle orbitals $v_{k\sigma}(\boldsymbol{r}), v_{k\sigma}(\boldsymbol{r})$ through the time-even number, anomalous, kinetic, and spin-current densites (for both neutrons and protons),

$$n(\boldsymbol{r}) = \sum_{k,\sigma} v^*_{k\sigma}(\boldsymbol{r}) v_{k\sigma}(\boldsymbol{r}), \quad (10a)$$

$$\nu(\boldsymbol{r}) = \sum_{k} v^*_{k\uparrow}(\boldsymbol{r}) u_{k\downarrow}(\boldsymbol{r}), \quad (10b)$$

$$\tau(\boldsymbol{r}) = \sum_{k,\sigma} \boldsymbol{\nabla} v^*_{k\sigma}(\boldsymbol{r}) \cdot \boldsymbol{\nabla} v_{k\sigma}(\boldsymbol{r}), \quad (10c)$$

$$\boldsymbol{J}(\boldsymbol{r}) = \frac{\boldsymbol{\nabla} - \boldsymbol{\nabla}'}{2\mathrm{i}} \times \sum_{k,\sigma,\sigma'} v^*_{k\sigma}(\boldsymbol{r}) \boldsymbol{\sigma}_{\sigma,\sigma'} v_{k\sigma'}(\boldsymbol{r}') \Big|_{\boldsymbol{r}=\boldsymbol{r}'}. \quad (10d)$$

as well as the time-odd spin-density and current (which are nonvanishing if time-reversal symmetry is broken)

$$\boldsymbol{s}(\boldsymbol{r}) = \sum_{k,\sigma,\sigma'} v^*_{k\sigma}(\boldsymbol{r}) \boldsymbol{\sigma}_{\sigma,\sigma'} v_{k\sigma'}(\boldsymbol{r}), \quad (10e)$$

$$\boldsymbol{j}(\boldsymbol{r}) = \sum_{k,\sigma} \frac{\boldsymbol{\nabla} - \boldsymbol{\nabla}'}{2\mathrm{i}} v^*_{k\sigma}(\boldsymbol{r}') v_{k\sigma}(\boldsymbol{r}) \Big|_{\boldsymbol{r}=\boldsymbol{r}'}; \quad (10f)$$

see Refs. [3,119] and references therein for details. [Note: In nuclear physics literature, proton and neutron number densities are typically denoted with the symbols $\rho_{n,p}(\boldsymbol{r})$. In accordance with the wider physics literature, we reserve ρ for mass densities, which are related to number densities by $\rho_{n,p}(\boldsymbol{r}) = m n_{n,p}(\boldsymbol{r})$].

Developing an orbital-free version of (9) would require expressing all the various terms exclusively in terms of the number density $n(\boldsymbol{r})$. Whether such a NEDF exists and how it should be implemented remains an open question. In this work, we will implement an orbital-free functional by approximating all the auxiliary densities (10) as functions of the number density; see Sec. III H for details.

A. Kinetic terms

The kinetic energy density derives from the energy density of a noninteracting system of protons and neutrons and contains no free parameters:

$$\mathcal{E}_{\rm kin} = \frac{\hbar^2}{2m}(\tau_n + \tau_p) - \frac{\delta m}{2m}\frac{\hbar^2}{2m}(\tau_n - \tau_p) + O\left(\frac{\delta m}{2m}\right)^2, \quad (11)$$

where $\tau_{n,p}$ are the kinetic densities in the Hartree-Fock-Bogoliubov (HFB) formulation with neutron and proton $m_{n,p} = m \pm \delta m/2$. In principle, one should include an explicit isospin splitting due to the different proton and neutron masses, but we follow here common practice in nuclear theory to use a common average mass $m = (m_n + m_p)/2$ and neglect $\delta m = m_n - m_p$. Note that since we are using the bare masses here, the theory is covariant under Galilean boosts. The consideration of terms with a more complex dependence on the kinetic energy densities requires adding current terms to restore the Galilean covariance of the theory (see, e.g., Refs. [3,120–123].)

B. Coulomb terms

The direct Coulomb energy and exchange contribution in the Slater approximation are

$$\mathcal{E}_C(\boldsymbol{r}) = \frac{1}{2} V_C(\boldsymbol{r}) n_{\rm ch}(\boldsymbol{r}) - \frac{e^2\pi}{4}\left[\frac{3n_p(\boldsymbol{r})}{\pi}\right]^{4/3}, \quad (12a)$$

$$V_C(\boldsymbol{r}) = e^2 \int d^3\boldsymbol{r}', \quad \frac{n_{\rm ch}(\boldsymbol{r}')}{|\boldsymbol{r} - \boldsymbol{r}'|} \quad (12b)$$

where e is the proton charge and $n_{\rm ch}$ is the charge density, which is obtained from the proton and neutron densities by convolution (here noted with an asterisk, $*$) with the appropriate charge form factors (see Appendix E for details):

$$n_{\rm ch} = G^n_E * n_n + G^p_E * n_p. \quad (12c)$$

Including the form factors does not significantly improve the mass fits but improves somewhat the fit of the charge radii. In principle, one might allow the coefficient of the Coulomb exchange term to vary; this is done, for example, in atomic physics in order to obtain better estimates of the Coulomb exchange energy. We find, however, that fitting the nuclear binding energies leads with high accuracy to the same coefficient presented in Eq. (12a), so we leave it fixed and do not include this as a parameter in our model.

We require our energy density functional to be an isoscalar and include no isospin breaking terms other than those due to the neutron-proton mass difference (which we neglect here) and the Coulomb interaction. Additional isospin violation due to up and down quark mass differences and electromagnetic effects [124–128] beyond these two contributions are much smaller and are partly responsible for the Nolen-Schiffer anomaly [129], to which the screening of the Coulomb exchange also contributes at a comparable level [104,130].

C. Homogeneous terms: Infinite nuclear and neutron matter

We parametrize the nuclear EoS as

$$\mathcal{E}_{\rm homo} = \sum_{j=0}^{2} \mathcal{E}_j(n)\beta^{2j}, \quad (13a)$$

$$\mathcal{E}_j(n) = \varepsilon_j(n) n = a_j n^{5/3} + b_j n^2 + c_j n^{7/3}, \quad (13b)$$

where n is the total density and β is the asymmetry:

$$n = n_n + n_p, \qquad \beta = \frac{n_n - n_p}{n_n + n_p}. \quad (13c)$$

We have considered terms with powers of the density $n^{8/3} \sim n\tau$ and higher, but in all our fits of the nuclear masses, we found such terms to be unconstrained in magnitude, barely improving the quality of the fits.

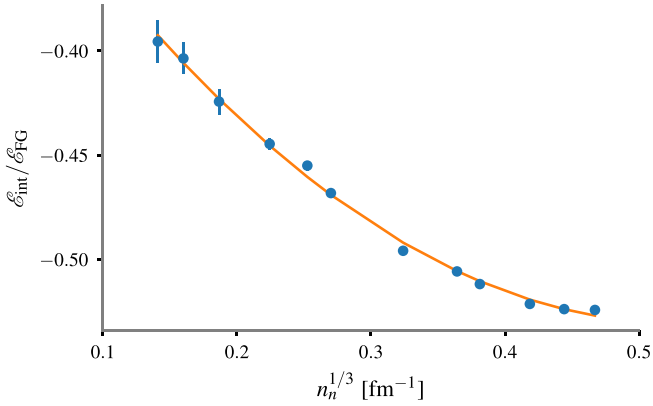

FIG. 3. The QMC results of Wlazłowski *et al.* [131] for the interaction energy per neutron displayed as the ratio $\mathcal{E}_{\rm int}/\mathcal{E}_{\rm FG}$ defined in Eq. (15b) (with $\beta = 1$), where $\mathcal{E}_{\rm FG} = 3\hbar^2(3\pi^2 n_n)^{2/3} n_n/(10 m_n)$. If $a_n = 0$ in Eq. (15b), the ratio $\mathcal{E}_{\rm int}/\mathcal{E}_{\rm FG}$ would tend to 0 for $n_n \to 0$. For densities $n_n^{1/3}|a_{nn}| < 1$ (where $a_{nn} = -18.9$ fm is the s-wave neutron-neutron scattering length), the leading-order correction to the kinetic energy density per particle contribution would be instead linear in density $4\pi\hbar^2 a_{nn} n_n/m_n$.

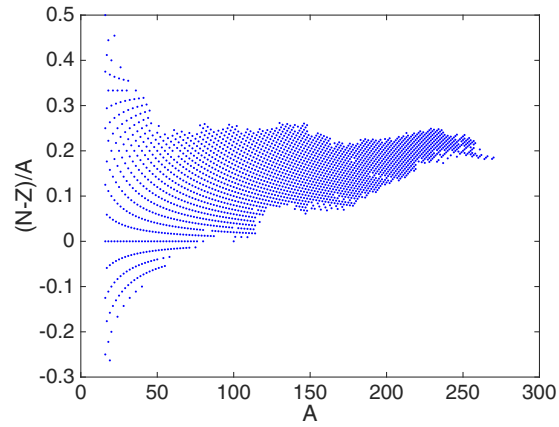

FIG. 4. The contribution to the ground-state energies of the terms quartic in isospin density $\delta E_{I4} = \int d^3\boldsymbol{r}\, \mathcal{E}_2(n)\beta^4$, evaluated perturbatively with NEDF-1 (see Table IV). In the lower panel, we display the ratio $(N-Z)/A$ for the nuclei we have considered. Among the 2375 nuclei we have considered, there are 33 nuclei with $N = Z$, 78 nuclei with $Z > N$, and 70 nuclei with $|N-Z|/A > 1/4$.

In infinite homogeneous nuclear matter, as might be found in a neutron star, for example, the gradient, spin-orbit, entrainment, and Coulomb terms vanish (charge neutrality is maintained by a background of electrons). The semiclassical expansion of the kinetic energy density $\mathcal{E}_{\rm kin}$ becomes exact in the leading Thomas Fermi term $\tau = \tau_{\rm TF}$. Thus, neglecting the small neutron-proton mass difference $m_n \approx m_p \approx m$, the functional acquires the simple form:

$$\mathcal{E}(n_n, n_p) = \frac{3\hbar^2(3\pi^2)^{2/3}}{10m}\left(n_n^{5/3} + n_p^{5/3}\right) + \sum_{j=0}^{2}(a_j n^{5/3} + b_j n^2 + c_j n^{7/3})\beta^{2j}. \quad (14)$$

This portion of the functional is essentially an expansion in powers of the Fermi momenta k_F: $k_{n,p} = (3\pi^2 n_{n,p})^{1/3}$ with only three terms k_F^5, k_F^6, and k_F^7. This type of expansion is ubiquitous in many-body perturbation theory, and also applies to fitting the neutron matter EoS with high accuracy ($n_p = 0$, $\beta = 1$):

$$\mathcal{E}_n(n_n) = \frac{3\hbar^2}{10m_n}(3\pi^2 n_n)^{2/3} n_n + \mathcal{E}_{\rm int}(n_n), \quad (15a)$$

$$\mathcal{E}_{\rm int}(n_n) = a_n n_n^{5/3} + b_n n_n^2 + c_n n_n^{7/3}, \quad (15b)$$

The coefficients a_n, b_n, and c_n are fixed by fitting the neutron matter EoS as calculated with QMC including up to next-to-next-to-next-to leading order ($\mathrm{N^3LO}$) two-body and up to next-to-next-to ($\mathrm{N^2LO}$) three-body interactions from chiral perturbation theory [131]:

$$\begin{aligned} a_n &= a_0 + a_1 + a_2 = -32.6\,\mathrm{MeV\,fm^2}, \\ b_n &= b_0 + b_1 + b_2 = -115.4\,\mathrm{MeV\,fm^3}, \\ c_n &= c_0 + c_1 + c_2 = 109.1\mathrm{MeV\,fm^4}. \end{aligned} \quad (16)$$

As seen from Fig. 3, all three terms (but no more) are needed in Eq. (15b) for an accurate reproduction of the neutron EoS (see also Appendix D). When we include the $j = 2$ quartic terms in Eq. (14), the values of a_2, b_2, and c_2 are determined from the values of a_n, b_n, and c_n describing the QMC results (16), without adding additional free parameters to the NEDF.[1]

The contribution of quartic terms to nuclear masses is small (typically less than 1 MeV) since in most nuclei $\beta < 0.25$; see Fig. 4 and Sec. III G. However, the best-fit functional with only quadratic β^2 ($j = 1$) terms does not reproduce the neutron matter EoS, especially near $n \approx 0.1$ fm^{-3} (see Fig. 22). Quartic terms are thus needed to reproduce the neutron matter EoS but are not constrained by nuclear binding energies. Therefore, they provide a direct (and independent) way to incorporate the EoS of neutron matter into the NEDF.

At this time, we do not have an equally accurate QMC calculation of nuclear matter with varying isospin composition, so we must rely instead on a phenomenological approach. Our main assumption is that we can describe both the isoscalar ($j = 0$, β^0) and isovector ($j = 1$, β^2) parts of the nuclear EoS using the same three powers of Fermi momenta Eqs. (15b) and (16) as required to fit the EoS of pure neutron matter. This approach differs from typical Skyrme-like parametrizations, which include terms with higher powers of densities, e.g., $n^{8/3}$ arising from τn type of terms, where τ is kinetic energy density.

One could in principle consider additional terms of the type $\tau n^{1/3} \propto n^2$, $\tau n^{2/3} \propto n^{7/3}$, and $\tau n \propto n^{8/3}$, but the contribution

[1]We have also performed a fully self-consistent mass fit with additional powers of densities $\sum_{j=0,1}(a_j n^{5/3} + b_j n^2 + c_j n^{7/3} + d_j n^{8/3})\beta^{2j}$. While this kind of fit leads to a lower energy rms $\chi_E \approx 1.2$ MeV, the charge radii rms increases to $\chi_r \approx 0.1$ fm and the value of the incompressibility $K_0 \approx 170$ MeV is very low. Typically in these cases the parameter a_0 becomes significant and acquires relatively large negative values, similar to the behavior seen in Fig. 7. See also the discussion in Sec. III G.

to the bulk energy of such terms would be practically indistinguishable from terms n^2, $n^{7/3}$, and $n^{8/3}$. Their contribution might become important only in the surface region, and since

$$\tau n^{1/3} - \frac{3}{5}(3\pi^2)^{2/3} n^2 \propto \frac{|\nabla n|^2}{n^{2/3}}, \tag{17a}$$

$$\tau n^{2/3} - \frac{3}{5}(3\pi^2)^{2/3} n^{7/3} \propto \frac{|\nabla n|^2}{n^{1/3}}, \tag{17b}$$

$$\tau n - \frac{3}{5}(3\pi^2)^{2/3} n^{8/3} \propto |\nabla n|^2, \tag{17c}$$

most of these terms could be incorporated effectively in gradient corrections (see Secs. III D and III H).

The terms $a_j n^{5/3}$ are somewhat unexpected and are not included in Skyrme-like parametrizations. Tondeur [132] introduced only a term a_1 (without theoretical justification), but it makes sense to include the other a_j for several reasons. First, the QMC calculations of Gezerlis and Carlson [133], Wlazłowski *et al.* [131], Gandolfi *et al.* [134] (see Fig. 3) are consistent with the existence of a nonvanishing parameter a_n in the neutron EoS, which implies that $a_n = \sum_{j=0}^{2} a_j \neq 0$. Then, these terms also appear naturally in the case of the unitary Fermi gas (UFG) [135], which has been confirmed to high precision in many experiments. The UFG is a system of two species of fermions, interacting with an s-wave interaction with zero range and infinite scattering length. In response to the many-body X-games challenge posed by Bertsch in 1999, Baker [136] showed that the system was stable. The energy density of the UFG scales exactly like the kinetic energy density of a free Fermi gas $\mathcal{E} \propto n^{5/3}$. Since both neutron and protons have similar s-wave interaction properties, one expects the nuclear energy density to behave somewhat like the unitary Fermi gas at low densities.[2]

Although the energy density of the UFG scales as the kinetic energy, this is not necessarily due to a mass renormalization as one might naïvely suspect. QMC calculations of the single quasiparticle dispersion [138] and spectral weight function [139,140] both arrive at the conclusion that the effective mass in the UFG is close to the bare mass $\approx m$. However, this does not preclude the interpretation that some part of the energy arises from the kinetic energy density τ (if $m_{\text{eff}} \neq m$), as is the case in the UFG [116,123,141]. The QMC calculations are simply not yet of sufficient accuracy to confirm or exclude an effective mass different from unity.

D. Gradient terms

We include a gradient term of the following form, similar to terms considered in Skyrme NEDF [142]:

$$\mathcal{E}_{\nabla} n = \eta_s \sum_{q=n,p} \frac{\hbar^2}{2m} |\nabla n_q|^2. \tag{18}$$

One might consider a more general term of the form

$$\mathcal{E}_{\nabla} n = \eta_0 \frac{\hbar^2}{2m} |\nabla n_n + \nabla n_p|^2 + \eta_1 \frac{\hbar^2}{2m} |\nabla n_n - \nabla n_p|^2. \tag{19}$$

Note that this form of gradient term alone in an orbital-free theory leads to unphysical density profiles with a discontinuity in ∇n at a finite radius, beyond which the density vanishes exactly. However, in the presence of $\mathcal{E}_{\text{kin}}$ in an orbital-based approach, the density is well behaved. We have found that the nuclear mass fits are basically insensitive to the linear combination $\eta_m = \eta_0 - \eta_1$, and we use $\eta_s = (\eta_0 + \eta_1)/2$ and $\eta_m = (\eta_0 - \eta_1)/2 = 0$. The linear combination $\eta_m = (\eta_0 - \eta_1)/2$ can instead be used to independently fit the static isovector dipole polarizability of nuclei, as it favors a small separation between the neutron and proton surfaces if $\eta_1 > 0$.

E. Spin-orbit coupling

Related to the gradient term is the spin-orbit coupling, which we include in the same form as in the Skyrme NEDF [142]:

$$\mathcal{E}_{\text{SO}} = W_0 \boldsymbol{J} \cdot \nabla n, \tag{20}$$

where $\boldsymbol{J} = \boldsymbol{J}_n + \boldsymbol{J}_p$ is the total spin current. Following Fayans [143], we only include the isoscalar portion here as the isovector contribution is small; see Sec. V A for possible extensions.

F. Pairing interaction

The pairing energy depends on the anomalous density

$$\mathcal{E}_{\Delta} = \sum_{q=n,p} \int d^3\boldsymbol{r}\; g_{\text{eff}}(\boldsymbol{r}) |\nu_q(\boldsymbol{r})|^2 \tag{21}$$

and the effective pairing coupling strength $g_{\text{eff}}(\boldsymbol{r})$ is obtained via a renormalization [144–146] of the bare pairing strength, which may depend on neutron and proton densities.

In the case of pairing, one can consider volume, surface, or mixed pairing coupling constants, but previous studies of large sets of nuclei have shown [145,147] that there is little evidence preferring one form to another. Phenomenological studies [147] also show that the proton pairing coupling is stronger than the neutron pairing coupling, a result at odds with the naïve expectation that the proton pairing coupling should be weaker due to the Coulomb interaction [148–150]. It would also be peculiar to find that isospin invariance is broken by the pairing interaction in this manner, when no other more important terms of the NEDF break isospin symmetry. For now, we will also not account for the role of the Coulomb interaction on the pairing of the protons.

In an orbital-free approach, the role of pairing is revealed only by the presence of the odd-even staggering of the energy term. As shown in Table I, it has a small effect on the overall quality of global mass fits and it may be omitted as a variational parameter.

G. SeaLL1 NEDF

We characterize the parameters of the theory according to their significance for mass fits and dynamics. We define a parameter as *dominant* if varying this parameter by less than

[2]Subsequent to our introduction of terms $\propto n^{5/3}$ in Ref. [137], Reinhard [6] also considered these, but with a strength corresponding to a pure UFG, which is quantitatively very different from neutron matter. His conclusions, that the properties of the low-density neutron matter cannot be incorporated into the NEDF, differ from ours.

5% or so reduces the χ_E of the best fit by 0.1 MeV per nucleon. We define a parameter as *subdominant* if it can be varied by 10% or more with a similar decrease in the quality of the fit. We define a parameter as *unconstrained* if it can be set to zero at this level of accuracy.

Our analysis shows that a minimal orbital-free NEDF has four dominant parameters and two subdominant parameters, consistent with the analysis presented above.

Kinetic (none): The kinetic energy density $\mathcal{E}_{\rm kin}$ Eq. (11) contains no free parameters—just $\hbar$ and the bare nucleon masses m_n and m_p and the kinetic densities $\tau_{n,p}$. However, since the orbital-free approach depends on densities alone, an approximation of the kinetic energy densities in terms of densities introduces a single parameter κ. This is discussed in Secs. III A and III H.

Coulomb (none): The Coulomb interactions $\mathcal{E}_C$ Eq. (12) also contains no free parameter in either formulation. In principle, the proton and neutron form factors can be included but these have only a small effect. This is discussed in Sec. III B.

1 dominant, 1 subdominant: The homogeneous portion of the functional $\mathcal{E}_{\rm homo}$ Eq. (13) adds only three significant parameters. In principle, up to nine parameters a_j, b_j, and c_j for $j \in \{0,1,2\}$ describe the EoS for homogeneous nuclear matter. However, three of these nine (for $j = 2$) are fixed by the EoS of neutron matter as determined in *ab initio* calculations. Two of the remaining six parameters (a_0, and the combination of $a_1 - b_1 n_0^{1/3}$, where n_0 is symmetric matter saturation density) are found to be unconstrained at the level of changing the energy rms by $\delta\chi_E < 0.1$ MeV and are thus set to 0. In our full SeaLL1, we keep c_1 as a fitting parameter, although it is significantly less dominant than the others. We fix c_1 sometimes in the orbital-free theory to provide a reasonable description of the neutron skins; see Appendix B. Either c_1 or the linear combination $a_1 - b_1 n^{1/3}$ can be used to tune the density dependence of the symmetry energy.

This counting echoes the dominant and subdominant roles of the various nuclear saturation and symmetry properties in fitting masses. In particular, the dominant parameters fix the saturation density n_0, saturation energy ε_0, and quadratic symmetry energy S_2. The slope of the quadratic symmetry energy L_2 is subdominant as far as mass fits are concerned, but important for properties such as the neutron skin thickness, which is why we keep an additional parameter in the SeaLL1 functional.

Gradients (1 dominant): The gradient corrections $\mathcal{E}_\nabla n$ Eq. (18) add a single new parameter η_s.

Spin-orbit (1 subdominant): The spin-orbit coupling term $\mathcal{E}_{\rm SO}$ Eq. (20) add a single new parameter W_0. This parameter is subdominant for the mass fits, but is crucial for producing the shell structure of nuclei. In the orbital-free approach, this term is practically incorporated in the gradient contribution.

Pairing (1 parameter): The pairing interaction $\mathcal{E}_\Delta$ Eq. (21) adds an additional parameter g_0 in the orbital-based approach. Its contribution is practically incorporated in the homogeneous isoscalar terms in the orbital-free approach. A different parameter δ measuring the odd-even staggering is required for the orbital-free formulation. However, as is seen for the liquid drop models in Table I, this additional parameter is quite unconstrained.

The orbital-based approach is specified by seven parameters: b_0, c_0, characterizing isoscalar nuclear properties; b_1, c_1, defining the isovector nuclear properties; η_s, defining the surface tension; W_0, the strength of the isoscalar spin-orbit interaction; and the bare (unrenormalized) pairing coupling constant g. In the orbital-free approach, we are left with only four significant phenomenological parameters: η_s, b_0, c_0, and a linear combination $a_1 = b_1 n^{1/3}$, since c_1 is unconstrained. The orbital-free approach has the additional parameter κ controlling the Padé gradient approximation of the kinetic energy density.

The full form of the functional SeaLL1 is

$$\mathcal{E}[n_n,n_p] = \overbrace{\frac{\hbar^2}{2m}(\tau_n+\tau_p)}^{\text{kinetic}} + \overbrace{\sum_{j=0}^{2}(a_j n^{5/3} + b_j n^2 + c_j n^{7/3})\beta^{2j}}^{\text{homogeneous}} + \overbrace{\eta_s \sum_{q=n,p}\frac{\hbar^2}{2m}|\nabla n_q|^2}^{\text{gradient}}$$
$$+ \underbrace{W_0 \boldsymbol{J}\cdot\boldsymbol{\nabla} n}_{\text{spin-orbit}} + \underbrace{\sum_{q=n,p} g_{\rm eff}(\boldsymbol{r})|\nu_q(\boldsymbol{r})|^2}_{\text{pairing}} + \underbrace{\frac{e^2}{2}\int d^3\boldsymbol{r}'\frac{n_p(\boldsymbol{r})n_p(\boldsymbol{r}')}{|\boldsymbol{r}-\boldsymbol{r}'|} - \frac{e^2\pi}{4}\left[\frac{3n_p(\boldsymbol{r})}{\pi}\right]^{4/3}}_{\text{Coulomb}}. \quad (22)$$

The parameter values for the SeaLL1 functional are summarized in Table II. The seven shaded parameters b_0, c_0, b_1, c_1, η_s, W_0, and g are significant for fitting nuclear masses and radii. The other parameters are either fixed independently (e.g., by the properties of neutron matter) or have been determined to be unconstrained for mass fits through a principle component analysis described in Appendix B.

Our fitting strategy is described in detail in Appendix B, and we only recall here its most important characteristics. First, we explored the parameter space with a simplified version of the orbital-free NEDF. This NEDF is characterized by seven parameters (a_0, a_1, b_0, b_1, c_0, c_1, and η_s) which we fitted on $N_E = 2375$ experimentally measured atomic masses (with errors less than 1 MeV) and $N_r = 883$ nuclear charge

TABLE II. Best-fit parameters for the SeaLL1 functional and the orbital-free approximation (next column in italic when different). The errors quoted for the fit parameters should be interpreted as estimating by how much this parameter can be independently changed while refitting the other and incurring a cost of at most $\delta\chi_E < 0.1$ MeV.

	SSeaLL1	Hydro	Comments
n_0	0.154	*0.154*	Adjusted (see Fig. 5)
a_0	0	Same	Insignificant
b_0	−684.5(10)	*−685.6(2)*	
c_0	827.26	*828.76*	$2c_0 n_0^{\frac{2}{3}} = -\frac{3\hbar^2}{10m}(\frac{3\pi^2}{2})^{\frac{2}{3}} - \frac{3}{2}b_0 n_0^{\frac{1}{3}}$
a_1	64.3	*50.9*	$a_1 = n_0^{1/3} b_1$
b_1	119.9(61)	*94.9(14)*	
c_1	−256(25)	*−160.0*	Fixed in orbital-free theory
a_2	−96.8	*−83.5*	$a_2 = a_n - a_0 - a_1$
b_2	449.2	*475.2*	$b_2 = b_n - b_0 - b_1$
c_2	−461.7	*559.6*	$c_2 = c_n - c_0 - c_1$
a_n	−32.6	Same	From neutron matter EoS (16)
b_n	−115.4	Same	From neutron matter EoS (16)
c_n	109.1	Same	From neutron matter EoS (16)
η_s	3.93(15)	*3.370(50)*	
W_0	73.5(52)	*0.0*	Fixed in orbital-free theory
g_0	−200	N/A	g_0 fit in Ref. [145]
κ	N/A	*0.2*	Semiclassical (see Sec. III H)
$\frac{\hbar^2}{2m}$	20.7355	Same	Units (MeV = fm = 1)
e^2	1.43996	Same	cgs units ($4\pi\epsilon_0 = 1$)
χ_E	1.74	*3.04*	606 even-even nuclei
		2.86	2375 nuclei
χ_r	0.034	*0.038*	345 charge radii
		0.041	883 charge radii

radii as listed in Audi *et al.* [18], Wang *et al.* [19]. From this series of fits and its statistical analysis, we found that (i) the parameters a_0 and c_1 are unconstrained and can be set to zero and (ii) the mass and radii are sensitive only to a single linear combination of the parameters a_1 and b_1. The parameter c_1 can be used interchangeably with the linearly independent combination $a_1 - n_0^{1/3} b_1$ to control the slope L_2 of the symmetry energy, which also controls the neutron skin thickness of neutron-rich nuclei; see below Eq. (30b) and the related discussion in Sec. IV C. We will fix here $a_1 = n_0^{1/3} b_1$, where $n_0 = 0.154\,\text{fm}^{-3}$ is the saturation density (see discussion below) and c_1 to obtain a reasonable neutron skin thickness in ^{208}Pb. With $c_1 = 0$, the neutron skin thickness of ^{208}Pb is about 0.2 fm and the χ_E increases by at most 0.1 MeV.

The next step consists in minimizing the residuals $\chi_E^2 = \sum |E_{N,Z} - E(N,Z)|^2/N_E$ over the $N_E = 196$ spherical even-even nuclei with $A \geqslant 16$ measured (not extrapolated) from Audi *et al.* [18], Wang *et al.* [19] with the full orbital-based functional. This involves adjusting the five dominant parameters shaded in Table II— the saturation density having been fixed from the study of charge radii. Note that the pairing parameter g_0 is fixed at the value suggested in Ref. [145]: Although this is in principle a fitting parameter, it plays only a minor role in global mass fits as discussed in the introduction. The SeaLL1 parameters of the orbital-based NEDF yield $\chi_E = 1.51$ MeV over the $N_E = 196$ spherical even-even nuclei, while the orbital-free NEDF yield $\chi_E = 2.86$ MeV over $N_E = 2375$ nuclei.[3] The pairing fields were treated using the renormalization procedure described in Refs. [144,145] with a cutoff energy of 100 MeV.

TABLE III. Saturation, symmetry, and neutron skin properties for SeaLL1. All values in MeV unless otherwise specified.

ρ_0 [fm^{-3}]	$-\epsilon_0$	K_0	S	S_2	L	L_2	Neutron skin ^{208}Pb [fm]	Neutron skin ^{48}Ca [fm]
0.154	15.6	230	31.7	27.7	32.4	32	0.131	0.159

As discussed in Appendix B, we find that fitting the binding energies alone in the orbital-free approach results in quite a low saturation density $n_0 \approx 0.14\,\text{fm}^{-3}$, and a poorer fit to both charge radii and density profiles. To explore the influence of saturation density n_0 on the quality of the fit, we performed mass-only fits for the remaining five parameters with various saturation densities n_0 ranging from 0.15 to 0.16 fm^{-3}. For each fit, we also calculate the rms radii residuals $\chi_r^2 = \sum |\delta r|^2/N_r$ for the $N_r = 123$ corresponding nuclei in Ref. [118]. These results are shown in Fig. 5, which demonstrates that the charge radii strongly prefer $n_0 \approx 0.155\,\text{fm}^{-3}$ in contrast to the rather weak lower bias from the mass fits. To incorporate this preference in our fits, we fix the saturation density $n_0 = 0.154\,\text{fm}^{-3}$ by adjusting c_0 using the Eq. (B4). This represents a compromise between the two biases where both χ_E and χ_r increase by about 10%. With this fixed value of n_0, we fit the remaining five parameters of the SeaLL1 functional by minimizing only χ_E over the $N_E = 196$ spherical even-even nuclei as summarized in Table II.

H. Orbital-free functional

Although we advocate working with the full orbital-based SeaLL1 functional presented above, for tasks such as globally fitting mass parameters, one can work with a much simpler orbital-free formulation. The main challenge in formulating an orbital-free theory is to express terms with the auxiliary densities $\tau_{n,p}$, $\boldsymbol{J}_{n,p}$, and $\boldsymbol{j}_{n,p}$ by an appropriate functional of the number densities $n_{n,p}$. Although formally possible, it is still an open research question as to how best reduce an orbital-based DFT to an orbital-free version. We discuss in more detail our approach based on a semiclassical approximation in Appendix A. To summarize here, we suggest using the following combination for the kinetic and spin-orbit contributions in an orbital-free theory:

$$\mathcal{E}_{\text{kin}}[n_n,n_p] + \mathcal{E}_{\text{SO}}[n_n,n_p] = (\text{orbital-free})$$
$$= \frac{\hbar^2}{2m}\sum_{q=n,p}\tau_{\text{TF}}[n_q]F(X_q) - \frac{W_0^2}{2}\frac{2m}{\hbar^2}n|\nabla n|^2, \quad (23a)$$

[3] At first sight, it is surprising that the value of χ_E in the orbital-free approach over 606 even-even nuclei is larger than the value obtained for 2375 nuclei. The reason is simple: The value $\chi_E = 3.04$ MeV was obtained with parameters obtained by fine-tuning the masses for spherical nuclei only in the orbital-based approach. This does not minimize the value of χ_E in the orbital-free approach.

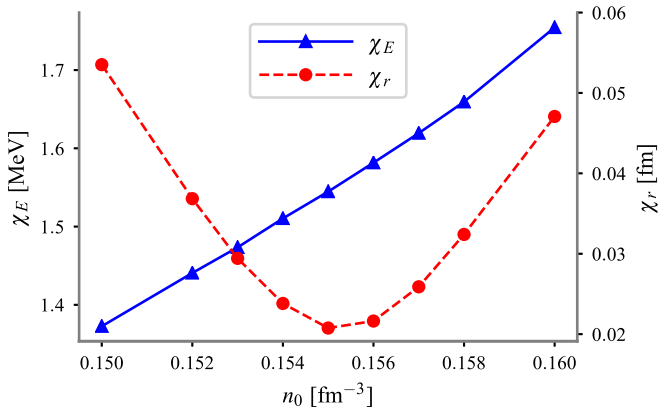

FIG. 5. Saturation density n_0 dependence of the energy residual χ_E and charge radii residual χ_r of the SeaLL1 functional. After holding n_0 fixed (through the parameter c_0), the remaining five shaded parameters in Table II were fit by minimizing only $\chi_E^2 = \sum |E_{N,Z} - E(N,Z)|^2/N_E$ over the $N_E = 196$ spherical even-even nuclei with $A \geqslant 16$ measured (not extrapolated) from Audi *et al.* [18], Wang *et al.* [19]. The value $n_0 = 0.154\,\mathrm{fm}^{-3}$ fixed in the SeaLL1 functional represents a compromise between these residuals here both χ_E and χ_r increase by about 10%.

where

$$F(X) = \frac{1 + (1+\kappa)X + 9\kappa X^2}{1 + \kappa X}, \quad X = \frac{\tau_2[n]}{\tau_{\mathrm{TF}}[n]}, \tag{23b}$$

$$\tau_{\mathrm{TF}}[n] = \frac{3}{5}(3\pi^2)^{2/3} n^{5/3}, \quad \tau_2[n] = \frac{1}{9}|\nabla\sqrt{n}|^2. \tag{23c}$$

The ratio X characterizes the size of the gradients in the system in terms of the leading τ_{TF} and subleading τ_2 terms of the semiclassical expansion [2,31,151] of the kinetic density τ. The Padé approximant $F(X)$ suggested by DePristo and Kress [152] and advocated in Ref. [2] interpolates between the semiclassical limit $X \ll 1$ valid in the core of large nuclei, and the approximation $\tau \approx \tau_{\mathrm{TF}} + |\nabla\sqrt{n}|^2$ introduced by Weizsäcker [11], which correctly reproduces the asymptotic fall off of the density when $X \gg 1$. When spin orbit is missing, $\tau_{\mathrm{TF}}[n_q]F(X_q)$ gives a semiclassical approximation of the kinetic density τ. This approximation requires a single additional parameter κ. The value of κ can be chosen approximately by comparisons between τ and $\tau_{\mathrm{TF}}[n_q]F(X_q)$, and between their resulting kinetic energies E_{kin}, for the same set of single-particle wave functions. We found $\kappa \approx 0.2$ will give a reasonable semiclassical approximation for τ and E_{kin}.

The semiclassical spin-orbit contribution is suggested by Brack *et al.* [57], which brings a parameter W_0 corresponding to the one in Eq. (20). Like the full self-consistent theory, this parameter is also subdominant for the mass fits and its contribution can be incorporated in the gradient term. Furthermore, due to the missing of shell structure in the orbital-free theory, this parameter is even more unconstrained.

The orbital-free formulation of the NEDF requires the additional parameter κ to approximate the gradient corrections. As discussed above we choose $\kappa = 0.2$. Following SeaLL1, we fix the saturation density $n_0 = 0.154\,\mathrm{fm}^{-3}$, and fit the three parameters b_0, b_1, and η_s shaded in Table II. The spin-orbit contribution was absorbed in the gradient term and if desired the unconstrained parameter c_1 can be used to fix the neutron skin thickness. The parameter values are determined by performing the same least squares minimization of the binding energy residuals as SeaLL1, but over all $N_E = 2375$ nuclei (including the deformed even-even, odd-even, and odd-odd ones) with $A \geqslant 16$ measured from Audi *et al.* [18], Wang *et al.* [19].

The parameter values and rms residuals of orbital-free theory are also summarized in Table II. As expected, the rms residuals $\chi_E = 2.86\,\mathrm{MeV}$ is larger than the χ_E of SeaLL1 due to the lack of shell corrections in the orbital-free theory, but are comparable with results from the liquid-drop formula in Table I.

I. Principal component analysis

The parameters listed in Table II are highly correlated. To analyze these, we consider as significant changes $\delta\chi_E \approx 0.1\,\mathrm{MeV}$ since this is the typical level of sensitivity of the mass fits. We keep the changes relatively small because otherwise the model is not well approximated by a quadratic error model if $\delta\chi_E > 0.1\,\mathrm{MeV}$. Numerically we find that even 0.1 MeV is too large but yields qualitatively correct information after a full refitting. Note that $\delta(\chi_E^2) = (\chi_E + \delta\chi_E)^2 - \chi_E^2 = 2\,\chi_E\,\delta\chi_E + (\delta\chi_E)^2$, so we must normalize $\delta(\chi_E^2)$ by $2\,\chi_E \times 0.1\,\mathrm{MeV}$ in order to consider changes $\delta\chi_E \approx 0.1\,\mathrm{MeV}$.

To compare the parameters in a meaningful way, we must make them dimensionless and of order unity. We do this by scaling them with appropriate powers of $n_0 = 0.154\,\mathrm{fm}^{-3}$ and $\varepsilon_F = \frac{\hbar^2}{2m}(3\pi^2 n_0/2)^{2/3} = 35.29420\,\mathrm{MeV}$, which we take as fixed parameters close to the saturation values:

$$\tilde{a}_j = \frac{a_j n_0^{2/3}}{\varepsilon_F}, \quad \tilde{b}_j = \frac{b_j n_0}{\varepsilon_F}, \quad \tilde{c}_j = \frac{a_j n_0^{4/3}}{\varepsilon_F}. \tag{24}$$

(It is important to retain a significant number of digits for isoscalar quantities, as it will be come more clear below.) In particular, we consider the covariance matrix $\boldsymbol{C}$ such that the residual deviation is

$$\frac{\delta(\chi_E^2)}{2\chi_E \times 0.1\,\mathrm{MeV}} \approx \boldsymbol{\delta}^T \boldsymbol{C}^{-1} \boldsymbol{\delta} = \sum_n \frac{(\delta p_n)^2}{\lambda_n^2}. \tag{25a}$$

where $\boldsymbol{\delta}$ is the deviations vector of the dimensionless parameters Eq. (24) from their best fit values as listed in Table II, and we have diagonalized $\boldsymbol{C}\mathbf{v}_n = \lambda_n^2 \mathbf{v}_n$ to obtain the principal components p_n

$$p_n = \boldsymbol{v}_n(\tilde{a}_0\ \tilde{b}_0\ \ldots\ \tilde{\eta}_s\ \tilde{W}_0). \tag{25b}$$

Since the parameters are of order unity, we may directly consider the λ_n as a measure of the errors: Changing p_n by λ_n will affect the fit on the scale of $\delta\chi_E \approx 0.1\,\mathrm{MeV}$. Therefore, the smaller the value of the parameter λ_n, the more precisely the fit to nuclear masses constrains the value of the corresponding linear combination of NEDF parameters. A similar approach was used by Bertsch *et al.* [153] in the analysis of Skyrme NEDFs.

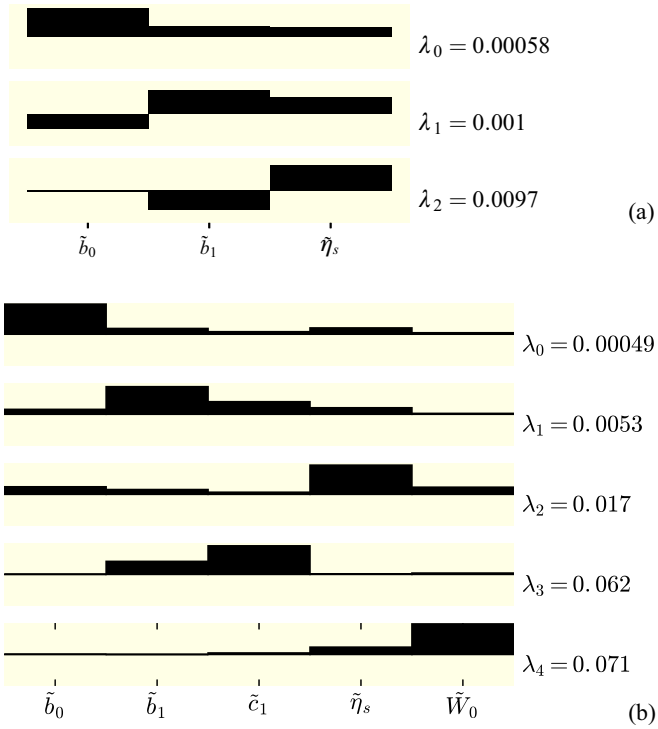

FIG. 6. The principal component analysis of the SeaLL1 NEDF in the case of the orbital-free (a) and orbital-based (b) approach.

In Fig. 6, we show a principal component analysis of the SeaLL1 functional. The orbital-based analysis includes only 196 spherical even-even nuclei used to fine-tune the parameters of the functional, while the analysis of the orbital-free functional includes all 2375 nuclei as described in Table I. Their features can be understood in terms of the saturation and symmetry parameters; see Eqs. (29):

$$S = \frac{\mathcal{E}(n_0,0) - \mathcal{E}(n_0/2,n_0/2)}{n_0}, \tag{26a}$$

$$L = 3n\frac{d}{dn}\left[\frac{\mathcal{E}(n,0)}{n}\right]\Bigg|_{n_0} = 3n_0\varepsilon_n'(n_0)$$
$$= \frac{6}{5}\frac{\hbar^2}{2m}(3\pi^2 n_0)^{2/3} + 2a_n n_0^{2/3} + 3b_n n_0 + 4c_n n_0^{4/3}. \tag{26b}$$

where $\varepsilon_n(n)$ is the energy per particle of the neutron EoS (15a). Since the saturation density n_0 minimizes the energy of symmetric matter, the slope of the full symmetry energy L at n_0 depends only on the EoS of pure neutron matter. Thus, the QMC neutron EoS alone fixes the global density dependence of the symmetry energy $L = 3n_0\varepsilon_n'(n_0) \approx 30\,\mathrm{MeV}$. We may express these as follows:

$$\frac{\varepsilon_0}{\varepsilon_F} = +\frac{3}{5} + \tilde{a}_0 + \tilde{b}_0 + \tilde{c}_0, \tag{27a}$$

$$0 = +\frac{3}{5} + \tilde{a}_0 + \frac{3}{2}\tilde{b}_0 + 2\tilde{c}_0, \tag{27b}$$

$$\frac{K_0}{\varepsilon_F} = -\frac{6}{5} - 2\tilde{a}_0 + 4\tilde{c}_0, \tag{27c}$$

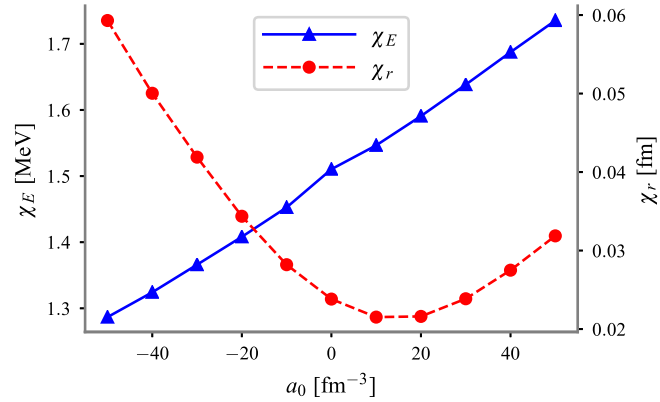

FIG. 7. The changes in χ_E and χ_r for the $N_E = 196$ even-even spherical nuclei with $A \geqslant 16$, similarly to Fig. 5 as a function of the fixed parameter a_0, while the rest of the seven parameters of SeaLL1 specified in Table II are optimized.

$$\frac{S}{\varepsilon_F} = \frac{3}{5}(2^{2/3} - 1) + (\tilde{a}_1 + \tilde{b}_1 + \tilde{c}_1) + (\tilde{a}_2 + \tilde{b}_2 + \tilde{c}_2), \tag{27d}$$

$$\frac{L}{\varepsilon_F} = \frac{6}{5}2^{2/3} + 2\tilde{a}_n + 3\tilde{b}_n + 4\tilde{c}_n, \tag{27e}$$

where K_0 is the isoscalar incompressibility. The most significant component p_0 in both fits is the sum of the $j = 0$ coefficients $\tilde{a}_0 + \tilde{b}_0 + \tilde{c}_0$ which fixes the saturation energy ε_0 Eq. (27a) (see also Fig. 21). [Remember that we have chosen $a_0 = 0$ and that c_0 is determined from Eq. (27b).] Next are mixtures of η_s and the symmetry energy S, Eq. (27d), which are correlated by the finite size of the nuclei; the latter is the sum of the $j = 1$ coefficients $\tilde{a}_1 + \tilde{b}_1 + \tilde{c}_1$. While we have chosen to keep the value of the parameter $a_0 = 0$, its value can be varied without affecting significantly the quality of the overall mass and charge radii fit; see Fig. 7. By changing the adopted value $a_0 = \pm 20\mathrm{fm}^{-3}$ and keeping ε_0 and the saturation density fixed, one can change the incompressibility by $\delta K_0 = \pm 2\delta\tilde{a}_0\varepsilon_F = \pm 2\delta a_0 n_0^{2/3} \approx \pm 23\,\mathrm{MeV}$.

The power of this kind of analysis resides in formulating a "power-counting" scheme, which organizes the various linear combinations of parameters in the order of relevance in the mass fit.

IV. PHYSICAL PROPERTIES

A. Global mass table

Since our orbital-based NEDF was fit on spherical even-even nuclei only, we validate its predictive power by performing a fully microscopic calculation of the nuclear binding energies of 606 even-even nuclei with $A \geqslant 16$ in Refs. [18,19]. We used an extension of the axial DFT solver HFBTHO code [154–156] that includes the SeaLL1 and the regularization of the pairing channel [144]. Calculations were performed in a deformed basis of 20 harmonic oscillator shells. In the pairing channel, a cutoff of 100 MeV was adopted in accordance with Ref. [145].

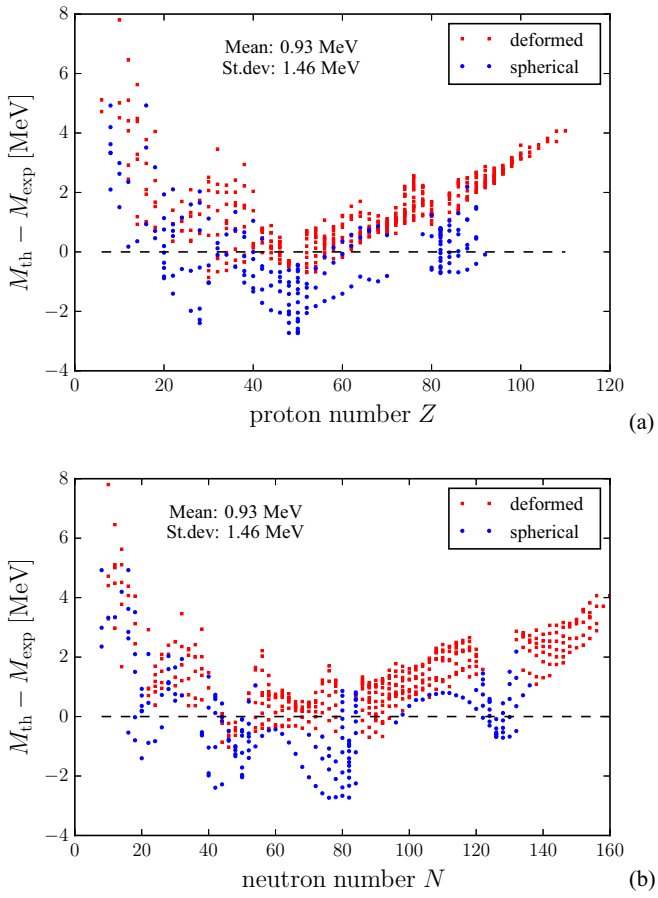

FIG. 8. Mass residuals between SeaLL1 and measured masses for 606 even-even nuclei, of which 410 are deformed nuclei and 196 are spherical nuclei, plotted with red squares and blue bullets respectively as a function of proton number Z (a) and neutron number N (b).

Figure 8 shows the residuals of the nuclear masses calculated with SeaLL1 with respect to the experimental values of these even-even nuclei. The rms of the residuals is $\chi_E = 1.74$ MeV. Besides the larger residuals in light nuclei, we observe the typical arclike features common to many NEDF calculations, both for isotonic and isotopic chains. The poor performance of SeaLL1 in light nuclei is likely related to the center-of-mass corrections (not accounted for here) and is also observed in the UNEDF functionals [73–75]. Since the center-of-mass correction is larger for light nuclei, our parameter fit limited to spherical nuclei leads to an underestimate of the masses of heavier spherical nuclei; see Fig. 8.

Overall the masses have a bias $\epsilon_E = \langle \delta E \rangle = 0.93$ MeV and a standard deviation $\sigma_E = 1.74$ MeV; see Fig. 9. This bias enters the rms error $\chi_E^2 = \sigma_E^2 + \epsilon_E^2$ which leads to a value of $\chi_E = 1.46$ MeV. This σ_E is an upper estimate of the rms energy χ_E we expect if the SeaLL1 parameters would have been instead fitted to all even-even nuclei.

The residuals for the two-nucleon separation energies for the same set of even-even nuclei are shown in Fig. 10, and they are naturally less affected by the errors induced by errors on binding energies.

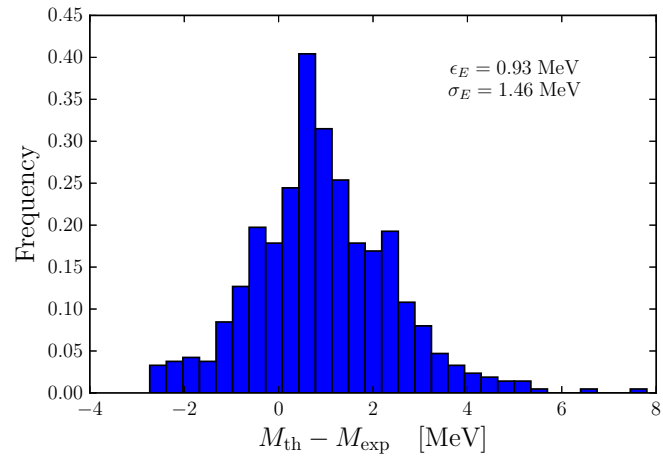

FIG. 9. The histogram of the mass residuals between SeaLL1 and experiment for 606 even-even nuclei.

B. Charge radii and density distribution

Using the parameters determined from the mass fits, SeaLL1 also models the neutron and proton densities in the nuclei, allowing us to extract the charge densities for these

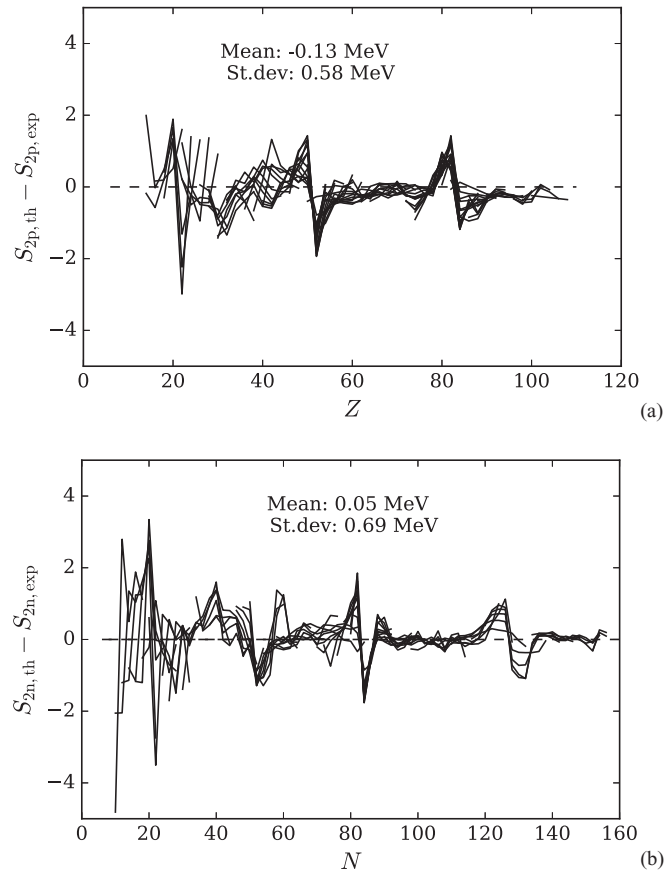

FIG. 10. The residual of the two-nucleon separation energies between SeaLL1 and experiment for 606 even-even nuclei: $S_{2p}(Z)$ for constant N (a) and $S_{2n}(N)$ for constant Z (b) chains connected by lines.

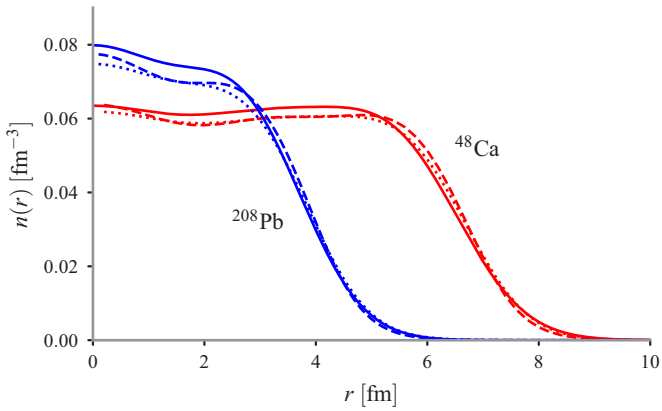

FIG. 11. The calculated proton $n_p(r)$ (dashed) and charge $n_{\rm ch}(r)$ (dotted) densities for ^{48}Ca (red) and ^{208}Pb (blue), calculated with SeaLL1 compared to charge densities (solid) extracted from electron scattering experiments [157].

nuclei using Eq. (12c). As a good benchmark, in Fig. 11 we compare the proton and charge densities of ^{48}Ca and ^{208}Pb calculated with SeaLL1 with the charge densities extracted from electron scattering experiments [157]. The calculated ^{208}Pb has a slightly larger radius and slightly smaller diffuseness compared to those extracted from data, which is consistent with the charge radii comparison between SeaLL1 and experiment in Fig. 12.

The residuals of radii for 345 matching even-even nuclei in Ref. [118] are also calculated, with a bias $\epsilon_r = 0.022$ fm and a standard deviation $\sigma_r = 0.025$ fm, which gives a rms residual of $\chi_r = 0.034$ fm, as shown in Fig. 12.

C. Symmetry energy and neutron skin thickness

The isoscalar parameters $j = 0$ and quadratic isovector parameters $j = 1$ (β^2) may be directly related to the saturation and symmetry properties respectively by expanding the energy per nucleon of homogeneous nuclear matter Eq. (14) about the symmetric saturation point $n_n = n_p = n_0/2$:

$$\frac{\mathcal{E}(n_n,n_p)}{n} = \epsilon_0(n) + \epsilon_2(n)\beta^2 + \epsilon_4(n)\beta^4 + O(\beta^6). \quad (28)$$

The saturation density n_0, energy per nucleon ε_0, and incompressibility K_0 are then defined by the minimum $\varepsilon_0'(n_0) = 0$, and depend only on the $j = 0$ isoscalar parameters a_0, b_0, and c_0. Expanding about n_0 in $\delta = (n - n_0)/3n_0$ and in powers of $\beta = (n_n - n_p)/n$, one can define various "local" contributions to the symmetry energy $S_{2,4}$, its density-dependent slope $L_{2,4}$, etc.:

$$\begin{aligned}
\epsilon_0(n) &= \tfrac{6}{5}\varepsilon_F + a_0 n^{2/3} + b_0 n + c_0 n^{4/3} \\
&= \varepsilon_0 + \tfrac{1}{2}K_0\delta^2 + O(\delta^3), \\
\epsilon_2(n) &= -\tfrac{4}{15}\varepsilon_F + a_1 n^{2/3} + b_1 n + c_1 n^{4/3} \\
&= S_2 + L_2\delta + \tfrac{1}{2}K_2\delta^2 + O(\delta^3), \\
\epsilon_4(n) &= S_4 + L_4\delta + \tfrac{1}{2}K_4\delta^2 + O(\delta^3). \qquad (29)
\end{aligned}$$

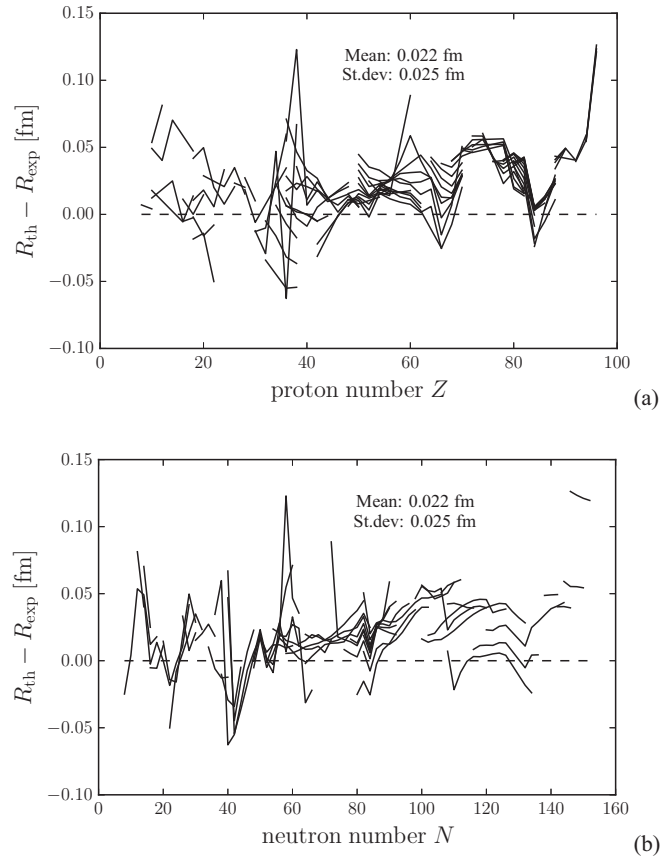

FIG. 12. Radii residuals between SeaLL1 and experiment for 345 even-even nuclei. Isotonic (a) and isotopic (b) chains are connected by lines.

Since we include also quartic terms β^4, we must differentiate between these local symmetry parameters S_2, L_2, etc. and the full symmetry parameters defined as the difference between symmetric matter and pure neutron matter (see also the discussion of Lattimer [158]). Using $a_1 = b_1 n_0^{/3}$ (see Table II), we obtain the values for S_2 and L_2 given by relations

$$S_2 = \tfrac{1}{3}\varepsilon_F + 2a_1 n_0^{2/3} + c_1 n_0^{4/3}, \quad (30a)$$

$$L_2 = \tfrac{2}{3}\varepsilon_F + 5a_1 n_0^{2/3} + 4c_1 n_0^{4/3}. \quad (30b)$$

As shown in Table II), the binding energy of nuclear matter and the symmetry energy predicted by SeaLL1 fit agrees well with the value obtained with the mass formula (2). Our fits generally estimate the slope of the symmetry energy L_2 from 29 to 36 MeV. However, our fits with orbital-free functionals demonstrate that this quantity is not well constrained by the masses and can be adjusted independently with the combination $a_1 - b_1 n_0^{1/3}$ and/or coefficient c_1; see also the discussion in Appendix B and Table V.

We also compute the neutron skin thickness of ^{48}Ca and ^{208}Pb, for which precision measurements CREX and PREX are under way; see Ref. [159] for details. The ^{208}Pb neutron skin is consistent with the value $0.156^{+0.025}_{-0.021}$ fm of Tamii *et al.* [160] extracted from measurements of the dipole polarizability using the method suggested by Reinhard and Nazarewicz [161] based on observed correlations between these two quantities

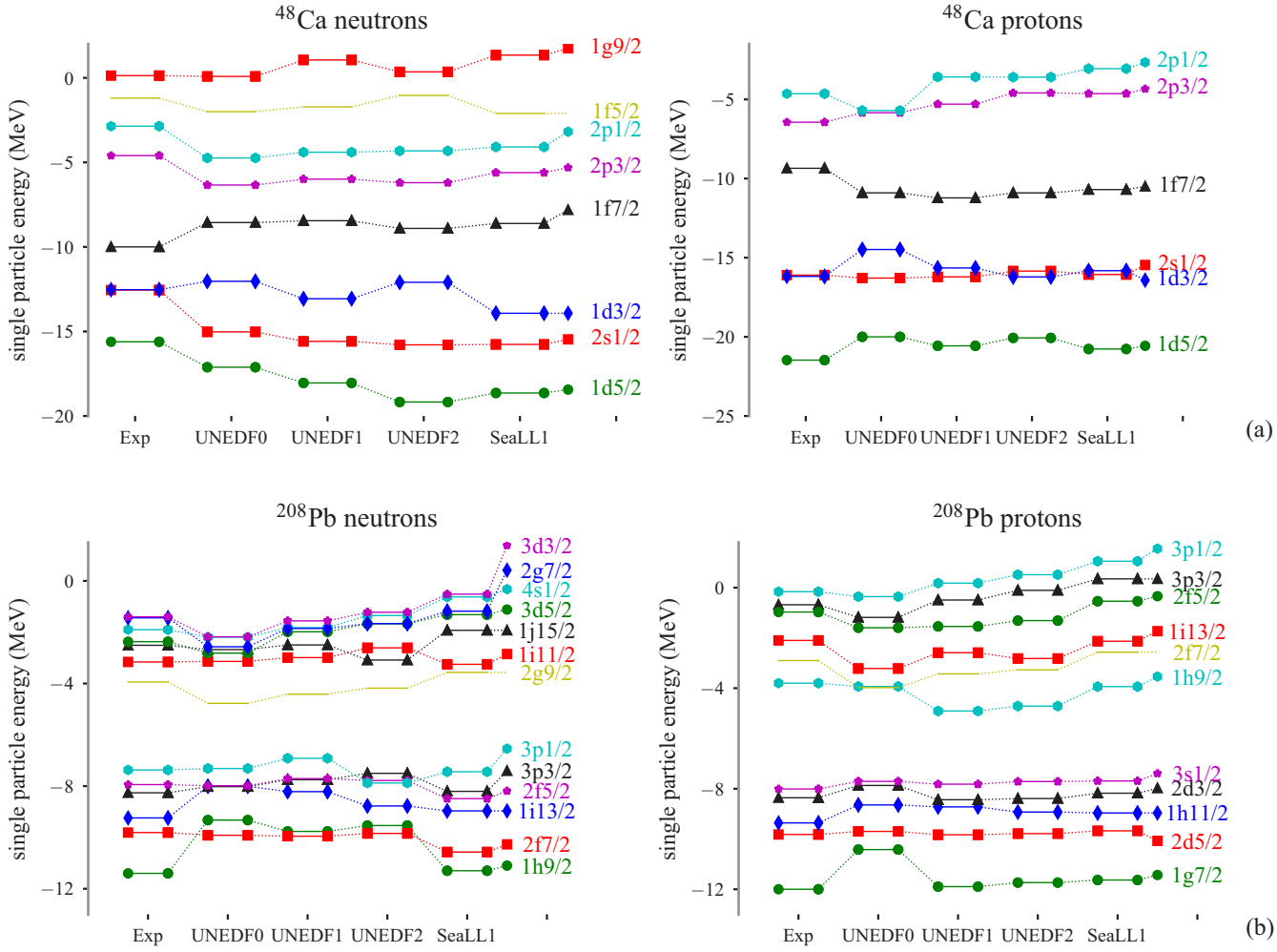

FIG. 13. Single particle energies in ^{48}Ca (a) and ^{208}Pb (b) for a variety of functionals UNEDF0-2 [73–75] and SeaLL1 (calculated using the HFBTHO DFT solver [154]).

in Skyrme models, and with the recent measurement of 0.15(3) fm [162]. Here again, our work with orbital-free functionals showed that the neutron skin is controlled by the same combination $a_1 - b_1 n_0^{1/3}$ as L_2, and hence is unconstrained by the masses.

D. Spherical shell structure

Shell structure is a fundamental property of atomic nuclei. In an independent-particle picture, the shell structure can be associated with the single-particle spectra of the mean-field potential. Reproducing the correct ordering and distribution of single-particle levels is essential for nuclear structure theories, and also important for the application of the NEDF in nuclear dynamics, such as nuclear fission and collision. Figure 13 display the single-particle levels for neutrons and protons in ^{48}Ca and ^{208}Pb for the SeaLL1, UNEDF0, UNEDF1, and UNEDF2 NEDF. Single-particle energies were obtained by blocking calculations in the neighboring odd nuclei following the procedure outlined in Refs. [74,75].

In ^{48}Ca, the rms deviations for the single-particle energies of UNEDF0, UNEDF1, UNEDF2, and SeaLL1 with the empirical values (Exp) [163] are 1.50,1.71,1.92, and 1.88 MeV and 1.22,1.08,1.22, and 1.17 MeV for neutrons and protons, respectively. In ^{208}Pb, these are 0.82,0.61,0.69, and 0.62 MeV and 0.77,0.49,0.50 and 0.54 MeV for neutrons and protons, respectively.

Compared with the empirical values, the $N = 28$ and $Z = 20$ gaps in ^{48}Ca are clearly too small with SeaLL1. The single-particle proton levels in ^{208}Pb show that the $Z = 82$ gap is also smaller in SeaLL1. Such patterns are also observed in UNEDF2 functional which, however, included single-particle spin-orbit splittings in their fit [75]. This might point to the need to consider the contribution from the isovector spin-orbit contribution in Eq. (37) proportional to W_1. Overall, however, the SeaLL1 single-particle spectra, as quantified in the corresponding rms, are of better quality than UNEDF2.

E. Fission pathway of ^{240}Pu

One of the important applications of nuclear DFT is the description of nuclear fission [164]. In this context, characteristics of fission pathways such as the excitation energy of fission isomers or the height of fission barriers are often used

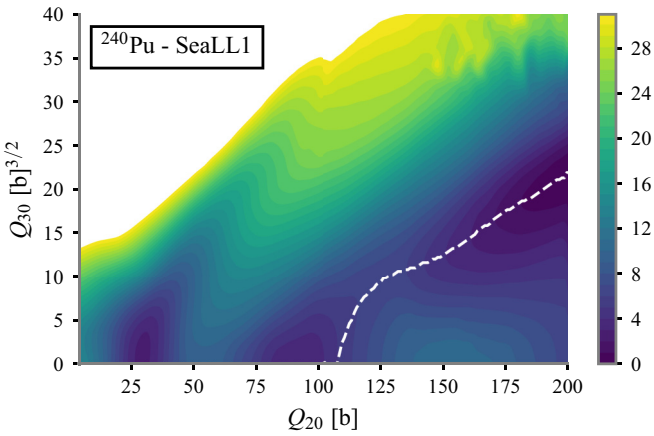

FIG. 14. Two-dimensional potential energy surface of ^{240}Pu with SeaLL1 for $0 \leqslant Q_{20} \leqslant 200\,\mathrm{b}, 0 \leqslant Q_{30} \leqslant 40\,\mathrm{b}^{3/2}$. The least-energy fission path is marked as white dashed line.

to gauge the predictive power of NEDF. To this purpose, we computed the potential energy surface of ^{240}Pu with SeaLL1 by performing constrained HFB calculations with constraints on the mass quadrupole Q_{20} and octuple moment Q_{30} in the region $0 \leqslant Q_{20} \leqslant 200\,\mathrm{b}, 0 \leqslant Q_{30} \leqslant 40\,\mathrm{b}^{3/2}$. The definitions and units of Q_{20} and Q_{30} are consistent with Ref. [165] and the characteristics of the harmonic oscillator (HO) basis used in the calculation are the same as in Ref. [166]. All calculations were performed with the HFBTHO DFT solver [154]. The results are shown in Fig. 14.

From this two-dimensional potential energy surface, we extracted the least-energy trajectory starting at the ground-state. Figure 15 shows the potential energy curve of ^{240}Pu as a function of Q_{20} along this (asymmetric) fission pathway. To gain an idea of the quality of SeaLL1, we repeated the calculations with the SkM* [167], and UNEDF1-HFB [168] energy functionals, both of which were designed for fission studies.

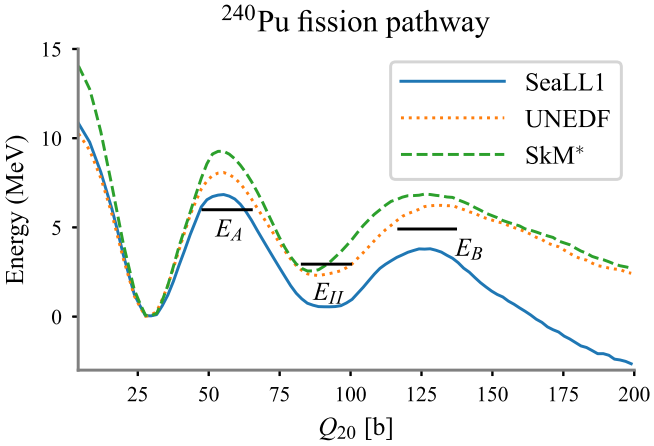

FIG. 15. Fission pathway for ^{240}Pu along the mass quadrupole moment Q_{20} calculated using HFBTHO with SeaLL1, SkM*, and UNEDF1-HFB.

Since all these calculations were done with the HFBTHO DFT solver, triaxiality is not included and the height of the first fission barrier is typically overestimated for all three functionals by about 2 MeV [166]. Compared with SkM* and UNEDF1-HFB, SeaLL1 underestimates the excitation energy of the fission isomer ($E_I = 0.54$ MeV compared with an experimental value of 2.8 MeV) and the heights of both fission barriers ($E_A = 6.84$ MeV vs 6.05 MeV, and $E_B = 4.20$ MeV vs 5.15 MeV, respectively, for the inner and outer barriers) agree within 1 MeV.

This result deserves a few comments. First, we note that both SkM* and UNEDF1 were constrained specifically on the height of the first fission barrier (SkM*) or excitation energy of the fission isomer (UNEDF1). By contrast, we did not include any specific information for nuclei at large deformation in the fit protocol of SeaLL1. It is therefore very encouraging that, without any such constraint, the resulting NEDF is still in reasonable agreement with experimental results, especially the height of the two barriers. Our results are definitely better than predictions with, e.g., SLy4 [142], another popular NEDF without constraints on large deformations, which predicts the second fission barrier much higher than the first one [173]. Second, the error in fission barriers of NEDFs designed for fission can reach 2.5 MeV, as can be seen in Ref. [75] where fission barriers and the energy of the second isomer in chains of Ra, Th, U, Pu, Cm, and Cf, are compared to the UNEDF1-2, Gogny D1S [174], and FRLDM [175] functionals. We also point to a recent study of the surface energy coefficient a_s [see Eq. (1)] for 76 parametrizations of the Skyrme NEDF [176] and the rather complex interplay between the roles of the shell effects and of the surface energy on the values of the fission barriers in ^{240}Pu. The energy of the fission isomer and the height of the outer fission barrier are shown to vary by several MeVs with respect to the ground-state energy. Third, we should repeat here the usual warnings about taking at face value calculations of fission barrier heights: These quantities are not physical observables but are extracted from data in a (very) model-dependent manner.

Ultimately, the predictive power of SeaLL1 (or any other NEDF for that matter) should be judged on their ability to reproduce fission half-lives, or fission fragment distributions. As recently shown [177], within a real-time formulation of DFT extended to the time-dependent superfluid local density approximation (TDSLDA) [117], the SeaLL1 NEDF provides a very accurate description of the features of the dynamics for the induced fission in ^{240}Pu, comparable to that of SkM*, whose fission properties are similar to UNEDF1-HFB.

F. Neutron and proton drip lines

In Fig. 16, we compare the proton and neutron drip lines obtained with SeaLL1 against the predictions of UNEDF1, as well as those obtained with other Skyrme parametrizations extracted from the supplemental data of Erler *et al.* [169] and using FRLDM [66]. SeaLL1 predicts that there are 7716 stable nuclei with $Z \leqslant 120$, as compared with 8450 in case of UNEDF1 and 7212 for SLy4. The position of the neutron drip line may dramatically impact the astrophysical r-process, which is predicted to follow lines of constant separation energy

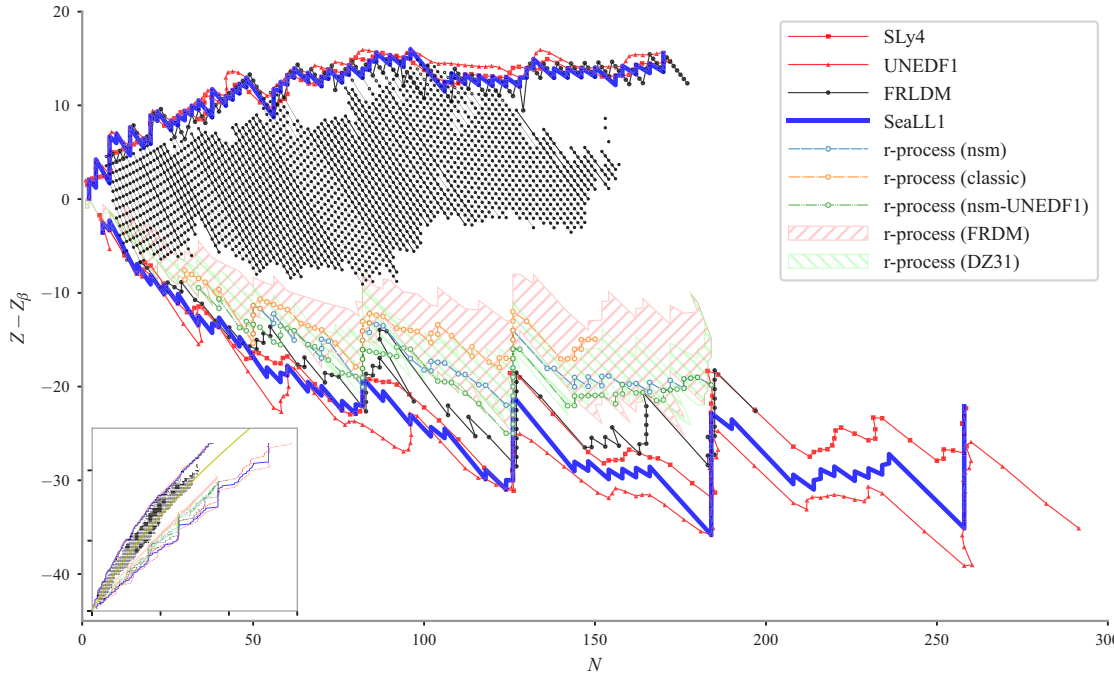

FIG. 16. Fully self-consistent calculations of the proton and neutron driplines for the SeaLL1 NEDF (thick blue line) compared with predictions of the functionals SLy4 and UNEDF1 extracted from Ref. [169], and FRLDM [66]. The vertical axis is shifted by the approximate β-stability line $Z_\beta(N)$ which minimizes Eq. (1) at constant A with parameters from Table I: $\partial_Z E(A-Z,Z)|_{Z=Z_\beta} = 0$, $Z_\beta = A/(2 + a_C A^{2/3}/2a_I)$. The inset shows the usual Z vs N plot, with the $Z = Z_\beta(N)$ curve as a solid (yellow) line. The 2375 nuclear masses from Refs. [18,19] are displayed as dots. We have plotted possible r-process trajectories predicted to be realized in the case of two neutron star mergers [16,17] (red circles), in a classical hot $(n,\gamma) \leftrightarrow (\gamma,n)$ in equilibrium r-process [170] (green circles) with the FRDM model [66] and neutron star merger with the UNEDF1 functional [74] (blue circles). With pink and green bands we display the r-process paths obtained by Mendoza-Temis *et al.* [171] under various conditions using the FRDM model [66] and the Duflo-Zuker model [172].

in close proximity to the neutron dripline [178,179]. Meyer [178] considered neutron star ejecta as the site of r-process nucleosynthesis and determined that the reaction flow is very close to the dripline. One should keep in mind also that the precise position of the drip lines is difficult to pinpoint, since the fluctuations, comparable to the theoretical errors, in the separation energies have large fluctuations in their vicinity. Even though his simulations were performed for relatively cold matter (recent simulations seem to indicate that the star material is somewhat heated [180,181]), it will be interesting to simulate the r-process using SeaLL1. The predicted position of the neutron dripline will likely affect the structure of the neutron star crust inferred from older studies [91–94,182–186]. The corresponding increase in the neutron skin thickness will also affect the profile and the pinning energy of quantized vortices in the neutron star crust [187–193].

Fusion cross sections [194,195] will also be significantly altered, particularly in stellar environments where neutron-rich nuclei fuse via pycnonuclear reactions [196,197] and where the neutron gas surrounding nuclei leads to their swelling [198]. A thicker neutron skin with further enhance this effect.

G. Neutron star crust

The baryon matter in the Universe organizes itself based on the short-range nuclear attraction and the long-range Couloumb repulsion. At densities much lower than the nuclear saturation density, $n \approx 0.16\,\mathrm{fm}^{-3}$, the nuclear and atomic length scales are well separated, and nuclei in matter are expected to form the Coulomb lattice embedded in the neutron-electron seas that minimizes the Coulomb interaction energy. At subsaturation baryon densities, $0.1n_0 < n < 0.8n_0$, conditions expected in the bottom layers of the inner crust of neutron star, there is a strong competition between the Coulomb and strong interactions, which leads to the emergence of various complex structures with similar energies that are collectively referred to as "nuclear pasta" [184,185,199]. Pasta nuclei are eventually dissolved into uniform matter at a certain nucleon density below n_0. Existence of pasta phases would modify some important processes by changing the hydrodynamic properties and the neutrino opacity in core-collapse supernovae [200,201] and protoneutron stars [202,203]. Also, the pasta phases may influence neutron star quakes and pulsar glitches via the change of mechanical properties of the crust matter [204–206].

Since its prediction, significant progress has been made in simulating the pasta phases [207–209]. In this section, we use the hydrodynamics model to simulate the pasta phases at average baryon densities $0.045 \leqslant n \leqslant 0.07\,\mathrm{fm}^{-3}$. In the nuclear-pasta system, the chemical potentials of baryons and electrons satisfy the β-equilibrium condition

$$\mu_n = \mu_p + \mu_e, \tag{31}$$

where μ_q is the chemical potential of species $q = n,p,e$ for neutrons, protons, and electrons, respectively, and $\Delta m =$

$m_n - m_p$ is the neutron-proton mass difference. The total energy is the sum of the baryon energy $E_{\rm baryon}$, the electron density $E_{\rm elec}$, and the proton-neutron mass difference

$$E_{\rm pasta} = E_{\rm baryon} + E_{\rm elec} - \Delta mc^2 Z. \quad (32)$$

For the baryon energy, we use the hydrodynamics model defined in Appendix B with the SeaLL1 parametrization. The electron energy is the Thomas-Fermi energy for relativistic electrons

$$E_{\rm elec} = \int d^3\boldsymbol{r}\ (3\pi^2 n_e)^{4/3} \frac{\hbar c}{4\pi^2}, \quad (33)$$

where the electron density is determined from Eq. (32) as

$$n_e(\boldsymbol{r}) = \Theta(\mu_n - \mu_p + V_c(\boldsymbol{r}) + \Delta mc^2) \times \frac{1}{3\pi^2}\left[\frac{\mu_n - \mu_p + V_c(\boldsymbol{r}) + \Delta mc^2}{\hbar c}\right]^3. \quad (34)$$

where $V_c(\boldsymbol{r})$ is the Coulomb potential experienced by electrons, which includes both the direct and the relativistic exchange parts [2] (notice the positive sign, opposite from the nonrelativistic Slater approximation)

$$V_c(\boldsymbol{r}) = e^2 \int d^3\boldsymbol{r}'\ \frac{n_c(\boldsymbol{r}')}{|\boldsymbol{r} - \boldsymbol{r}'|} + \frac{1}{2}e^2\left[\frac{3}{\pi} n_e(\boldsymbol{r})\right]^{1/3}, \quad (35)$$

where $n_c(\boldsymbol{r}) = n_p(\boldsymbol{r}) - n_e(\boldsymbol{r})$ is the charge density. Through solving the hydrodynamics equation similar to Eq. (A6a) for baryons and Eq. (34) for electrons, the charge number $Z = \int d^3\boldsymbol{r}\ n_e(\boldsymbol{r})$ is determined self-consistently for a given baryon number $A = N_n + N_p$, where $N_p = Z$ is satisfied for charge neutrality. Numerically, we perform this calculation in a three-dimensional (3D) cubic lattice with periodic boundary conditions at average baryon densities $n =$ 0.045,0.05,0.055,0.06,0.065, and 0.07 fm^{-3}To explore the role of finite-size effects, the size of cubic lattice is chosen as $L_x = 32,48,64$, and 96 fm respectively for all ns. The lattice constant is fixed as $dx = 1.00$ fm. In Fig. 17, we compare the energy of uniform pure neutron matter, with uniform matter in β-equilibrium, and allowing for the formation of inhomogeneities. Even though for various size cubic boxes the spatial distribution of the matter at a given average density is not identical, the gain in energy and the proton/neutron ratios are practically the same and at an average density slightly above 0.07 fm^{-3} the matter distribution becomes homogeneous.

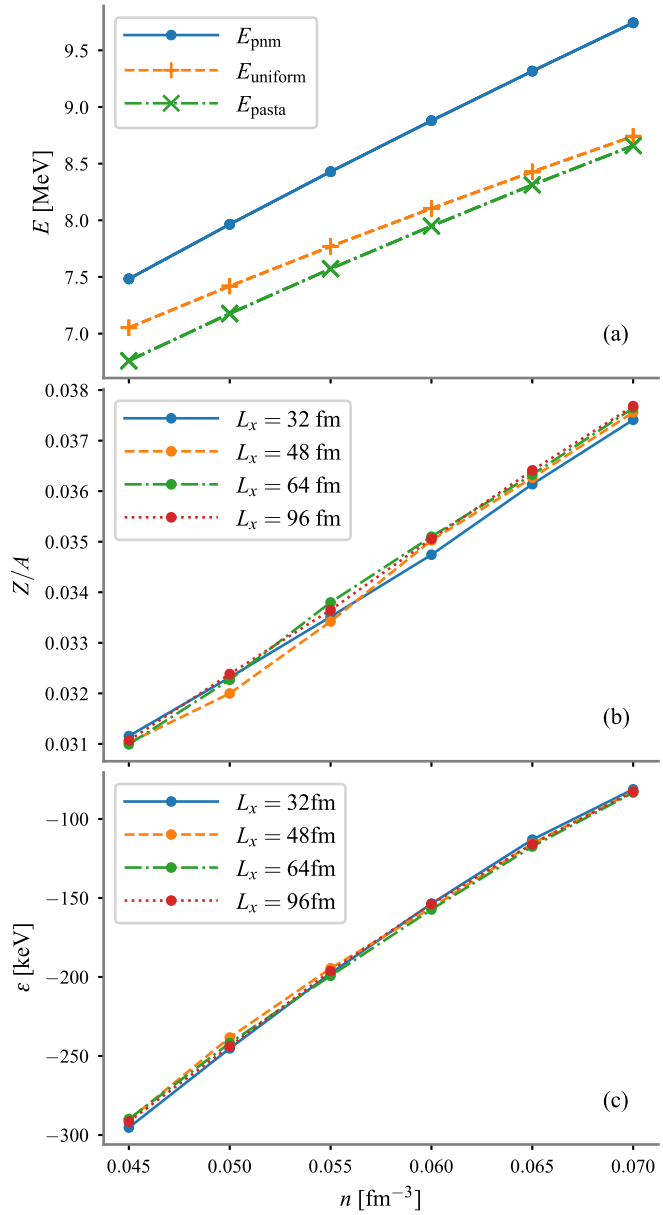

FIG. 17. (a) Energy per baryon in the pasta phase ($E_{\rm past}$), energy per neutron in pure neutron matter ($E_{\rm pnm}$), and energy per baryon in uniform nuclear matter ($E_{\rm uni}$) as a function of average baryon density. (b) Charge ratio of the nuclear pasta as a function of average baryon density. (c) The energy per nucleon difference between the uniform and the inhomogeneous matter configurations in β equilibrium as a function of the average baryon density.

H. Comparison with other NEDFs

The accuracy of the ground-state nuclear properties obtained using SeaLL1 NEDF compares extremely well with other approaches. The UNEDF1 nuclear energy functional introduced by Kortelainen *et al.* [74] has a residual of $\chi_E = 1.91$ MeV per nucleus for 555 even-even nuclei from AME2013 [210] and an rms of 0.75 MeV (for S_{2n}) and 0.79 MeV (for S_{2p}) compared to $\chi_E = 1.74$ MeV, and rms 0.69 MeV (for S_{2n}), and 0.59 MeV (for S_{2p}) in the case of SeaLL1. SeaLL1 delivers better quality single-particle spectra as well, without introducing them into the fit, unlike UNEDF2. UNEDF2 reports an rms $\chi_r = 0.018$ fm for 49 nuclei only, and we cannot compare that with that obtained by us, a $\chi_r =$ 0.034 fm for 345 measured even-even nuclei. The UNEDF2 functional of Kortelainen et al. [75] depends on 14 strongly correlated parameters.

The BCPM energy density functional introduced by Baldo *et al.* [211,212] is based on information extracted from Brueckner-Hartree-Fock calculations of neutron and symmetric nuclear matter [213], and four additional parameters to describe pairing correlations in the $T = 1$ channel [214], one for the spin-orbit interaction and two for the surface properties, in total seven parameters, not counting the fine-tuning of

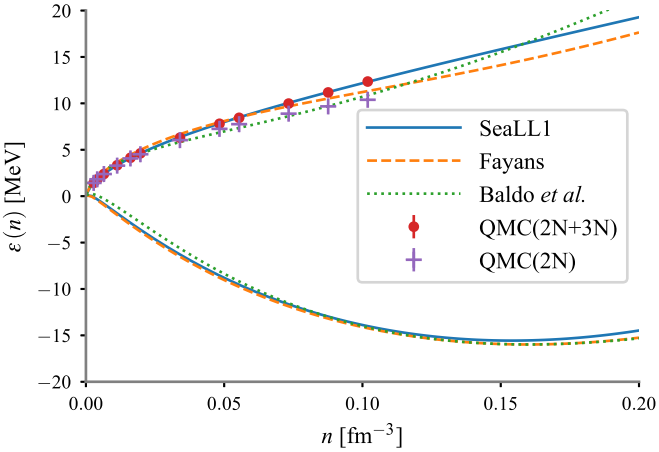

FIG. 18. The energy per nucleon for pure neutron matter and symmetric neutron matter used in SeaLL1, compared to the corresponding energies used by Fayans [143] and Baldo *et al.* [211–213]. For comparison, we have shown with a dashed line the results of the QMC calculation of Wlazłowski *et al.* [131], with $2N$ and $3N$ interactions as well the result with the $2N$ interactions alone.

nuclear saturation properties. This approach is similar in spirit to the one suggested by Fayans [143,215], in the spirit of the Kohh-Sham DFT [10]. These authors have also included the beyond-mean-field rotational energy correction [216], and the center-of-mass energy correction [217], and they find a $\chi_E = 1.58$ MeV for 579 even-even nuclei in AME2003 [210] and a $\chi_r = 0.027$ fm for 313 nuclei.

Goriely *et al.* [7,8,69,71] have produced over the years a series of high-accuracy mass models based on Skyrme NEDFs. Their best model gives an average rms around 0.5 MeV for the entire mass table, and a very close value $\chi_E = 0.549$ MeV for even-even nuclei. In the case of BSk24 [71], the charge radius rms is $\chi_r = 0.005$ fm. However, in contrast with the UNEDF and SeaLL1 NEDF, the mass tables evaluated by Goriely *et al.* were obtained by adding various phenomenological corrections in order to account effectively for beyond-mean-field effects. These include corrections for the center-of-mass motion, the rotational energy correction, and the Wigner energy. These beyond-mean-field corrections are hard still to incorporate in dynamical calculations, as in the case of fission [117] or nucleus-nucleus collisions.

As an exercise, we performed a refit of SeaLL1 after including the phenomenological center-of-mass correction due to Butler *et al.* [217]. For spherical even-even nuclei, this term alone reduces the energy rms from 1.54 to 0.97 MeV. It is thus expected that by adding further beyond-mean-field corrections to SeaLL the value of χ_E can be reduced significantly.

We also mention work with the relativistic mean-field theory (RMFT) of nuclei. State-of-the-art parametrizations of the relativistic NEDF yields a χ_E between 2 and 3 MeV for even nuclei using the AME2012 data set [218,219].

Finally, we note that phenomenological Skyrme-like NEDFs "predict an inert point" of the neutron matter EoS at $n \approx 0.12\,\mathrm{fm}^{-3}$, with an energy per particle [71,220,221] noticeably lower than the QMC calculations and unrealistic low-density behavior; see Eq. (15a) and Fig. 18. The BCPM NEDF assumes that no quartic terms in isospin β^4 are present in the NEDF, as their EoS for neutron matter is softer than the EoS determined in QMC calculations of [131]; see discussion in Appendix D. Adding the quartic β^4 ($j = 2$) terms does not significantly impact the quality of the fits; see Sec. III C. However, the best-fit functional with only quadratic β^2 ($j = 1$) terms does not reproduce the neutron matter EoS, especially near $n \approx 0.12\,\mathrm{fm}^{-3}$ and the low-density behavior. These results demonstrate two important points: (1) quartic terms $\propto \beta^4$ ($j = 2$) appear to be needed to reproduce the accurate neutron matter EoS only and (2) known nuclear masses do not constrain these quartic terms.

V. PERSPECTIVES

A. Static properties and correlation energies

Additional control may be obtained by introducing generalizations of the terms included in SeaLL1. These may be used to refine other nuclear properties, including the static electric dipole polarizability, nucleon effective masses, single-particle spectra, proton and neutron pairing gaps, fission barriers, and the second fission isomer energies. For example,

$$\mathcal{E}_{\nabla n} = \eta_0 \frac{\hbar^2}{2m}|\nabla n_n + \nabla n_p|^2 + \eta_1 \frac{\hbar^2}{2m}|\nabla n_n - \nabla n_p|^2 \quad (36)$$

with $\eta_0 \neq \eta_1$ would allow one to adjust the neutron skin thickness somewhat independently from the symmetry properties of the functional and one can also control the static electric polarizability in the same manner.

The single-particle spectra for ^{48}Ca and ^{208}Pb obtained with SealLL1 have a larger neutron gaps and smaller proton gaps than measured experimentally (see Fig. 13). This could be remedied by tuning independently the parameters $W_0 \neq W_1$ in a more general form of the spin-orbit coupling,

$$\mathcal{E}_{\mathrm{SO}} = W_0 \boldsymbol{J} \cdot \nabla n + W_1(\boldsymbol{J}_n - \boldsymbol{J}_p) \cdot (\nabla n_n - \nabla n_p), \quad (37)$$

which could be used to independently fine-tune proton and neutron single-particle spectra near the Fermi level. One can add as well a density dependence of the spin-orbit coupling, which can lead to fine changes of the single-particle spectra; see also Ref. [8] for a related study.

One could further tune the single-particle spectra, and adjust the nucleon effective masses, by introducing more generalized density-dependent terms of the type arising in Eqs. (17a),

$$\mathcal{E}_\tau \propto \tau n^\sigma - \boldsymbol{j}^2 n^{\sigma-1} - \frac{3}{5}(3\pi^2)^{2/3} n^{5/3+\sigma} \propto \frac{|\nabla n|^2}{n^{1-\sigma}}. \quad (38)$$

(The obvious isospin structure has been suppressed.) The presence of the current density here is required in order to restore Galilean covariance [120]. Since the density gradients are peaked at the nuclear surface, the dependence of these coupling constants on density are not expected to lead to a significant changes in the quality of nuclear mass fits. The corresponding coupling constants would thus play a subdominant role as discussed in Sec. III G. This shows that terms like τn^σ in Skyrme-like functionals can be used in the combination (38), where they would play a subdominant role in mass fits.

In connection with gradient corrections, a remark is in order. Since the density gradients peak at the surface, allowing the corresponding coupling constants to acquire a density dependence could be useful, but such a density dependence of these coupling constants likely is not going to be very sensitive to different powers of the density or even a linear combination of different powers of the densities, though it might be capable of discriminating between various isospin structures. This behavior was observed, for example, by Goriely [7], when they introduced various density dependence of the spin-orbit terms and observed that the energy rms changed only by 20 keV.

Similarly, a long-standing feature of standard nuclear energy density functionals (NEDFs) requires breaking the isospin symmetry of the pairing contribution, even needing stronger proton pairing than neutron pairing [74,75,147] despite the Coulomb repulsion. This can easily be remedied by using instead a modified form of pairing which conserves the charge symmetry:

$$\mathcal{E}_\Delta = \int d^3\boldsymbol{r}\; g_{\rm eff}(\boldsymbol{r})(|\nu_n(\boldsymbol{r})|^2 + |\nu_p(\boldsymbol{r})|^2) + \int d^3\boldsymbol{r}\; h_{\rm eff}(\boldsymbol{r})(|\nu_n(\boldsymbol{r})|^2 - |\nu_p(\boldsymbol{r})|^2)\beta, \quad (39a)$$

where $\beta = (n_n - n_p)/(n_n + n_p)$. The dependence on neutron and proton densities of the bare coupling constants should satisfy isospin symmetry:

$$g(n_n(\boldsymbol{r}),n_p(\boldsymbol{r})) = g(n_p(\boldsymbol{r}),n_n(\boldsymbol{r})), \quad (39b)$$

$$h(n_n(\boldsymbol{r}),n_p(\boldsymbol{r})) = h(n_p(\boldsymbol{r}),n_n(\boldsymbol{r})). \quad (39c)$$

Since in measured nuclei one has predominantly $N \geqslant Z$, see Fig. 16, a phenomenological analysis that leads to a larger apparent coupling for protons than for neutrons can be reconciled with renormalized coupling constants $g_{\rm eff}(\boldsymbol{r}) < 0$ and $h_{\rm eff}(\boldsymbol{r}) > 0$.

An additional subdominant term of the type

$$\tilde{\mathcal{E}}_{\rm spin} = \alpha_1\left(\boldsymbol{s}_n^2 + \boldsymbol{s}_p^2\right) + \alpha_2 \boldsymbol{s}_n \cdot \boldsymbol{s}_p \quad (40)$$

should be considered as well for odd nuclei. The contribution of spin densities is typically much smaller than the contributions of the densities in nuclei, $\int d^3\boldsymbol{r}\; n_{n,p}(\boldsymbol{r}) \gg |\int d^3\boldsymbol{r}\; \boldsymbol{s}_{n,p}(\boldsymbol{r})|$, as in even-even nuclei $\boldsymbol{s}_{n,p}(\boldsymbol{r}) \equiv 0$, and thus these terms will play a noticeable role in odd-A and odd-N–odd-Z nuclei mainly [222]. The term proportional to α_2 will be important mostly in odd-odd nuclei. These type of contributions will affect in particular β-decay matrix elements.

The structure of the double-humped fission barriers also depends critically on the character of shell corrections (see Fig. 15), and is thus sensitive to the single-particle spectrum structure. Hence, fission properties may be tuned by adjusting all of the subdominant terms discussed above without degrading the ability of the functional to fit masses and charge radii.

We now have a clear path to refine the structure of the SeaLL1 NEDF, by systematically adding physically motivated parameters in order to better describe nuclear physics observables. While the properties of the simple SeaLL1 functional as presented here are quite reasonable without any fine-tuning, there is room for substantial improvement. For example, one can consider spin-orbit terms (37) with $W_0 \neq W_1$, gradient terms (36) with $\eta_0 \neq \eta_1$, gradient terms modifying the nucleon effective masses (38), and density-dependent pairing terms (39a) with both couplings $g_{\rm eff}$ and $h_{\rm eff}$ nonvanishing. Subdominant corrections can be made to the symmetry energy (30) with $a_1 - b_1 n_0^{1/3} \neq 0$ and $c_1 \neq 0$. Even the incompressibility $K_0 = \frac{6}{5}\varepsilon_F - 12\varepsilon_0 + 2a_0 n_0^{2/3}$ (if ε_0 and n_0 are fixed) can be changed by $\approx \pm 20$ MeV with the parameter a_0; see Eq. (27c) and Fig. 7.

The next step is to account for correlation energies; the center-of-mass corrections, which, in the case of self-bound systems, present some challenges [223–230]. Accounting for the center-of-mass correction [217,231], the correction due to particle number projection [232], the vibration correlation energy correction [6,233], the angular momentum projection [6,70,173,216,220,234,235], and Wigner energy [7,8] should reduce the rms energy from about 1.7 to about 0.5 MeV. Further improvement may require a proper accounting for quantum chaoslike effects [78–86].

B. Nuclear dynamics and time-dependent DFT

One of the main advantages of DFT is the ability to also describe nuclear dynamics with the same NEDF as for static properties. In time-dependent phenomena, additional terms of the NEDF become active. We could especially consider two types of entrainment terms. Such terms are never discussed in any standard theory of large amplitude collective motion in nuclear physics [64,236,237], despite being allowed by symmetry. They are as natural to consider in the presence of mixed proton and neutron superfluids in neutron stars as they are in mixtures of ^{3}He and ^{4}He superfluids [238–240].

Entrainment (the Andreev-Bashkin effect) was predicted by Andreev and Bashkin [238] to occur in superfluid mixtures of ^{3}He and ^{4}He and is rather surprising at first sight, since superfluids are expected to flow without resistance. In particular, one might have expected that if somehow one would bring into motion only one superfluid component, superfluidity will have the consequence that the other component remains at rest. The entrainment term (41) is indeed dissipationless, and thus it does not violate superfluidity but allows the motion of one superfluid to influence (entrain) the other. It is natural to expect a similar phenomenon to arise in nuclei, where proton and neutron (super)fluids can coexist. The entrainment term is Galilean invariant and in nuclear systems has the form

$$\mathcal{E}_{\rm entrain} = g_{\rm ent}\left(\frac{n_n n_p}{n^2}\right)\frac{n}{2m}\left|\frac{\boldsymbol{j}_n}{n_n} - \frac{\boldsymbol{j}_p}{n_p}\right|^2, \quad (41)$$

where $\boldsymbol{j}_{n,p}$ are the density currents (10f). Since this type of coupling between neutron and proton fluids is absent when either density vanishes, we require that $g_{\rm ent}(0) = 0$. The requirement that the total kinetic energy is always positive leads to the condition $x + g_{\rm ent}(x) > 0$. Entrainment should also plays a role in neutron stars and has been studied intermittently since 1975 [239–247]. The significant effect of this term is seen in the dynamics only, when the motion of one fluid will

drag along the other and therefore the presence of such an additional term will affect strongly the excitation energies of isovector modes such as the giant dipole resonances (GDRs) and the Thomas-Reiche-Kuhn sum rule. The simplest choice for this coupling is $g_{\rm ent}(x) = \alpha x$ with $1 + \alpha > 0$, which allows for negative values of $g(x)$. Borumand *et al.* [242] recommend $g_{\rm ent}(x) \propto x^{2/3}$, which would restrict $g(x) \geqslant 0$ for small values of x.

A second type of entrainment contribution can be introduced as well, with which one can control the Gamow-Teller transitions and β-transition matrix elements.

$$\tilde{\mathcal{E}}_{\rm spin\ entrain} = \tilde{g}_{\rm ent}\left(\frac{n_n n_p}{n^2}\right)\frac{n}{2m}\left|\frac{\boldsymbol{J}_n}{n_n} - \frac{\boldsymbol{J}_p}{n_p}\right|^2, \tag{42}$$

where $\boldsymbol{J}_{n,p}$ are the spin-density currents (10d).

VI. CONCLUSIONS

The nuclear energy density functional (NEDF) presented here is physically intuitive and provides a clear strategy for further improving the quality of mass fits by separating contributions of various energy scales in the χ_E of nuclear masses. In this respect, the approach outlined here, and ideas used before by Bertsch *et al.* [153], is similar in spirit to an effective field theory. Our starting point was a generalization of the liquid drop model as suggested by Weizsäcker [11], which aligns with the Hohenberg and Kohn [1] formulation of DFT in terms of neutron and proton densities only. This formulation allows us to evaluate proton and neutron densities, and thus the charge radii as well, and the binding energies of 2375 nuclei with an accuracy superior to the Bethe-Weizsäcker mass formula, but with the same number of parameters. Using this as a starting point, three additional parameters were identified to produce a minimal NEDF, in the spirit of the Kohn-Sham LDA formulation [10] of the DFT, which is extended to account for the presence of pairing correlations, shell effects, and the density dependence of the symmetry energy. The NEDF developed in this work, which we call SeaLL1, contains thus seven significant parameters, each clearly related to specific properties of nuclei.

The SeaLL1 NEDF describes the nuclear masses of 606 even-nuclei from the AME2012 evaluation [18,19] with a mean energy error of 0.93 MeV and a standard deviation 1.46 MeV, two-neutron and two-proton separation energies with rms errors of 0.69 and 0.59 MeV respectively, and the charge radii of 345 even-even nuclei [118] with a mean of 0.022 fm and a standard deviation of 0.025 fm.

Since in SeaLL1 the effective nucleon mass is equal to the bare mass, one can naturally expect that nuclear level densities [248] will be described rather accurately, along with the single-particle spectra around the Fermi level, unlike many phenomenological NEDFs. The quality of the single-particle spectra are typically better than in the case of previous NEDFs, even though we did not include them in the fit.

Nuclear and neutron matter properties are also well reproduced in SeaLL1. One needs only two parameters to reproduce the symmetric nuclear binding energy and saturation density. We find a reasonable value for the isoscalar nuclear incompressibility, $K_0 = 230$ MeV, although the saturation density is a bit lower than the canonical value 0.16 fm^{-3}. The saturation density is not well constrained by the mass fits alone but can be constrained by also considering the charge radii as discussed in Fig. 5. Two additional parameters control the symmetry properties of nuclear matter. The symmetry energy $S = 31.7$ MeV, its density dependence, the neutron skin thickness 0.131 fm of ^{208}Pb, and the compressibility of nuclear matter all have reasonable values. SeaLL1 also incorporates information about the EoS of pure neutron matter from quantum Monte Carlo calculations with chiral effective field theory *NN* interactions at N3LO level and *NNN* interactions at the N2LO level. The addition of quartic isovector terms $\propto \beta^4$ permit the NEDF to match the neutron matter EoS without significantly affecting the global mass fit. We thus find that nuclear masses and the neutron matter EoS are largely uncorrelated, a conclusion somewhat at odds with previous analyses.

A gradient term with a single parameter controls the diffuseness of the nuclear surface and the nuclear surface tension. Two additional parameters are required to describe the spin-orbit interaction and the pairing correlations.

We have identified the respective role of the parameters of the SeaLL1 NEDF by using a principal component analysis. We have established that a number of parameters play an insignificant role in the mass fit. Their values can be varied significantly without affecting the quality of the χ_E. We refer to these as insignificant or subdominant parameters, and identify how they can be used to fine-tune the values of other observables.

Looking ahead, we note that a number of important nuclear observables such as the position of the GDR, the Gamow-Teller resonances, the Thomas-Kuhn-Reiche sum rule, the nuclear compressibility and correspondingly the position of the giant monopole resonances, the dipole electric polarizability, the neutron skin thickness, and the density dependence of the symmetry energy depend on parameters which can be either freely adjusted (spin-orbit splittings and/or effective masses) without affecting the accuracy of the ground-state binding energies, or which affect very little the ground-state properties. In this respect, SeaLL1 stands apart from previous NEDFs, in which many of these properties were often included in the fits.

ACKNOWLEDGMENTS

We are grateful to George F. Bertsch for numerous discussions and suggestions, to Rebecca Surman, Gabriel Martinez-Pinedo, and Meng-Ru Wu for providing the data for the *r*-process trajectories, and to Jeremy W. Holt, David B. Kaplan, Jérôme Margueron, Piotr Magierski, and Sanjay Reddy for comments. This work was supported in part by US DOE Grant No. DE-FG02-97ER-41014, a WSU Seed Grant, and the Scientific Discovery through Advanced Computing (SciDAC) program funded by US Department of Energy, Office of Science, Advanced Scientific Computing Research and Nuclear Physics. It was partly performed under the auspices of the US Department of Energy by the Lawrence Livermore National Laboratory under Contract No. DE-AC52-07NA27344. Some calculations reported here have been performed at the University of Washington Hyak cluster funded by the NSF MRI Grant No. PHY-0922770, and with computing support

from the Lawrence Livermore National Laboratory (LLNL) Institutional Computing Grand Challenge program.

APPENDIX A: ORBITAL-FREE FUNCTIONAL

Here we discuss some details of the orbital-free theory described in Sec. III H.

As mentioned there, the main challenge in formulating an orbital-free theory is to express terms with the auxiliary densities $\tau_{n,p}$, ν, $\boldsymbol{J}_{n,p}$, and $\boldsymbol{j}_{n,p}$ by an appropriate functional of the number densities $n_{n,p}$. One approach is to start with a semiclassical expansion. Neglecting the spin-orbit interaction (20), the kinetic density τ admits the following semiclassical expansion [2,31,151]:

$$\tau \approx \overbrace{\tfrac{3}{5}(3\pi^2)^{2/3}n^{5/3}}^{\tau_{\rm TF}[n]} + \overbrace{\frac{1}{9}|\nabla\sqrt{n}|^2}^{\tau_2[n]} + \tau_4[n] + \cdots . \tag{A1}$$

The factor of $1/9$ can be derived rigorously for smoothly varying densities, along with higher order terms discussed in Eq. (A4) below. This should be compared with the factor of unity originally suggested by Weizsäcker [11], later shown to be valid only if the density has small-amplitude rapid oscillations [2,31,151]. For nuclei, the semiclassical result is relevant for the bulk but gives incorrect asymptotic behavior, while Weizsäcker's result reproduces the correct asymptotic behavior but is a poor approximation in the bulk; see Ref. [57] for a discussion. Resolving this tension is an active area of research in DFT, and many suggestions have been compared [249].

The simplest option is to treat the coefficient $1/9 = \eta$ as a phenomenological parameter, since gradient terms can also be generated by interactions [250–252]. Fitting the nuclear masses yields values of η close to 0.5, roughly halfway between the semiclassical and Weizsäcker values. Stocker *et al.* [253] used a similar approach in order to discuss the anomaly in the nuclear curvature energy—the term in the nuclear mass formula $\propto A^{1/3}$.

Another appealing approach suggested by DePristo and Kress [152] and advocated in Ref. [2] is to use a Padé approximant $F(X)$ to interpolate between the semiclassical and asymptotic results:

$$\tau \approx \tau_{\rm TF}[n]F(X), \quad X = \frac{\tau_2[n]}{\tau_{\rm TF}[n]}. \tag{A2}$$

DePristo and Kress [152] motivate a rather complicated form $F(X)$, but for nuclei we find little improvement over the following single-parameter form:

$$F(X) = \frac{1+(1+\kappa)+9\kappa X^2}{1+\kappa X} = \begin{cases} 1+X & X \ll 1, \\ 9X & X \gg 1. \end{cases} \tag{A3}$$

Note: The approximation $\eta \approx 1/9$ mentioned above is implemented with $F(X) = 1 + 9\eta X$.

The next order in the semiclassical expansion of noninteracting fermions [2,31] is

$$\tau_4[n] = \frac{1}{810(3\pi^2)^{2/3}} f(n),$$
$$f(n) = n^{1/3}\left[\left(\frac{\nabla n}{n}\right)^4 - \frac{27}{8}\left(\frac{\nabla n}{n}\right)^2\frac{\nabla^2 n}{n} + 3\left(\frac{\nabla^2 n}{n}\right)^2\right]. \tag{A4}$$

This type of correction has been studied in nuclear physics and shown to lead to quite accurate estimates of the kinetic energy density within the extended Thomas-Fermi approximation [31,57,254]. Within a DFT, such terms can also arise due to the finite range of the interactions in a matter similar to some Skyrme interactions [250–252]. However, these terms—even with adjustable parameters—do not significantly change the quality of the mass fits, so we do not consider them in our main analysis. Including them perturbatively in the fit, however, does improve the fit of the charge radii. For example, fitting the overall coefficient reduces the charge radii residual χ_r (see details in Appendix B) from $\chi_r \approx 0.14$ fm to $\chi_r \approx 0.09$ fm. Fitting each of the three terms independently further reduces the residuals to $\chi_r \approx 0.06$ fm. Fourth-order terms are neglected as they can lead to a complex behavior of the emerging equation for the densities, which can be difficult to rationalize. (See, for example, the analysis of fourth-order differential equations arising in case of nonlocal potentials by Bulgac [255].) Higher order gradient corrections than Eq. (A4) lead to an unphysical behavior of the densities in the classically forbidden regions. Furthermore, the semiclassical expansion has an asymptotic character [151], and corrections beyond second order do not always improve the functional. Finally, when using a properly fit Padé approximant Eq. (23b), we find that $\int \tau_{\rm TF}[n]F(X) - \tau_{\rm TF}[n] - \tau_2[n]d^3\boldsymbol{x} \approx \int \tau_4[n]d^3\boldsymbol{x}$ for many nuclei. Thus, the Padé approximant Eq. (23b) seems to incorporate the qualitative effects of the $\tau_4[n]$ term. For these reasons, we do not include fourth-order corrections $\tau_4[n]$ in our orbital-free theory.

When spin-orbit interactions are included, they modify the semiclassical expansion. Thus, to properly express the orbital-free theory, we must consider both terms together. The correct semiclassical expansion of this combined energy density to second order is [57,254]

$$\begin{aligned}\mathcal{E}_{\rm kin} + \mathcal{E}_{\rm SO} &= \frac{\hbar^2}{2m}(\tau_n + \tau_p) + W_0\boldsymbol{J}\cdot\boldsymbol{\nabla}n \\ &\approx \frac{\hbar^2}{2m}(\tau_{\rm TF}[n_n] + \tau_{\rm TF}[n_p] + \tau_2[n_n] + \tau_2[n_p]) \\ &\quad - \frac{W_0^2}{2}\frac{2m}{\hbar^2}n(\boldsymbol{\nabla}n)^2.\end{aligned} \tag{A5}$$

Note that the sign of the last term differs from the expression (7) in Ref. [254], which contains only the kinetic component. The result here combines both the kinetic and spin-orbit contributions, altering the sign. (The remaining terms in the

functional only alter the mean-field potential, and so they do not affect this result.)

This expansion suffers the same problems as the pure semiclassical expansion of the kinetic energy, Eq. (A1). Thus, for the reasons discussed above, we replace $\tau_{\rm TF}+\tau_2$ with the Padé approximant, Eq. (23b). In principle, a similar correction could be used with the spin-orbit term; however, this term has the form $n(\nabla n)^2$ instead of $\tau_2 \propto (\nabla n)^2/n$. It is therefore suppressed in the tails and does not effect the asymptotic behavior of the nuclear density profile. Note that the scaling is similar to the gradient correction. For this reason, we keep the semiclassical form but refit the coefficient η_s to compensate for any inaccuracies.

The equations that determine the equilibrium densities of a nucleus in the orbital-free theory are obtained by minimizing the energy of a given nucleus $E(N,Z)=\int d^3\boldsymbol{r}\ \mathcal{E}[n_n,n_p]$ with respect to the densities, while constraining the total numbers of neutrons N and protons Z with two chemical potentials $\mu_{n,p}$:

$$-\frac{\hbar^2}{2m}\nabla\left(\frac{F'(X_q)}{9}\nabla n_q^{1/2}\right)+U_q n_q^{1/2}=\mu_q n_q^{1/2}, \quad \text{(A6a)}$$

$$U_q=\frac{\partial\mathcal{E}[n_n,n_p]}{\partial n_q}, \quad \text{for } q\in\{n,p\}. \quad \text{(A6b)}$$

We present these here as the inclusion of $F(X)$ acts as a density-dependent effective mass. No such complication appears in the HFB formulation, which proceeds as described in [119].

APPENDIX B: ORBITAL-FREE NEDF PARAMETERS

We start by considering the functional with the simplified kinetic energy

$$\mathcal{E}_{\rm kin}[n_n,n_p]=\frac{\hbar^2}{2m}\sum_{q=n,p}\tau_{\rm TF}[n_q]F(X_q), \quad \text{(B1)}$$

where $\tau_{\rm TF}$, X_q, and $F(X)$ are given in Eqs. (A2) and (A3).

As discussed above, when using the simplified form $F(X)=1+9\eta X$, the best-fit value of $\eta\approx 0.5$. One might naïvely think that this corresponds to a dynamical theory of superfluid neutron and proton pairs with an effective nucleon pair mass $m_{\rm eff}\approx 2m$ (see, i.e., Ref. [256] and references therein). Such a theory with $\eta=0.5$, however, leaves the potentials U_q wrong by a factor of 2. To correctly describe a dynamical theory of superfluid neutron and proton pairs, one would need a value of $\eta=1/4$. Thus, in this approximation, the parameter η must simply be interpreted as an approximate way to control the falloff of the densities in the surface region where the interaction effects are still strong.

We now consider our NEDF as an hydrodynamic model for nuclei and fit the parameters to the same $N_E=2375$ measured nuclear masses with $A\geqslant 16$ from Refs. [18,19] used to fit the liquid drop models in Table I. However, unlike the liquid drop model, our hydrodynamic model allows us also to consider properties of the density distribution. Thus, we also fit the $N_r=883$ nuclear charge radii from Ref. [118] with $\chi_r^2=\sum|\delta r|^2/N_r$. When we include the charge radii in the fit, we minimize the following quantity $\chi_E^2/(3\,\text{MeV})^2+\chi_r^2/(0.05\,\text{fm})^2$ which roughly equalizes the weight of the mass and radii contributions in the fit.

At this point, we have seven parameters in our NEDF: η, $a_{0,1}$, $b_{0,1}$, and $c_{0,1}$ (the $j=2$ parameters are fixed by the neutron matter EoS). In addition, we include by hand the conventional even-odd staggering Eq. (2b) with a coefficient δ to describe pairing correlations, even though this has very little significance in the fits. The results of various fits scenarios we have considered are summarized below in Table IV where we present sets of parameters for various fit strategies, and in Table V where we present the saturation, symmetry, and neutron skin properties.

We have considered the following type of fits:

NEDF-0: A six parameter least-squares fit of the $N_E=2375$ nuclear masses [18,19] including η, b_0, c_0, a_1, b_1, and δ but setting the nucleon charge form factors Eq. (12c) $G_E^p\equiv 1$ and $G_E^n\equiv 0$.

NEDF-1: The same as NEDF-0, but including the measured charge form factors. Comparing it with NEDF-0 we see that the electric form factors are not significant for the overall mass fits but slightly impact the charge radii at the 0.01 fm level (for the reduced χ_r).

NEDF-2: The same as NEDF-1, but without the pairing parameter $\delta=0$. Comparing with it NEDF-1 we see that odd-event staggering is also relatively unconstrained at the level of 0.1 MeV per nucleus. This is consistent with the results from the mass formulas in Table I.

NEDF-1r: The same as NEDF-1, but including the $N_r=883$ charge radii into the fit. We see that there is significant room to improve the description of the charge radii without significantly degrading the mass fits.

NEDF-3 The same as NEDF-1, but with all eight parameters, including a_0 and c_1 that we omitted from the previous fits. In conjunction with the principal component analysis shown in Fig. 20, this fit demonstrates that the terms with parameters a_0 and c_1 are unconstrained.

NEDF-3n: The same as NEDF-1, but with all eight parameters, including a_0 and c_1 that we omitted from the previous fits, and the β^4 parameters for the terms quartic in isospin, constrained by the QMC neutron matter EoS [131] using Eqs. (15b). That the quality of the fit, isoscalar, and isovector parameters changes very little, which demonstrates that the neutron matter EoS is essentially independent of the nuclear masses.

NEDF-3nr: The same as NEDF-3n but including the charge radii as in fit NEDF-1r. That the a_0 and c_1 terms are unconstrained for both masses and radii is also emphasized by this fit.

NEDF-E: Following the principal component analysis of NEDF-3n (discussed below), we find the combination $a_1-b_1n_0^{1/3}$ to be only weakly constrained by the mass fit. To test this, we set $a_1=b_1n_0^{1/3}$ where $n_0=0.154\,\text{fm}^{-3}$ is a constant. The combination $a_1-b_1n_0^{1/3}$, to which the masses are insensitive, allows independent control the slope L_2 of the symmetry energy [see Eq. (27e)]. From the fits, we see that this same combination also controls the neutron skin thicknesses.

TABLE IV. Fit parameters and residuals for the various NEDFs. The top set of functionals uses the simplified form $F(X) = 1 + 9\eta X$ while the second set uses the form in Eq. (A3) with the parameter κ instead. The SeaLL1 parameters are shown in the last row for comparison.

NEDF	η	η_s [fm^3]	W_0 [MeV.fm^5]	a_0 [MeV.fm^2]	a_1 [MeV.fm^2]	a_2 [MeV.fm^2]	b_0 [MeV.fm^3]	b_1 [MeV.fm^3]	b_2 [MeV.fm^3]	c_0 [MeV.fm^4]	c_1 [MeV.fm^4]	c_2 [MeV.fm^4]	δ [MeV]	χ_E [MeV]	χ_r [fm]
0	0.4719	0	0	0	131.1	0	−741.570	−143	0	940.50	0	0	11.46	2.59	0.14
1	0.4742	0	0	0	122.6	0	−738.302	−128	0	934.38	0	0	11.47	2.58	0.13
2	0.4743	0	0	0	120.1	0	−740.226	−123	0	938.26	0	0	0	2.71	0.14
1r	0.4807	0	0	0	135.9	0	−702.003	−157	0	861.33	0	0	11.75	2.71	0.05
3	0.4800	0	0	−10	125.0	0	−695.08	−130	0	892.1	−0.0	0	11.41	2.58	0.14
3n	0.4739	0	0	−7.59	195.7	−220.7	−707.006	−322	913.194	902.50	100	−873.8	11.57	2.57	0.13
3nr	0.4815	0	0	−7.63	195.4	−220.4	−674.608	−317	876.220	837.29	75	−803.21	12.45	2.67	0.05
E	0.4885	0	0	0	34.60	0	−740.950	65.1	0	938.63	0	0	11.21	2.64	0.13
Er	0.4957	0	0	0	32.98	0	−707.394	62.1	0	870.91	0	0	12.71	2.74	0.05
En	0.4866	0	0	0	34.01	−66.60	−741.546	64.0	562.093	940.02	0	−830.90	11.26	2.62	0.13
Enr	0.4970	0	0	0	32.54	−65.13	−707.031	61.2	530.344	870.15	0	−761.03	12.51	2.74	0.05
En-rho	1/9	4.9731	0	0	29.71	−62.29	−672.625	55.9	501.277	934.85	0	−825.73	11.78	2.64	0.05
Enr-rho	1/9	5.0397	0	0	29.52	−62.11	−672.986	55.6	501.986	934.85	0	−825.73	13.72	2.68	0.05
En-so	1/9	5.4751	76.20	0	136.8	−169.4	−669.776	51.5	502.814	934.85	0	−825.73	11.73	3.18	0.05
		κ													
En-pade-1	0.07	5.0941	0	0	30.14	−62.73	−672.785	56.7	500.620	802.20	0	−693.08	10.40	2.82	0.07
En-pade-2	0.15	4.6365	0	0	30.37	−62.96	−672.213	57.2	499.610	801.41	0	−692.29	11.49	2.89	0.07
En-pade-3	0.20	4.4318	0	0	30.33	−62.91	−671.889	57.1	499.374	800.97	0	−691.85	11.94	2.93	0.07
En-pade-4	0.30	4.2098	0	0	31.50	−64.09	−672.625	59.3	497.894	801.98	0	−692.86	12.07	3.11	0.07
Hydro	0.20	3.3696	0	0	50.88	−83.47	−685.597	94.9	475.237	828.76	−160	−559.64	0	2.86	0.04
													g_0 [MeV fm^3]		
SeaLL1	N/A	3.93	73.50	0	64.30	−96.80	−684.50	119.90	449.20	827.26	−256	−461.70	−200	1.74	0.03

TABLE V. Saturation, symmetry, and neutron skin properties for the various NEDFs. All values in MeV unless otherwise specified.

NEDF	n_0 [fm^{-3}]	$-\varepsilon_0$	K	S	L	L_2	Neutron skin ^{208}Pb [fm]	Neutron skin ^{48}Ca [fm]
0	0.136	15.24	222.5	26.8	34.1	32.8	0.082	0.118
1	0.136	15.22	222.4	26.7	35.9	34.7	0.087	0.123
2	0.136	15.21	222.2	26.7	36.8	35.6	0.089	0.125
1r	0.148	15.48	227.7	27.1	30.9	29.6	0.078	0.116
3	0.136	15.21	216.5	26.7	34.7	33.4	0.088	0.124
3n	0.137	15.20	218.2	30.0	29.3	16.7	0.068	0.107
3nr	0.147	15.44	222.9	31.0	31.2	15.5	0.068	0.107
E	0.136	15.28	223.1	29.7	68.2	66.9	0.159	0.174
Er	0.147	15.53	228.1	30.6	70.2	68.9	0.161	0.176
En	0.136	15.27	222.9	30.1	29.1	66.1	0.152	0.172
Enr	0.147	15.53	228.2	31.1	31.1	68.3	0.156	0.174
En-rho	0.160	15.85	234.4	32.3	33.5	68.9	0.138	0.149
Enr-rho	0.160	15.87	234.6	32.4	33.5	68.6	0.138	0.149
En-so	0.160	15.74	233.1	32.2	33.5	65.4	0.120	0.139
En-pade-1	0.160	15.86	234.5	32.4	33.5	69.6	0.157	0.176
En-pade-2	0.160	15.83	234.2	32.3	33.5	69.9	0.166	0.189
En-pade-3	0.160	15.82	234.1	32.3	33.5	69.8	0.170	0.194
En-pade-4	0.160	15.85	234.4	32.3	33.5	71.6	0.181	0.206

NEDF-Er: The same as NEDF-E but including the charge radii as in fit NEDF-1r.
NEDF-En: This is our main fit. It is the same as NEDF-E but includes the β^4 parameters adjusted to reproduce the neutron matter EoS as in fit NEDF-3n.
NEDF-Enr: The same as NEDF-En but including the charge radii as in fit NEDF-1r.

In all fits above, the parameter η is around 1/2, which deviates from the Weiszäcker value 1/9. In our latest fits, we fix $\eta = 1/9$ and introduce a new gradient term η_s.

From the equilibrium condition of symmetric nuclear matter we get a relationship between $\tilde{a}_0$, $\tilde{b}_0$, and $\tilde{c}_0$,

$$0 = \tfrac{3}{5} + \tilde{a}_0 + \tfrac{3}{2}\tilde{b}_0 + 2\tilde{c}_0, \tag{B2}$$

or by using the original parameters,

$$a_0 = -\frac{3\varepsilon_F}{5k_0^2} - \frac{3}{2}b_0k_0 - 2c_0k_0^2, \tag{B3}$$

where $k_0 = n_0^{1/3}$, $n_0 = 0.16$. If a_0 is set to be 0, there is a relationship between b_0 and c_0:

$$c_0 = -\frac{3\varepsilon_F}{10k_0^4} - \frac{3b_0}{4k_0}. \tag{B4}$$

Using this relationship, the saturation density derived from the NEDF will be fixed to be $n_0 = 0.16$.

NEDF-En-rho: We fix $\eta = 1/9$ and add $\mathcal{E}_\nabla n$ into the NEDF. The saturation density n_0 is fixed to be 0.16 by adding a constraint between b_0 and c_0. Then the number of significant parameters in this NEDF is reduced to 3.
NEDF-Enr-rho: The same as NEDF-En-rho but including the charge radii as in fit NEDF-1r.

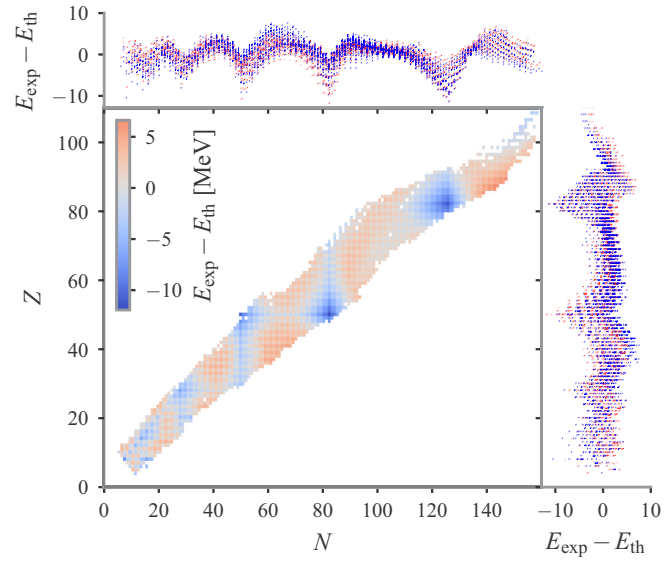

FIG. 19. The blue pluses show the results obtained using the orbital-free approximation with $\chi_E = 2.86$ MeV, while the red crosses are the results of the fits using nuclear mass formula Eq. (2), with $\chi_E = 2.64$ MeV. When compared against each other, the rms energy deviation between the two fits is $\Delta\chi_E = 1.10$ MeV. Thus, the orbital-free theory essentially reproduces the nuclear mass formula Eq. (2). The main plot is the same as in Fig. 1, in which one can see clearly the magic numbers separately for neutrons and protons.

In our earlier fits, we do not include the contribution of spin-orbit interaction, which is crucial for the proper description of nuclear static properties.

NEDF-En-so: Following NEDF-En-rho, we add $\mathcal{E}_{\rm SO}$ into the NEDF. The spin-orbit strength W_0 is fixed to be the value suggested in Ref. [143]. The significant fitting parameters are the same with NEDF-En-rho.

When we fix $\eta = 1/9$ and neglect higher order extended Thomas-Fermi (ETF) expansion in the kinetic energy, the asymptotic form of density can be proved to be

$$n(r) \underset{r\to\infty}{\longrightarrow} \frac{1}{r^2}e^{-r/a}, \quad a = \sqrt{-\frac{1}{36}\frac{\hbar^2}{2m}\frac{1}{\mu}}, \tag{B5}$$

where μ is the chemical potential (which is negative). Unfortunately, the diffuseness a is too small by a factor of 3 compared with the realistic nuclear surfaces, which corresponds to $\eta = 1$ in the asymptotic region. In order to obtain a nucleus density with correct asymptotic behavior, we suggest using the following Padé approximation in the representation of extended Thomas-Fermi approximation for the kinetic density; see Eqs. (A2) and (A3):

$$\tau_q = \tau_{TF,q}F(X), \tag{B6}$$

where the function $F(x)$ has the asymptotic behavior:

$$F(X) = \begin{cases} 1 + X, & X \ll 1 \\ 9X, & X \gg 1 \end{cases}. \tag{B7}$$

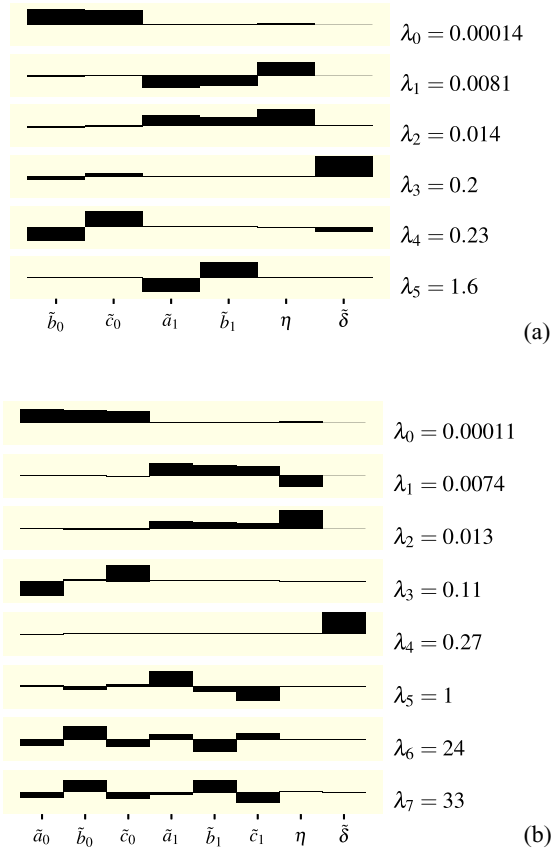

FIG. 20. Principal component analysis for the NEDF-1 fit (a) and the NEDF-3 fit (b). Plotted are the components of the eigenvectors $\boldsymbol{v}_n$ defining the principal component Eq. (25b) as linear combinations of the various dimensionless parameters. From this, we see that for NEDF1 the most significant component $p_0 \approx \tilde{b}_0 + \tilde{c}_0$, which fixes the saturation energy to high precision. At the same time, the component $p_4 \approx \tilde{b}_0 - \tilde{c}_0$ in NEDF-1 (and similarly in NEDF-3n) is not well constrained. We also see that the least-significant component $p_5 \approx \tilde{a}_1 - \tilde{b}_1$ is essentially unconstrained. For NEDF-3, we find three insensitive components, two of which can be used to set the smallest parameters $a_0 = c_1 = 0$. After removing these, one obtains a similar analysis as for NEDF-1 above.

In this approximation, we can get both correct behavior for the nucleus density in the near and asymptotic region. Through varying the parameter κ we obtain the following fits.

NEDF-En-pade-1: Following NEDF-En-so, we use the Padé approximation for the kinetic energy and the parameter $b = 0.065$.
NEDF-En-pade-2: Same with NEDF-En-pade-1, but $\kappa = 0.15$.
NEDF-En-pade-3: Same with NEDF-En-pade-1, but $\kappa = 0.2$.
NEDF-En-pade-4: Same with NEDF-En-pade-1, but $\kappa = 0.3$.

These fits are summarized in Table IV, with the saturation and symmetry properties in Table V. The residuals for fit NEDF-1 are shown in Fig. 19 and compared with a fit to the nuclear with mass formula Eq. (2).

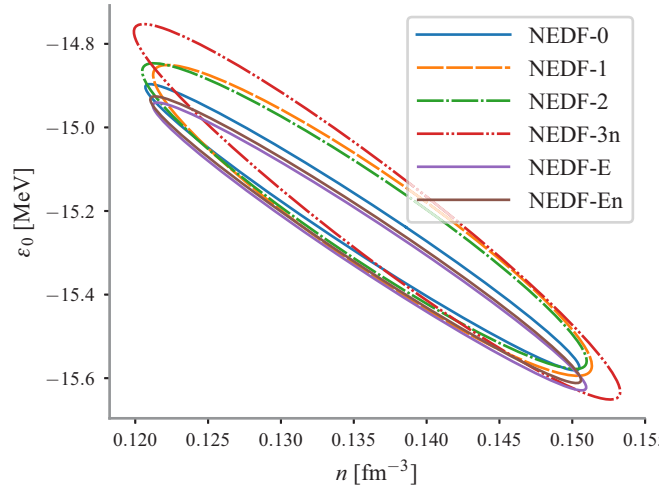

FIG. 21. The various ellipses show the region in the (ε_0, n_0) plane, in which the NEDF parameters can be changed and to lead to changes in the residual $\delta\chi_E < 0.2$ MeV. While the equilibrium energy ε_0 and density n_0 are controlled mainly by the combination $\tilde{b}_0 + \tilde{c}_0$, which is constrained with very high precision, the combination $\tilde{b}_0 - \tilde{c}_0$ has significantly less constraint; see Sec. III I. This aspect allows us to manipulate to a certain degree the saturation properties, while affecting the overall fit only slightly.

The reduced χ_E for these fits is comparable to that obtained using the nuclear mass formulas Eq. (1) with four parameters (plus δ) and Eq. (2) with five parameters (plus δ). This is consistent with our hypothesis that a NEDF for masses should contain no more than five significant parameters. Note, however, that unlike the mass formulas, the NEDF also gives a good description of charge radii—for which the mass formula says nothing—and provides access to nuclear dynamics.

APPENDIX C: PRINCIPAL COMPONENT ANALYSIS

The principal components for fits NEDF-1 and NEDF-3 are shown in Fig. 20.

In the case of NEDF-3, we see that two parameters are completely unconstrained. These include $\tilde{a}_0 \approx -0.088$ and $\tilde{c}_1 = -0.017$. These values are an order of magnitude smaller than the other coefficients: Hence, the unconstrained components can be easily removed by setting $a_0 = c_1 = 0$, which we do in most of our fits.

Finally, both plots indicate that a combination of the $j = 1$ parameters is highly unconstrained. Thus, in NEDF-1, the combination $\tilde{b}_1 - \tilde{a}_1$ can be given almost any value of order unity without changing χ_E more than 0.1 MeV. This is directly tested in the changes from NEDF1 to NEDF-E, NEDF-Er, NEDF-En, and NEDF-Enr, where we change the sign of b_1 and set $a_1 = b_1 n_0^{2/3}$. Indeed, we see that χ_E changed by about 0.1 MeV. Notice from Table V that the slope of the symmetry energy L_2 changes from about 30 to 70 MeV while the other parameters remain about the same. This also significantly changes the neutron skin thickness, demonstrating a correlation between L_2 and the skin thickness, similar to that seen in other mean-field models [257]. This is consistent with Eq. (27e)

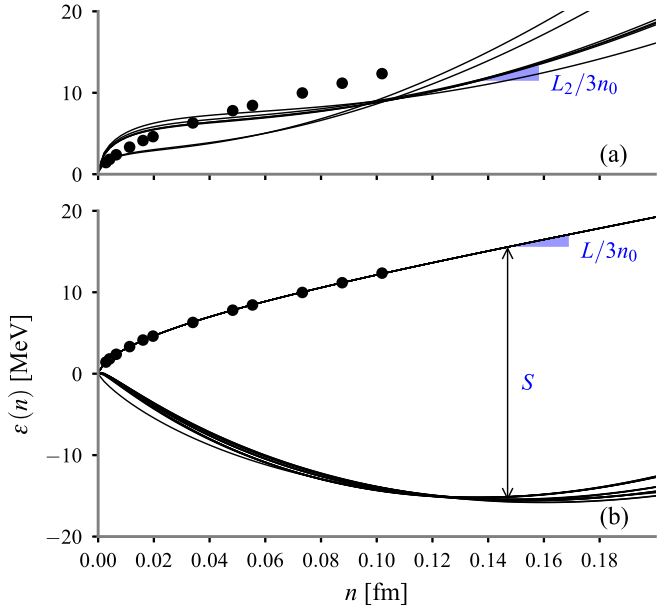

FIG. 22. The energy density per nucleon for (a), pure neutron matter for NEDF-0, 1, 1r, 2, 3, E, and Er, which do not constrain the neutron EoS and have only β^2 contributions; and (b), symmetric nuclear matter for all orbital-free functionals, and neutron matter for NEDF-3n, 3nr, En, and Enr, which collapse to the single curve fitting the QMC results [131] (dots).

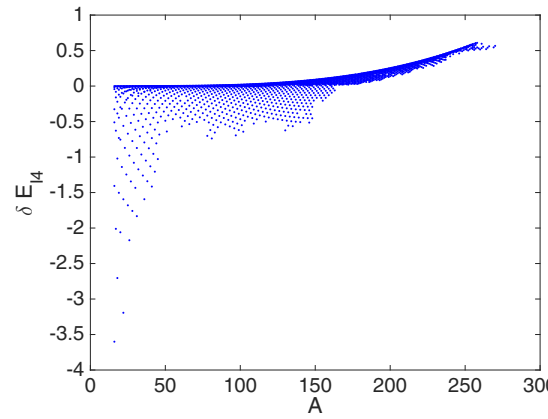

FIG. 23. The contribution to the ground-state energies of the terms quartic in isospin density $\delta E_{I4} = \int \mathrm{d}^3\boldsymbol{r}\ \mathcal{E}_2(n)\beta^4$, evaluated perturbatively with NEDF-1; see Table IV.

where we see that $\tilde{b}_1$ gives us a direct handle on L_2. Finally, we have some unconstrained parameters, including $\tilde{\delta}$.

APPENDIX D: SATURATION, SYMMETRY PROPERTIES, AND NEUTRON MATTER

When only β^2 isospin contributions are included in the functional, our fits to the nuclear binding energies display a feature reported in other NEDF discussed in literature: The energy per neutron in pure neutron matter appears to be well constrained at a density of $n_n \approx 0.1\,\mathrm{fm}^{-3}$ where all functionals cross; see Fig. 22. The symmetry energy S is indicated for the functionals NEDF-En and Enr. The slope $L \approx 30\,\mathrm{MeV}$ is fixed by the neutron matter EoS alone [if used as a constraint, see Eq. (26b)]. In this case, the slope $L_2/3n_0$ may be tuned without significantly affecting the mass fit by adjusting the insensitive combination $a_1 - b_1 n_0^{1/3}$ or c_1; see Sec. III I. Functionals with only quadratic isospin contributions (β^2) appear to cross near $n \approx 0.1\,\mathrm{fm}^{-3}$; see also Ref. [258] and references therein. However, the value for the energy per neutron $\approx 9\,\mathrm{MeV}$ at this point in our fits is significantly smaller than the value $\approx 12.19\,\mathrm{MeV}$ obtained in QMC calculations of Wlazłowski *et al.* [131] or the equations of state for neutron matter used by Fayans [143] and Baldo *et al.* [211–213]; see Fig. 18. This feature is not present when the β^4 terms are included (NEDF-3n, NEDF-3nr, NEDF-En, and NEDF-Enr) and the QMC results are thus automatically reproduced.

The inclusion of the $j = 2$ terms quartic in β^4 has very little significance on mass fits. This demonstrates an important point: The EoS of pure neutron matter has very little impact on the form of the NEDF if only nuclei are considered. In measured nuclei, the ratio $\beta = (n_n - n_p)/n \approx (N - Z)/A$ is $|\beta| < 1/4$ (with a very small number of exceptions); hence nuclear masses are essentially insensitive to the presence of the β^4 terms, as $|\beta|^4 < 1/256$. To assess the magnitude of these effects, we have evaluated the β^4 contributions to the nuclear binding energies perturbatively; see Fig. 23. This contribution is quite small and can be easily overlooked when discussing known nuclei, but is crucial in order to correctly reproduce the energy of neutron matter. By evaluating Eq. (28) at $n = 0.1\,\mathrm{fm}^{-3}$ one obtains

$$\left.\frac{\mathcal{E}}{n}\right|_{n=0.1} = [-4.399 + 13.961\beta^2 + 2.635\beta^4]\ \mathrm{MeV}. \quad \text{(D1)}$$

When one averages β^2 and β^4 over all nuclei, one obtains the values 0.028 and 0.001 respectively, which are noticeably lower than the "maximum" values of $1/16 \approx 0.062$ and $1/256 \approx 0.004$ and thus the contribution of the terms in β^4 to χ_E and nuclear masses is further reduced. The contributions of these terms to the averaged energy density per nucleon over β at $n = 0.1\,\mathrm{fm}^{-3}$ are

$$\left.\frac{\mathcal{E}}{n}\right|_{n=0.1} = [-4.399 + 0.391 + 0.0026]\ \mathrm{MeV}, \quad \text{(D2)}$$

and the contribution of the quartic term in β to the total energy is practically invisible in nuclei.

Thus, using properties of the neutron matter to constrain the form of the NEDF and/or arguing against the inclusion of higher powers of $(n_n - n_p)$ [71,143,161,211,212,259–262] is an ill-advised procedure, and the applications of functionals constructed in this manner, in particular to star environments, should be regarded with suspicion. The statement often made in the literature (see, e.g., Horowitz *et al.* [258] and references therein) that the value of the symmetry energy at $n \approx 0.1\,\mathrm{fm}^{-3}$ is well constrained by nuclear masses must only be applied to the local expansion S_2 at this density but not to the symmetry energy difference S between symmetric and pure neutron matter.

APPENDIX E: CHARGE FORM FACTORS

The charge form factors are determined experimentally, and we approximate the Fourier transforms of the form factors with the dipole term for the proton, $G_E^p(Q) \approx (1 + Q^2/0.71\,\mathrm{GeV}^2)^{-2}$ [263], and $G_E^n(Q) \approx a(1 + Q^2 r_+^2/12)^{-2} - a(1 + Q^2 r_-^2/12)^{-2}$ with $r_\pm^2 = r_{\mathrm{avg}}^2 \pm \langle r_n^2\rangle/2a$, $\langle r_n^2\rangle = -0.1147(35)\,\mathrm{fm}^2$, $r_{\mathrm{avg}} = 0.856(32)\,\mathrm{fm}$, and $a = 0.115(20)$ [264].

[1] P. Hohenberg and W. Kohn, Inhomogeneous electron gas, Phys. Rev. **136**, B864 (1964).
[2] R. M. Dreizler and E. K. U. Gross, *Density Functional Theory: An Approach to the Quantum Many–Body Problem* (Springer-Verlag, Berlin, 1990).
[3] M. Bender, P.-H. Heenen, and P.-G. Reinhard, Self-consistent mean-field models for nuclear structure, Rev. Mod. Phys. **75**, 121 (2003).
[4] DOE SCIDAC UNEDF Project [http://unedf.mps.ohio-state.edu].
[5] DOE SCIDAC NUCLEI Project [http://nuclei.mps.ohio-state.edu].
[6] P.-G. Reinhard, Estimating the relevance of predictions from the Skyrme-Hartree-Fock model, Phys. Scr. **91**, 023002 (2016).
[7] S. Goriely, Further explorations of Skyrme-Hartree-Fock-Bogoliubov mass formulas, XV: The spin-orbit coupling, Nucl. Phys. A **933**, 68 (2015).
[8] S. Goriely, N. Chamel, and J. M. Pearson, Further explorations of Skyrme-Hartree-Fock-Bogoliubov mass formulas, XVI: Inclusion of self-energy effects in pairing, Phys. Rev. C **93**, 034337 (2016).
[9] S. Goriely, S. Hilaire, M. Girod, and S. Péru, The Gogny-Hartree-Fock-Bogoliubov nuclear-mass model, Eur. Phys. J. A **52**, 202 (2016).
[10] W. Kohn and L. J. Sham, Self-consistent equations including exchange and correlation effects, Phys. Rev. **140**, A1133 (1965).
[11] C. F. v. Weizsäcker, Zur Theorie der Kernmassen, Z. Phys. A **96**, 431 (1935).
[12] H. A. Bethe and R. F. Bacher, Nuclear physics A: Stationary states of nuclei, Rev. Mod. Phys. **8**, 82 (1936).
[13] See Supplemental Material at http://link.aps.org/supplemental/10.1103/PhysRevC.97.044313 for details about our simulations, comparison of fermionic and bosonic simulations and list of movies.
[14] F. W. Aston, Isotopes and atomic weights, Nature (London) **105**, 605 (1920).
[15] A. S. Eddington, The internal constitution of the stars, Nature (London) **106**, 14 (1920).
[16] M. R. Mumpower, R. Surman, G. C. McLaughlin, and A. Aprahamian, The impact of individual nuclear properties on *r*-process nucleosynthesis, Prog. Part. Nucl. Phys. **86**, 86 (2016).
[17] M. R. Mumpower, R. Surman, G. C. McLaughlin, and A. Aprahamian, Corrigendum to "The impact of individual nuclear properties on *r*-process nucleosynthesis" [J. Prog. Part. Nucl. Phys. 86C (2015) 86–126], Prog. Part. Nucl. Phys. **87**, 116 (2016).
[18] G. Audi, M. Wang, A. H. Wapstra, F. G. Kondev, M. MacCormick, X. Xu, and B. Pfeiffer, The AME2012 atomic mass evaluation, Chin. Phys. C **36**, 1287 (2012).
[19] M. Wang, G. Audi, A. H. Wapstra, F. G. Kondev, M. MacCormick, X. Xu, and B. Pfeiffer, The AME2012 atomic mass evaluation, Chin. Phys. C **36**, 1603 (2012).
[20] P.-G. Reinhard, M. Bender, W. Nazarewicz, and T. Vertse, From finite nuclei to the nuclear liquid drop: Leptodermous expansion based on self-consistent mean-field theory, Phys. Rev. C **73**, 014309 (2006).
[21] H. Weyl, Über die Asymptotische Verteilung der Eigenwerte, Nachr. Königl. Ges. Wiss. Göttingen **2**, 110 (1911).
[22] H. Weyl, Das Asymptotische Verteilungsgesetz der Eigenwerte Linearer Partieller Differentialgleichungen (Mit Einer Anwendung Auf die Theorie der Hohlraumstrahlung), Math. Ann. **71**, 441 (1912).
[23] H. Weyl, Über die Abhängigkeit der Eigenschwingungen Einer Membran und Deren Begrenzung, J. Reine Angew. Math. **1912**, 1 (1912).
[24] H. Weyl, Über das Spektrum der Hohlraumstrahlung, J. Reine Angew. Math. **1912**, 163 (1912).
[25] H. Weyl, Über die Randwertaufgabe der Strahlungstheorie und Asymptotische Spektralgesetze, J. Reine Angew. Math. **1913**, 177 (1913).
[26] H. Weyl, Das Asymptotische Verteilungsgesetz der Eigenschwingungen Eines Beliebig Gestalteten Elastischen Körpers, Rend. Circ. Mat. Palermo **39**, 1 (1915).
[27] H. Weyl, Ramifications, old and new, of the eigenvalue problem, Bull. Amer. Math. Soc. **56**, 115 (1950).
[28] M. Kac, Can one hear the shape of a drum? Am. Math. Mon. **73**, 1 (1966).
[29] R. T. Waechter, On hearing the shape of a drum: An extension to higher dimensions, Math. Proc. Cambridge Philos. Soc. **72**, 439 (1972).
[30] H. P. Baltes and E. R. Hilf, *Spectra of Finite Systems* (Bibliographisches Institut, Mannheim, 1976).
[31] M. Brack and R. K Bhaduri, *Semiclassical Physics*, Frontiers in Physics (Addison-Wesley, Reading, MA, 1997), Vol. 96.
[32] R. Balian and C. Bloch, Distribution of eigenfrequencies for the wave equation in a finite domain: I. Three-dimensional problem with smooth boundary surface, Ann. Phys. (N.Y.) **60**, 401 (1970).
[33] R. Balian and C. Bloch, Distribution of eigenfrequencies for the wave equation in a finite domain, II: Electromagnetic field, Riemannian spaces, Ann. Phys. (N.Y.) **64**, 271 (1971).
[34] R. Balian and C. Bloch, Distribution of eigenfrequencies for the wave equation in a finite domain, III: Eigenfrequency density oscillations, Ann. Phys. (N.Y.) **69**, 76 (1972).
[35] V. M. Strutinsky and A. G. Magner, Semi-classical theory for nuclear shell structure, Fiz. Elem. Chastits At. Yadra **7**, 356 (1976) [Sov. J. Part. Nucl. **7**, 138 (1976)].
[36] O. Bohigas, S. Tomsovic, and D. Ullmo, Manifestations of classical phase space structures in quantum mechanics, Phys. Rep. **223**, 43 (1993).
[37] C. W. Johnson, G. F. Bertsch, and D. J. Dean, Orderly Spectra from Random Interactions, Phys. Rev. Lett. **80**, 2749 (1998).
[38] M. C. Gutzwiller, Periodic orbits and classical quantization conditions, J. Math. Phys. **12**, 343 (1971).

[39] M. V. Berry and M. Tabor, Closed orbits and the regular bound spectrum, Proc. R. Soc. London, Ser. A **349**, 101 (1976).

[40] M. V. Berry and M Tabor, Calculating the bound spectrum by path summation in action-angle variables, J. Phys. A: Math. Gen. **10**, 371 (1977).

[41] O. Haxel, J. H. D. Jensen, and H. E. Suess, On the "magic numbers" in nuclear structure, Phys. Rev. **75**, 1766 (1949).

[42] M. Goeppert Mayer, On closed shells in nuclei, II, Phys. Rev. **75**, 1969 (1949).

[43] M. Goeppert Mayer, Nuclear configurations in the spin-orbit coupling model, I: Empirical evidence, Phys. Rev. **78**, 16 (1950).

[44] M. Goeppert Mayer, Nuclear configurations in the spin-orbit coupling model, II: Theoretical considerations, Phys. Rev. **78**, 22 (1950).

[45] L. D. Landau, Theory of Fermi liquids, Zh. Eksp. Teor. Fiz. **30**, 1058 (1956) [Sov. Phys. JETP **3**, 920 (1956)].

[46] L. D. Landau, Oscillations of a Fermi liquid, Zh. Eksp. Teor. Fiz. **32**, 59 (1957) [Sov. Phys. JETP **5**, 101 (1957)].

[47] A. B. Migdal, *Theory of Finite Fermi Systems and Applications to Atomic Nuclei* (Wiley, New York, 1967).

[48] H. Nishioka, K. Hansen, and B. R. Mottelson, Supershells in metal clusters, Phys. Rev. B **42**, 9377 (1990).

[49] W. A. de Heer, The physics of simple metal clusters: Experimental aspects and simple models, Rev. Mod. Phys. **65**, 611 (1993).

[50] M. Brack, The physics of simple metal clusters: Self-consistent jellium model and semiclassical approaches, Rev. Mod. Phys. **65**, 677 (1993).

[51] J. Pedersen, S. Bjornholm, J. Borggreen, K. Hansen, T. P. Martin, and H. D. Rasmussen, Observation of quantum supershells in clusters of sodium atoms, Nature (London) **353**, 733 (1991).

[52] A. Bulgac and C. Lewenkopf, Stable Deformations in Large Metallic Clusters, Phys. Rev. Lett. **71**, 4130 (1993).

[53] V. M. Strutinsky, Influence of nucleon shells on energy of a nucleus, Yad. Fiz. **3**, 614 (1966) [Sov. J. Nucl. Phys. **3**, 449 (1966)].

[54] V. M. Strutinsky, Shell effects in nuclear masses and deformation energies, Nucl. Phys. A **95**, 420 (1967).

[55] V. M. Strutinsky, "Shells" in deformed nuclei, Nucl. Phys. A **122**, 1 (1968).

[56] M. Brack, J. Damgaard, A. S. Jensen, H. C. Pauli, V. M. Strutinsky, and C. Y. Wong, Funny hills: The shell-correction approach to nuclear shell effects and its applications to the fission process, Rev. Mod. Phys. **44**, 320 (1972).

[57] M. Brack, C. Guet, and H. B. Håkansson, Self-consistent semiclassical description of average nuclear properties—a link between microscopic and macroscopic models, Phys. Rep. **123**, 275 (1985).

[58] W. D. Myers and W. J. Swiatecki, Nuclear masses and deformations, Nucl. Phys. **81**, 1 (1966).

[59] W. D. Myers and W. J. Swiatecki, Average nuclear properties, Ann. Phys. (N.Y.) **55**, 395 (1969).

[60] W. D. Myers and W. J. Swiatecki, The nuclear droplet model for arbitrary shapes, Ann. Phys. (N.Y.) **84**, 186 (1974).

[61] W. D. Myers and W. J. Swiatecki, A Thomas-Fermi model of nuclei, part i: Formulation and first results, Ann. Phys. (N.Y.) **204**, 401 (1990).

[62] W. D. Myers and W. J. Swiatecki, A Thomas-Fermi model of nuclei, II: Fission barriers and charge distributions, Ann. Phys. (N.Y.) **211**, 292 (1991).

[63] W. D. Myers and W. J. Swiatecki, Nuclear properties according to the Thomas-Fermi model, Nucl. Phys. A **601**, 141 (1996).

[64] P. Ring and P. Schuck, *The nuclear many-body problem*, 1st ed., Theoretical and Mathematical Physics Series (Springer-Verlag, Berlin, 2004), Vol. 17.

[65] A. Bohr and B. R. Mottelson, *Nuclear Structure* (World Scientific, Singapore, 1998).

[66] P. Moller, J. R. Nix, W. D. Myers, and W. J. Swiatecki, Nuclear ground-state masses and deformations, At. Data Nucl. Data Tables **59**, 185 (1995).

[67] P. Möller, W. D. Myers, H. Sagawa, and S. Yoshida, New Finite-Range Droplet Mass Model and Equation-of-State Parameters, Phys. Rev. Lett. **108**, 052501 (2012).

[68] P. Möller, A. J. Sierk, T. Ichikawa, and H. Sagawa, Nuclear ground-state masses and deformations: FRDM(2012), At. Data Nucl. Data Tables **109**, 1 (2016).

[69] S. Goriely, N. Chamel, and J. M. Pearson, Skyrme-Hartree-Fock-Bogoliubov Nuclear Mass Formulas: Crossing the 0.6 Mev Accuracy Threshold with Microscopically Deduced Pairing, Phys. Rev. Lett. **102**, 152503 (2009).

[70] J. P. Delaroche, M. Girod, J. Libert, H. Goutte, S. Hilaire, S. Péru, N. Pillet, and G. F. Bertsch, Structure of even-even nuclei using a mapped collective Hamiltonian and the D1S Gogny interaction, Phys. Rev. C **81**, 014303 (2010).

[71] S. Goriely, N. Chamel, and J. M. Pearson, Hartree-Fock-Bogoliubov nuclear mass model with 0.50 MeV accuracy based on standard forms of Skyrme and pairing functionals, Phys. Rev. C **88**, 061302 (2013).

[72] S. Goriely and R. Capote, Uncertainties of mass extrapolations in Hartree-Fock-Bogoliubov mass models, Phys. Rev. C **89**, 054318 (2014).

[73] M. Kortelainen, T. Lesinski, J. Moré, W. Nazarewicz, J. Sarich, N. Schunck, M. V. Stoitsov, and S. Wild, Nuclear energy density optimization, Phys. Rev. C **82**, 024313 (2010).

[74] M. Kortelainen, J. McDonnell, W. Nazarewicz, P.-G. Reinhard, J. Sarich, N. Schunck, M. V. Stoitsov, and S. M. Wild, Nuclear energy density optimization: Large deformations, Phys. Rev. C **85**, 024304 (2012).

[75] M. Kortelainen, J. McDonnell, W. Nazarewicz, E. Olsen, P.-G. Reinhard, J. Sarich, N. Schunck, S. M. Wild, D. Davesne, J. Erler, and A. Pastore, Nuclear energy density optimization: Shell structure, Phys. Rev. C **89**, 054314 (2014).

[76] D. Lunney, J. M. Pearson, and C. Thibault, Recent trends in the determination of nuclear masses, Rev. Mod. Phys. **75**, 1021 (2003).

[77] A. Bohr and B. R. Mottelson, *Nuclear Structure* (Benjamin, New York, 1969), Vol. 1.

[78] O. Bohigas and P. Leboeuf, Nuclear Masses: Evidence of Order-Chaos Coexistence, Phys. Rev. Lett. **88**, 092502 (2002); Erratum: Nuclear Masses: Evidence of Order-Chaos Coexistence [Phys. Rev. Lett. **88**, 092502 (2002)] **88**, 129903(E) (2002).

[79] S. Åberg, Nuclear physics: Weighing up nuclear masses, Nature (London) **417**, 499 (2002).

[80] H. Olofsson, S. Åberg, O. Bohigas, and P. Leboeuf, Correlations in Nuclear Masses, Phys. Rev. Lett. **96**, 042502 (2006).

[81] H. Olofsson, S. Åberg, and P. Leboeuf, Semiclassical Theory of Bardeen-Cooper-Schrieffer Pairing-Gap Fluctuations, Phys. Rev. Lett. **100**, 037005 (2008).

[82] A. Molinari and H. A. Weidenmüller, Statistical fluctuations of ground-state energies and binding energies in nuclei, Phys. Lett. B **601**, 119 (2004).

[83] A. Molinari and H. A. Weidenmüller, Nuclear masses, chaos, and the residual interaction, Phys. Lett. B **637**, 48 (2006).

[84] J. G. Hirsch, V. Velázquez, and A. Frank, Quantum chaos and nuclear mass systematics, Phys. Lett. B **595**, 231 (2004).

[85] J. G. Hirsch, A. Frank, J. Barea, P. Van Isacker, and V. Velázquez, Bounds on the presence of quantum chaos in nuclear masses, Eur. J. Phys. A **25**, 75 (2005).

[86] J. Barea, A. Frank, J. G. Hirsch, and P. Van Isacker, Nuclear Masses Set Bounds on Quantum Chaos, Phys. Rev. Lett. **94**, 102501 (2005).

[87] H. B. G. Casimir, On the attraction between two perfectly conducting plates, Proc. K. Ned. Akad. Wet. **51**, 793 (1948).

[88] G. L. Klimchitskaya, U. Mohideen, and V. M. Mostepanenko, The Casimir force between real materials: Experiment and theory, Rev. Mod. Phys. **81**, 1827 (2009).

[89] M. E. Fisher and P. G. de Gennes, Phénomènes Aux Parois Dans un Mélange Binaire Critique, C. R. Acad. Sci. Ser. B **287**, 207 (1978).

[90] A. Hanke, F. Schlesener, E. Eisenriegler, and S. Dietrich, Critical Casimir Forces Between Spherical Particles in Fluids, Phys. Rev. Lett. **81**, 1885 (1998).

[91] A. Bulgac and P. Magierski, Quantum corrections to the ground state energy of inhomogeneous neutron matter, Nucl. Phys. A **683**, 695 (2001); Erratum to "Quantum corrections to the ground state energy of inhomogeneous neutron matter," **703**, 892 (2002).

[92] P. Magierski, A. Bulgac, and P.-H. Heenen, Exotic nuclear phases in the inner crust of neutron stars in the light of Skyrme-Hartree-Fock theory, Nucl. Phys. A **719**, C217 (2003).

[93] P. Magierski and A. Bulgac, Nuclear structure and dynamics in the inner crust of neutron stars, Nucl. Phys. A **738**, 143 (2004).

[94] P. Magierski and P.-H. Heenen, Structure of the inner crust of neutron stars: Crystal lattice or disordered phase? Phys. Rev. C **65**, 045804 (2002).

[95] A. Bulgac, P. Magierski, and A. Wirzba, Fermionic Casimir effect in case of Andreev reflection, Europhys. Lett. **72**, 327 (2005).

[96] Y. Yu, A. Bulgac, and P. Magierski, Shell Correction Energy for Bubble Nuclei, Phys. Rev. Lett. **84**, 412 (2000).

[97] A. Bulgac, P. Magierski, and A. Wirzba, Scalar Casimir effect between Dirichlet spheres or a plate and a sphere, Phys. Rev. D **73**, 025007 (2006).

[98] M. Bordag and I. Pirozhenko, Vacuum energy between a sphere and a plane at finite temperature, Phys. Rev. D **81**, 085023 (2010).

[99] S. J. Rahi, T. Emig, N. Graham, R. L. Jaffe, and M. Kardar, Scattering theory approach to electrodynamic Casimir forces, Phys. Rev. D **80**, 085021 (2009).

[100] N. Graham, Casimir energies of periodic dielectric gratings, Phys. Rev. A **90**, 032507 (2014).

[101] A. Canaguier-Durand, P. A. Maia Neto, A. Lambrecht, and S. Reynaud, Thermal Casimir effect for Drude metals in the plane-sphere geometry, Phys. Rev. A **82**, 012511 (2010).

[102] M. Schaden, Semiclassical estimates of electromagnetic Casimir self-energies of spherical and cylindrical metallic shells, Phys. Rev. A **82**, 022113 (2010).

[103] H. A. Jahn and E. Teller, Stability of polyatomic molecules in degenerate electronic states, I: Orbital degeneracy, Proc. R. Soc. London, Ser. A **161**, 220 (1937).

[104] A. Bulgac and V. R. Shaginyan, A systematic surface contribution to the ground-state binding energies, Nucl. Phys. A **601**, 103 (1996).

[105] P. Möller, J. R. Nix, and K. L. Kratz, Nuclear properties for astrophysical and radioactive ion beam applications, At. Data Nucl. Data Tables **66**, 131 (1997).

[106] J. Carlson, S. Gandolfi, F. Pederiva, Steven C. Pieper, R. Schiavilla, K. E. Schmidt, and R. B. Wiringa, Quantum Monte Carlo methods for nuclear physics, Rev. Mod. Phys. **87**, 1067 (2015).

[107] F. Pederiva, A. Roggero, and K. E. Schmidt, Variational and diffusion Monte Carlo approaches to the nuclear few- and many-body problem, in *An Advanced Course in Computational Nuclear Physics: Bridging the Scales from Quarks to Neutron Stars*, edited by M. Hjorth-Jensen, M. Paola Lombardo, and U. van Kolck (Springer, Cham, 2017), pp. 401–476.

[108] C. Barbieri and A. Carbone, Self-consistent Green's function approaches, in *An Advanced Course in Computational Nuclear Physics: Bridging the Scales from Quarks to Neutron Stars*, edited by M. Hjorth-Jensen, M. Paola Lombardo, and U. van Kolck (Springer, Cham, 2017), pp. 571–644.

[109] J. G. Lietz, S. Novario, G. R. Jansen, G. Hagen, and M. Hjorth-Jensen, Computational nuclear physics and post-Hartree-Fock methods, in *An Advanced Course in Computational Nuclear Physics: Bridging the Scales from Quarks to Neutron Stars*, edited by M. Hjorth-Jensen, M. Paola Lombardo, and U. van Kolck (Springer, Cham, 2017), pp. 293–399.

[110] E. Gebrerufael, K. Vobig, H. Hergert, and R. Roth, Ab Initio Description of Open-Shell Nuclei: Merging No-Core Shell Model and In-Medium Similarity Renormalization Group, Phys. Rev. Lett. **118**, 152503 (2017).

[111] E. Epelbaum, H. Krebs, D. Lee, and U.-G. Meißner, *Ab initio* calculation of the Hoyle state, Phys. Rev. Lett. **106**, 192501 (2011).

[112] R. Machleidt and D. R. Entem, Chiral effective field theory and nuclear forces, Phys. Rep. **503**, 1 (2011).

[113] E. Kozik, K. Van Houcke, E. Gull, L. Pollet, N. Prokof'ev, B. Svistunov, and M. Troyer, Diagrammatic Monte Carlo for correlated fermions, Europhys. Lett. **90**, 10004 (2010).

[114] R. Rossi, N. Prokof'ev, B. Svistunov, K. Van Houcke, and F. Werner, Polynomial complexity despite the fermionic sign, Europhys. Lett. **118**, 10004 (2017).

[115] J. Carlson, S.-Y. Chang, V. R. Pandharipande, and K. E. Schmidt, Superfluid Fermi Gases with Large Scattering Length, Phys. Rev. Lett. **91**, 050401 (2003).

[116] A. Bulgac, Time-dependent density functional theory and the real-time dynamics of Fermi superfluids, Annu. Rev. Nucl. Part. Sci. **63**, 97 (2013).

[117] A. Bulgac, M. McNeil Forbes, and G. Wlazłowski, Towards quantum turbulence in cold atomic fermionic superfluids, J. Phys. B **50**, 014001 (2017).

[118] I. Angeli and K. P. Marinova, Table of experimental nuclear ground state charge radii: An update, At. Data Nucl. Data Tables **99**, 69 (2013).

[119] S. Jin, A. Bulgac, K. Roche, and G. Wlazłowski, Coordinate-space solver for superfluid many-fermion systems with the shifted conjugate-orthogonal conjugate-gradient method, Phys. Rev. C **95**, 044302 (2017).

[120] Y. M. Engel, D. M. Brink, K. Goeke, S. J. Krieger, and D. Vautherin, Time-dependent Hartree-Fock theory with Skyrme's interaction, Nucl. Phys. A **249**, 215 (1975).

[121] J. Dobaczewski and J. Dudek, Time-odd components in the mean field of rotating superdeformed nuclei, Phys. Rev. C **52**, 1827 (1995).

[122] V. O. Nesterenko, W. Kleinig, J. Kvasil, P. Vesely, and P.-G. Reinhard, TDDFT with Skyrme forces: Effect of time-odd densities on electric giant resonances, Int. J. Mod. Phys. E **17**, 89 (2008).

[123] A. Bulgac, M. McNeil Forbes, and P. Magierski, *The unitary Fermi gas: From Monte Carlo to density functionals*, in *The BCS–BEC Crossover and the Unitary Fermi Gas*, Lecture Notes in Physics, edited by W. Zwerger (Springer-Verlag, Berlin, 2012), Vol. 836, Chap. 9, pp. 305–373.

[124] G. A. Miller, B. M. K. Nefkens, and I. Slaus, Charge symmetry, quarks and mesons, Phys. Rep. **194**, 1 (1990).

[125] G. A. Miller, A. K. Opper, and E. J. Stephenson, Charge symmetry breaking and QCD, Annu. Rev. Nucl. Part. Sci. **56**, 253 (2006).

[126] H. Müther, A. Polls, and R. Machleidt, Isospin symmetry breaking nucleon-nucleon potentials and nuclear structure, Phys. Lett. B **445**, 259 (1999).

[127] R. Machleidt and H. Müther, Charge symmetry breaking of the nucleon-nucleon interaction: ρ-ω mixing versus nucleon mass splitting, Phys. Rev. C **63**, 034005 (2001).

[128] U. G. Meißner, A. M. Rakhimov, A. Wirzba, and U. T. Yakhshiev, Neutron-proton mass difference in finite nuclei and the Nolen-Schiffer anomaly, Eur. Phys. J. A **36**, 37 (2008).

[129] J. A. Nolen and J. P. Schiffer, Coulomb energies, Annu. Rev. Nucl. Sci. **19**, 471 (1969).

[130] A. Bulgac and V. R. Shaginyan, Proton single-particle energy shifts due to Coulomb correlations, Phys. Lett. B **469**, 1 (1999).

[131] G. Wlazłowski, J. W. Holt, S. Moroz, A. Bulgac, and K. J. Roche, Auxiliary-Field Quantum Monte Carlo Simulations of Neutron Matter in Chiral Effective Field Theory, Phys. Rev. Lett. **113**, 182503 (2014).

[132] F. Tondeur, An energy density nuclear mass formula: (i) Self-consistent calculation for spherical nuclei, Nucl. Phys. A **303**, 185 (1978).

[133] A. Gezerlis and J. Carlson, Low-density neutron matter, Phys. Rev. C **81**, 025803 (2010).

[134] S. Gandolfi, A. Gezerlis, and J. Carlson, Neutron matter from low to high density, Annu. Rev. Nucl. Part. Sci. **65**, 303 (2015).

[135] *The BCS–BEC Crossover and the Unitary Fermi Gas*, edited by W. Zwerger, Lecture Notes in Physics (Springer-Verlag, Berlin, 2012), Vol. 836.

[136] George A. Baker Jr., Neutron matter model, Phys. Rev. C **60**, 054311 (1999).

[137] A. Bulgac, M. McNeil Forbes, and S. Jin, The nuclear energy density functional: What do we really know? arXiv:1506.09195 (unpublished).

[138] J. Carlson and S. Reddy, Asymmetric Two-Component Fermion Systems in Strong Coupling, Phys. Rev. Lett. **95**, 060401 (2005).

[139] P. Magierski, G. Wlazłowski, A. Bulgac, and J. E. Drut, Finite-Temperature Pairing Gap of a Unitary Fermi Gas by Quantum Monte Carlo Calculations, Phys. Rev. Lett. **103**, 210403 (2009).

[140] P. Magierski, G. Wlazłowski, and A. Bulgac, Onset of a Pseudogap Regime in Ultracold Fermi Gases, Phys. Rev. Lett. **107**, 145304 (2011).

[141] A. Bulgac, Local density functional theory for superfluid fermionic systems: The unitary gas, Phys. Rev. A **76**, 040502 (2007).

[142] E. Chabanat, P. Bonche, P. Haensel, J. Meyer, and R. Schaeffer, A Skyrme parametrization from subnuclear to neutron star densities, part II: Nuclei far from stabilities, Nucl. Phys. A **635**, 231 (1998).

[143] S. A. Fayans, Towards a universal nuclear density functional, JETP Lett. **68**, 169 (1998).

[144] A. Bulgac and Y. Yu, Renormalization of the Hartree-Fock-Bogoliubov Equations in the Case of a Zero Range Pairing Interaction, Phys. Rev. Lett. **88**, 042504 (2002).

[145] Y. Yu and A. Bulgac, Energy Density Functional Approach to Superfluid Nuclei, Phys. Rev. Lett. **90**, 222501 (2003).

[146] P. J. Borycki, J. Dobaczewski, W. Nazarewicz, and M. V. Stoitsov, Pairing renormalization and regularization within the local density approximation, Phys. Rev. C **73**, 044319 (2006).

[147] G. F. Bertsch, C. A. Bertulani, W. Nazarewicz, N. Schunck, and M. V. Stoitsov, Odd-even mass differences from self-consistent mean field theory, Phys. Rev. C **79**, 034306 (2009).

[148] T. Lesinski, T. Duguet, K. Bennaceur, and J. Meyer, Non-empirical pairing energy density functional, Eur. Phys. J. A **40**, 121 (2009).

[149] K. Hebeler, T. Duguet, T. Lesinski, and A. Schwenk, Non-empirical pairing energy functional in nuclear matter and finite nuclei, Phys. Rev. C **80**, 044321 (2009).

[150] M. Yamagami, J. Margueron, H. Sagawa, and K. Hagino, Isoscalar and isovector density dependence of the pairing functional determined from global fitting, Phys. Rev. C **86**, 034333 (2012).

[151] R. O. Jones and O. Gunnarsson, The density functional formalism, its applications and prospects, Rev. Mod. Phys. **61**, 689 (1989).

[152] A. E. DePristo and J. D. Kress, Kinetic-energy functionals via Padé approximations, Phys. Rev. A **35**, 438 (1987).

[153] G. F. Bertsch, B. Sabbey, and M. Uusnäkki, Fitting theories of nuclear binding energies, Phys. Rev. C **71**, 054311 (2005).

[154] R. Navarro Perez, N. Schunck, R.-D. Lasseri, C. Zhang, and J. Sarich, Axially deformed solution of the Skyrme-Hartree-Fock-Bogolyubov equations using the transformed harmonic oscillator basis (III) HFBTHO (v3.00): A new version of the program, Comput. Phys. Commun. **220**, 363 (2017).

[155] M. V. Stoitsov, N. Schunck, M. Kortelainen, N. Michel, H. Nam, E. Olsen, J. Sarich, and S. Wild, axially deformed solution of the Skyrme-Hartree-Fock-Bogoliubov equations using the transformed harmonic oscillator basis (II) HFBTHO v2.00d: A new version of the program, Comput. Phys. Commun. **184**, 1592 (2013).

[156] M. V. Stoitsov, J. Dobaczewski, W. Nazarewicz, and P. Ring, Axially deformed solution of the Skyrme–Hartree–Fock–Bogolyubov equations using the transformed harmonic oscillator basis. The program HFBTHO (v1.66p), Comput. Phys. Commun. **167**, 43 (2005).

[157] H. De Vries, C. W. De Jager, and C. De Vries, Nuclear charge-density-distribution parameters from elastic electron scattering, At. Data Nucl. Data Tables **36**, 495 (1987).

[158] J. M. Lattimer, Symmetry energy in nuclei and neutron stars, Nucl. Phys. A **928**, 276 (2014).

[159] C. J. Horowitz, K. S. Kumar, and R. Michaels, Electroweak measurements of neutron densities in CREX and PREX at JLab, USA, Eur. Phys. J. A **50**, 48 (2014).

[160] A. Tamii, I. Poltoratska, P. von Neumann-Cosel, Y. Fujita, T. Adachi, C. A. Bertulani, J. Carter, M. Dozono, H. Fujita, K. Fujita *et al.*, Complete Electric Dipole Response and the Neutron Skin in ^{208}Pb, Phys. Rev. Lett. **107**, 062502 (2011).

[161] P.-G. Reinhard and W. Nazarewicz, Information content of a new observable: The case of the nuclear neutron skin, Phys. Rev. C **81**, 051303 (2010).

[162] C. M. Tarbert, D. P. Watts, D. I. Glazier, P. Aguar, J. Ahrens, J. R. M. Annand, H. J. Arends, R. Beck, V. Bekrenev, B. Boillat *et al.*, Neutron Skin of 208Pb from Coherent Pion Photoproduction, Phys. Rev. Lett. **112**, 242502 (2014).

[163] N. Schwierz, I. Wiedenhover, and A. Volya, Parameterization of the Woods-Saxon potential for shell-model calculations, arXiv:0709.3525 [nucl-th] (unpublished).

[164] N. Schunck and L. M. Robledo, Microscopic theory of nuclear fission: A review, Rom. Rep. Phys. **79**, 116301 (2016).

[165] J. Dobaczewski and P. Olbratowski, Solution of the Skyrme-Hartree-Fock-Bogolyubov equations in the Cartesian deformed harmonic-oscillator basis. (IV) HFODD (v2.08i): A new version of the program, Comput. Phys. Commun. **158**, 158 (2004).

[166] N. Schunck, D. Duke, H. Carr, and A. Knoll, Description of induced nuclear fission with Skyrme energy functionals: Static potential energy surfaces and fission fragment properties, Phys. Rev. C **90**, 054305 (2014).

[167] J. Bartel, P. Quentin, M. Brack, C. Guet, and H.-B. Håkansson, Towards a better parametrisation of Skyrme-like effective forces: A critical study of the SkM force, Nucl. Phys. A **386**, 79 (1982).

[168] N. Schunck, J. D. McDonnell, J. Sarich, S. M. Wild, and D. Higdon, Error analysis in nuclear density functional theory, J. Phys. G: Nucl. Part. Phys. **42**, 034024 (2015).

[169] J. Erler, N. Birge, M. Kortelainen, W. Nazarewicz, E. Olsen, A. M. Perhac, and M. Stoitsov, The limits of the nuclear landscape, Nature (London) **486**, 509 (2012).

[170] R. Surman, M. Mumpower, and G. McLaughlin, Systematic and statistical uncertainties in simulated *r*-process abundances due to uncertain nuclear masses, JPS Conf. Proc. **14**, 010612 (2017).

[171] J. de Jesús Mendoza-Temis, M.-R. Wu, K. Langanke, G. Martínez-Pinedo, A. Bauswein, and H.-T. Janka, Nuclear robustness of the *r* process in neutron-star mergers, Phys. Rev. C **92**, 055805 (2015).

[172] J. Duflo and A. P. Zuker, Microscopic mass formulas, Phys. Rev. C **52**, R23 (1995).

[173] M. Bender, P.-H. Heenen, and P. Bonche, Microscopic study of ^{240}Pu: Mean field and beyond, Phys. Rev. C **70**, 054304 (2004).

[174] J. F. Berger, M. Girod, and D. Gogny, Constrained Hartree-Fock and beyond, Nucl. Phys. A **502**, 85 (1989).

[175] P. Möller, A. J. Sierk, T. Ichikawa, A. Iwamoto, R. Bengtsson, H. Uhrenholt, and S. Åberg, Heavy-element fission barriers, Phys. Rev. C **79**, 064304 (2009).

[176] R. Jodon, M. Bender, K. Bennaceur, and J. Meyer, Constraining the surface properties of effective Skyrme interactions, Phys. Rev. C **94**, 024335 (2016).

[177] A. Bulgac, lecture at LANL FIESTA Fission School and Workshop, September 17–22 (2017) [http://t2.lanl.gov/fiesta2017/agenda.shtml].

[178] B. S. Meyer, Decompression of initially cold neutron star matter: A mechanism for the *r*-process? Astrophys. J. **343**, 254 (1989).

[179] K. Langake and M. Wiescher, Nuclear reactions and stellar processes, Rep. Prog. Phys. **64**, 1657 (2001).

[180] S. Goriely, A. Bauswein, and H.-T. Janka, *r*-process nucleosynthesis in dynamically ejected matter of neutron star mergers, Astrophys. J. Lett. **738**, L32 (2011).

[181] S. Rosswog, O. Korobkin, A. Arcones, F.-K. Thielemann, and T. Piran, The long-term evolution of neutron star merger remnants, I: The impact of *r*-process nucleosynthesis, MNRAS **439**, 744 (2014).

[182] G. Baym, H. A. Bethe, and C. J. Pethick, Neutron star matter, Nucl. Phys. A **175**, 225 (1971).

[183] J. W. Negele and D. Vautherin, Neutron star matter at sub-nuclear densities, Nucl. Phys. A **207**, 298 (1973).

[184] D. G. Ravenhall, C. J. Pethick, and J. R. Wilson, Structure of Matter Below Nuclear Saturation Density, Phys. Rev. Lett. **50**, 2066 (1983).

[185] C. P. Lorenz, D. G. Ravenhall, and C. J. Pethick, Neutron Star Crusts, Phys. Rev. Lett. **70**, 379 (1993).

[186] P. Magierski and A. Bulgac, Nuclear hydrodynamics in the inner crust of neutron stars, Acta Phys. Pol. B **35**, 1203 (2004).

[187] P. Avogadro, F. Barranco, R. A. Broglia, and E. Vigezzi, Quantum calculation of vortices in the inner crust of neutron stars, Phys. Rev. C **75**, 012805 (2007).

[188] P. Avogadro, F. Barranco, R. A. Broglia, and E. Vigezzi, Vortex-nucleus interaction in the inner crust of neutron stars, Nucl. Phys. A **811**, 378 (2008).

[189] P. M. Pizzochero, L. Viverit, and R. A. Broglia, Vortex-Nucleus Interaction and Pinning Forces in Neutron Stars, Phys. Rev. Lett. **79**, 3347 (1997).

[190] P. M. Pizzochero, Pinning and binding energies for vortices in neutron stars: Comments on recent results, *Exotic States of Nuclear Matter* (World Scientific, Singapore, 2007), pp. 388–395.

[191] P. M. Pizzochero, Angular momentum transfer in Vela-like pulsar glitches, Astrophys. J. Lett. **743**, L20 (2011).

[192] A. Bulgac, M. McNeil Forbes, and R. Sharma, Strength of the Vortex-Pinning Interaction from Real-Time Dynamics, Phys. Rev. Lett. **110**, 241102 (2013).

[193] Y. Yu and A. Bulgac, Spatial Structure of a Vortex in Low Density Neutron Matter, Phys. Rev. Lett. **90**, 161101 (2003).

[194] L. R. Gasques, A. V. Afanasjev, E. F. Aguilera, M. Beard, L. C. Chamon, P. Ring, M. Wiescher, and D. G. Yakovlev, Nuclear fusion in dense matter: Reaction rate and carbon burning, Phys. Rev. C **72**, 025806 (2005).

[195] E. G. Adelberger, A. García, R. G. Hamish Robertson, K. A. Snover, A. B. Balantekin, K. Heeger, M. J. Ramsey-Musolf, D. Bemmerer, A. Junghans, C. A. Bertulani *et al.*, Solar fusion cross sections, II: The *pp* chain and CNO cycles, Rev. Mod. Phys. **83**, 195 (2011).

[196] S. Schram and S. E. Koonin, Pycnonuclear fusion rates, Astrophys. J. **365**, 296 (1990).

[197] A. V. Afanasjev, M. Beard, A. I. Chugunov, M. Wiescher, and D. G. Yakovlev, Large collection of astrophysical *S* factors and their compact representation, Phys. Rev. C **85**, 054615 (2012).

[198] A. S. Umar, V. E. Oberacker, C. J. Horowitz, P.G. Reinhard, and J. A. Maruhn, Swelling of nuclei embedded in neutron-gas and consequences for fusion, Phys. Rev. C **92**, 025808 (2015).

[199] M. Hashimoto, H. Seki, and M. Yamada, Shape of nuclei in the crust of neutron star, Progr. Theor. Phys. **71**, 320 (1984).

[200] H. A. Bethe, Supernova mechanisms, Rev. Mod. Phys. **62**, 801 (1990).

[201] H.-T. Janka, Explosion mechanisms of core-collapse supernovae, Annu. Rev. of Nucl. Part. Sci. **62**, 407 (2012).
[202] C. J. Horowitz, M. A. Pérez-García, and J. Piekarewicz, Neutrino-"pasta" scattering: The opacity of nonuniform neutron-rich matter, Phys. Rev. C **69**, 045804 (2004).
[203] M. D. Alloy and D. P. Menezes, Nuclear "pasta phase" and its consequences on neutrino opacities, Phys. Rev. C **83**, 035803 (2011).
[204] M. Gearheart, W. G. Newton, J. Hooker, and B.-A. Li, Upper limits on the observational effects of nuclear pasta in neutron stars, Mon. Not. Royal Astron. Soc. **418**, 2343 (2011).
[205] J. A. Pons, D. Vigano, and N. Rea, A highly resistive layer within the crust of x-ray pulsars limits their spin periods, Nat. Phys. **9**, 431 (2013).
[206] Y. Levin and G. Ushomirsky, Crust–core coupling and r-mode damping in neutron stars: A toy model, Mon. Not. Royal Astron. Soc. **324**, 917 (2001).
[207] M. Okamoto, T. Maruyama, K. Yabana, and T. Tatsumi, Nuclear "pasta" structures in low-density nuclear matter and properties of the neutron-star crust, Phys. Rev. C **88**, 025801 (2013).
[208] F. J. Fattoyev, C. J. Horowitz, and B. Schuetrumpf, Quantum nuclear pasta and nuclear symmetry energy, Phys. Rev. C **95**, 055804 (2017).
[209] B. Schuetrumpf, K. Iida, J. A. Maruhn, and P.-G. Reinhard, Nuclear "pasta matter" for different proton fractions, Phys. Rev. C **90**, 055802 (2014).
[210] G. Audi, A. H. Wapstra, and C. Thibault, The Ame2003 atomic mass evaluation, Nucl. Phys. A **729**, 337 (2003).
[211] M. Baldo, P. Schuck, and X. Viñas, Kohn-Sham density functional inspired approach to nuclear binding, Phys. Lett. B **663**, 390 (2008).
[212] M. Baldo, L. M. Robledo, P. Schuck, and X. Viñas, New Kohn-Sham density functional based on microscopic nuclear and neutron matter equations of state, Phys. Rev. C **87**, 064305 (2013).
[213] M. Baldo, C. Maieron, P. Schuck, and X. Viñas, Low densities in nuclear and neutron matters and in the nuclear surface, Nucl. Phys. A **736**, 241 (2004).
[214] E. Garrido, P. Sarriguren, E. Moya de Guerra, and P. Schuck, Effective density-dependent pairing forces in the $T = 1$ and $T = 0$ channels, Phys. Rev. C **60**, 064312 (1999).
[215] S. A. Fayans, S. V. Tolokonnikov, E. L. Trykov, and D. Zawischa, Nuclear isotope shifts within the local energy-density functional approach, Nucl. Phys. A **676**, 49 (2000).
[216] J. L. Egido and L. M. Robledo, Angular momentum projection and quadrupole correlations effects in atomic nuclei, in *Extended Density Functionals in Nuclear Structure Physics*, edited by G. A. Lalazissis, P. Ring, and D. Vretenar (Springer, Berlin, 2004), pp. 269–302.
[217] M. N. Butler, D. W. L. Sprung, and J. Martorell, An improved approximate treatment of c.m. motion in DDHF calculations, Nucl. Phys. A **422**, 157 (1984).
[218] T. Niksic, D. Vretenar, and P. Ring, Relativistic nuclear energy density functionals: Mean-field and beyond, Prog. Part. Nucl. Phys. **66**, 519 (2011).
[219] S. E. Agbemava, A. V. Afanasjev, D. Ray, and P. Ring, Global performance of covariant energy density functionals: Ground-state observables of even-even nuclei and the estimate of theoretical uncertainties, Phys. Rev. C **89**, 054320 (2014).
[220] S. Goriely, M. Samyn, J. M. Pearson, and M. Onsi, Further explorations of Skyrme-Hartree-Fock-Bogoliubov mass formulas, IV: Neutron-matter constraint, Nucl. Phys. A **750**, 425 (2005).
[221] P.-G. Reinhard, Lecture at ECT*, Trento, Italy, January 26–30, 2015 [https://sites.google.com/site/ectworkshopns2015/talks].
[222] N. Schunck, J. Dobaczewski, J. McDonnell, J. Moré, W. Nazarewicz, J. Sarich, and M. V. Stoitsov, One-quasiparticle states in the nuclear energy density functional theory, Phys. Rev. C **81**, 024316 (2010).
[223] J. Engel, Intrinsic-density functionals, Phys. Rev. C **75**, 014306 (2007).
[224] N. Barnea, Density functional theory for self-bound systems, Phys. Rev. C **76**, 067302 (2007).
[225] B. G. Giraud, Scalar nature of the nuclear density functional, Phys. Rev. C **78**, 014307 (2008).
[226] B. G. Giraud, Density functionals in the laboratory frame, Phys. Rev. C **77**, 014311 (2008).
[227] B. G. Giraud, B. K. Jennings, and B. R. Barrett, Existence of a density functional for an intrinsic state, Phys. Rev. A **78**, 032507 (2008).
[228] J. Messud, M. Bender, and E. Suraud, Density functional theory and Kohn-Sham scheme for self-bound systems, Phys. Rev. C **80**, 054314 (2009).
[229] J. Messud, Generalization of internal density-functional theory and Kohn-Sham scheme to multicomponent self-bound systems, and link with traditional density-functional theory, Phys. Rev. A **84**, 052113 (2011).
[230] J. Messud, Alternate, well-founded way to treat center-of-mass correlations: Proposal of a local center-of-mass correlations potential, Phys. Rev. C **87**, 024302 (2013).
[231] S. Goriely, M. Samyn, M. Bender, and J. M. Pearson, Further explorations of Skyrme-Hartree-Fock-Bogoliubov mass formulas, II: Role of the effective mass, Phys. Rev. C **68**, 054325 (2003).
[232] M. Samyn, S. Goriely, M. Bender, and J. M. Pearson, Further explorations of Skyrme-Hartree-Fock-Bogoliubov mass formulas, III: Role of particle-number projection, Phys. Rev. C **70**, 044309 (2004).
[233] M. Bender, G. F. Bertsch, and P.-H. Heenen, Correlation energies by the generator coordinate method: Computational aspects for quadrupolar deformations, Phys. Rev. C **69**, 034340 (2004).
[234] M. Bender, G. F. Bertsch, and P.-H. Heenen, Systematics of Quadrupolar Correlation Energies, Phys. Rev. Lett. **94**, 102503 (2005).
[235] M. Bender, G. F. Bertsch, and P.-H. Heenen, Global study of quadrupole correlation effects, Phys. Rev. C **73**, 034322 (2006).
[236] M. Baranger and M. Véneroni, An adiabatic time-dependent Hartree-Fock theory of collective motion in finite systems, Ann. Phys. (N.Y.) **114**, 123 (1978).
[237] D. M. Brink, M. J. Giannoni, and M. Veneroni, Derivation of an adiabatic time-dependent Hartree-Fock formalism from a variational principle, Nucl. Phys. A **258**, 237 (1976).
[238] A. F. Andreev and E. P. Bashkin, 3-velocity hydrodynamics of superfluid solutions, Zh. Éksp. Teor. Fiz. **69**, 319 (1975) [Sov. Phys. JETP **42**, 164 (1975)].
[239] G. E. Volovik, V. P. Mineev, and I. M. Khalatnikov, Theory of solutions of a superfluid Fermi liquid in a superfluid Bose liquid, Zh. Éksp. Teor. Fiz. **69**, 675 (1975) [Sov. Phys. JETP **42**, 342 (1975)].

[240] G. A. Vardanyan and D. M. Sedrakyan, Magnetohydrodynamics of superfluid solutions, Zh. Éksp. Teor. Fiz. **81**, 1731 (1981) [Sov. Phys. JETP **54**, 919 (1981)].
[241] M. A. Alpar, S. A. Langer, and J. A. Sauls, Rapid postglitch spin-up of the superfluid core in pulsars, Astrophys. J. **282**, 533 (1984).
[242] M. Borumand, R. Joynt, and W. Kluźniak, Superfluid densities in neutron-star matter, Phys. Rev. C **54**, 2745 (1996).
[243] E. Babaev, Andreev-Bashkin effect and knot solitons in an interacting mixture of a charged and a neutral superfluid with possible relevance for neutron stars, Phys. Rev. D **70**, 043001 (2004).
[244] M. E. Gusakov and P. Haensel, The entrainment matrix of a superfluid neutron–proton mixture at a finite temperature, Nucl. Phys. A **761**, 333 (2005).
[245] N. Chameland P. Haensel, Entrainment parameters in a cold superfluid neutron star core, Phys. Rev. C **73**, 045802 (2006).
[246] N. Chamel, Crustal Entrainment and Pulsar Glitches, Phys. Rev. Lett. **110**, 011101 (2013).
[247] D. N. Kobyakov, C. J. Pethick, S. Reddy, and A. Schwenk, Dispersion and decay of collective modes in neutron star cores, Phys. Rev. C **96**, 025805 (2017).
[248] T. von Egidy and D. Bucurescu, Systematics of nuclear level density parameters, Phys. Rev. C **72**, 044311 (2005).
[249] D. García-Aldea and J. E. Alvarellos, Kinetic energy density study of some representative semilocal kinetic energy functionals, J. Chem. Phys. **127**, 144109 (2007).
[250] J. W. Negele and D. Vautherin, Density-matrix expansion for an effective nuclear Hamiltonian, Phys. Rev. C **5**, 1472 (1972).
[251] J. W. Negele and D. Vautherin, Density-matrix expansion for an effective nuclear Hamiltonian, II, Phys. Rev. C **11**, 1031 (1975).
[252] B. Gebremariam, T. Duguet, and S. K. Bogner, Improved density matrix expansion for spin-unsaturated nuclei, Phys. Rev. C **82**, 014305 (2010).
[253] W. Stocker, J. Bartel, J. R. Nix, and A.J. Sierk, Anomaly in the nuclear curvature energy, Nucl. Phys. A **489**, 252 (1988).
[254] M. Brack, B. K. Jennings, and Y. H. Chu, On the extended Thomas-Fermi approximation to the kinetic energy density, Phys. Lett. B **65**, 1 (1976).
[255] A. Bulgac, Semilocal approach to nonlocal equations, Nucl. Phys. A **487**, 251 (1988).
[256] M. McNeil Forbes and R. Sharma, Validating simple dynamical simulations of the unitary Fermi gas, Phys. Rev. A **90**, 043638 (2014).
[257] X. Viñas, M. Centelles, X. Roca-Maza, and M. Warda, Density dependence of the symmetry energy from neutron skin thickness in finite nuclei, Eur. Phys. J. A **50**, 27 (2014).
[258] C. J. Horowitz, E. F. Brown, Y. Kim, W. G. Lynch, R. Michaels, A. Ono, J. Piekarewicz, M. B. Tsang, and H. H. Wolter, A way forward in the study of the symmetry energy: Experiment, theory, and observation, J. Phys. G **41**, 093001 (2014).
[259] B. A. Brown, Constraints on the Skyrme Equations of State from Properties of Doubly Magic Nuclei, Phys. Rev. Lett. **111**, 232502 (2013).
[260] B. A. Brown and A. Schwenk, Constraints on Skyrme equations of state from properties of doubly magic nuclei and *ab initio* calculations of low-density neutron matter, Phys. Rev. C **89**, 011307 (2014).
[261] A. F. Fantina, N. Chamel, J. M. Pearson, and S. Goriely, Constraints on the equation of state of cold dense matter from nuclear physics and astrophysics, EPJ Web Conf. **66**, 07005 (2014).
[262] J. Erler, C. J. Horowitz, W. Nazarewicz, M. Rafalski, and P.-G. Reinhard, Energy density functional for nuclei and neutron stars, Phys. Rev. C **87**, 044320 (2013).
[263] C. F. Perdrisat, V. Punjabi, and M. Vanderhaeghen, Nucleon electromagnetic form factors, Prog. Part. Nucl. Phys. **59**, 694 (2007).
[264] T. R. Gentile and C. B. Crawford, Neutron charge radius and the neutron electric form factor, Phys. Rev. C **83**, 055203 (2011).